IDENTIFYING PARAMETERS FROM THE BIOHEAT TRANSFER EQUATION USING MAGNETIC RESONANCE-GUIDED FOCUSED ULTRASOUND

by

Christopher Reed Dillon

A dissertation submitted to the faculty of
The University of Utah
in partial fulfillment of the requirements for the degree of

Doctor of Philosophy

Department of Bioengineering

The University of Utah

August 2014

The University of Utah Graduate School

STATEMENT OF DISSERTATION APPROVAL

The following faculty members served as the supervisory committee chair and members for the dissertation of Christopher Reed Dillon.

Dates at right indicate the members' approval of the dissertation.

Douglas A. Christensen, Chair	30 April 2014 Date Approved
Robert B. Roemer, Member	30 April 2014 Date Approved
Dennis L. Parker, Member	30 April 2014 Date Approved
Allison Payne, Member	30 April 2014 Date Approved
Edward W. Hsu, Member	30 April 2014 Date Approved

The dissertation has also been approved by Patrick A. Tresco, Chair of the Department/School/College of Bioengineering and by David B. Kieda, Dean of The Graduate School.

ABSTRACT

For magnetic resonance-guided focused ultrasound (MRgFUS) treatments to be broadly accepted, progress must be made in treatment planning, monitoring, and control. A key component to this goal is accurate modeling of the bioheat transfer equation (BHTE). This dissertation develops new methods for identifying the significant parameters of the BHTE: the ultrasonic specific absorption rate (SAR), the tissue thermal diffusivity, and perfusion-related energy losses.

SAR is determined by fitting an analytical solution (one-dimensional radial Gaussian heating) to MRgFUS temperature data in simulations and a tissue-mimicking phantom. This new method is compared with linear and exponential methods for different fitting times, beam sizes, perfusion, and thermal diffusivity values. The analytical method is consistently most reliable and is accurate to within 10% for all cases, except high perfusion. An extension to the analytical solution improves SAR estimates for high perfusion cases.

MRgFUS sampling characteristics (spatial averaging, temporal sampling, and noise) for SAR and thermal diffusivity estimation are parametrically evaluated against several focused ultrasound beam sizes. For single point heatings, a maximum voxel size of 1x1x3 mm^3 is recommended for temperature and estimate errors to remain less than 10%.

Two MRgFUS thermal diffusivity estimation methods are evaluated against a standard technique in *ex vivo* porcine and *in vivo* rabbit back muscle. Both methods

accurately estimate thermal diffusivity using cooling data (overall *ex vivo* error < 6%, *in vivo* < 12%). Including heating data in the Gaussian SAR method further reduces errors (*ex vivo* error < 2%, *in vivo* < 3%). The Gaussian SAR method has better precision than the Gaussian temperature method.

Two methods for quantifying perfusion-related energy losses using MRgFUS cooling temperatures are developed (experimental + modeled data vs. experimental data). The methods are verified via simulations and experiments in *ex vivo* perfused porcine kidney at different flow rates. The difference techniques employed make these methods susceptible to noise errors, but this feasibility study demonstrates promise for their use in future work.

In conclusion, these methods can be used to validate biothermal models, and associated improvements in thermal modeling have the potential to increase the efficacy and safety of MRgFUS therapies.

TABLE OF CONTENTS

LIST OF TABLES

CHAPTER 1

INTRODUCTION

1.1 Introduction to thermal therapies

1.1.1 History and categories of thermal therapies

Physicians have employed thermal energy in therapeutic applications throughout human history, exploiting its ability to close wounds, minimize the spread of infection, and irreversibly damage undesirable tissues. The ancient Egyptians treated "swelling vessels" and "tumours or ulcers in the breast" using a "fire-drill" [1]. The Greek physician Hippocrates recommended using a red-hot iron to cauterize hemorrhoids, small tumors, and other diseases [2-4]. While the application of thermal energy for therapeutic purposes today may be more sophisticated, it relies upon the same principles that have been employed for millennia.

The use of thermal energy in current cancer therapies can generally be divided into two categories. First, in local hyperthermia, the tissue temperature is raised to ~43-45 °C for extended periods of time and can kill cancer cells directly or induce changes in tumor physiology that sensitize it to other therapies. Temperature elevation increases vascular permeability and induces vasodilation for increased blood flow, improving delivery of chemotherapeutic agents to the tumor. The increased blood flow during hyperthermia reduces hypoxia in tumors, making them more sensitive to radiation therapy [5,6].

Cancer drugs may also be encapsulated in temperature-sensitive liposomes or microbubbles which locally release their therapeutic agents in high temperature tissues [7].

The second category of thermal therapies is thermal ablation, which involves rapidly heating the tumor to temperatures well above 45 °C for short periods of time. This extensive temperature rise causes irreversible damage to cells by causing protein denaturation, coagulation, and necrosis [8]. Additionally, inflammation from tissue ablation can recruit immune effector cells to the target region, inducing an immune response to help the body attack any remaining cancer cells [9]. Exposed proteins and cellular debris from damaged tissue can also act as antigens, stimulating a systemic immunomodulation that targets local cancer cells as well as distant metastases which were not directly affected by the thermal treatment [10,11].

The distinction between hyperthermia and thermal ablation is indefinite as are the associated physiological responses, because thermal tissue damage is dependent upon the duration of temperature elevation as well as its magnitude. Most often, thermal damage is based upon an Arrhenius model where time and temperature contribute to thermal dose in a nonlinear fashion [12]. The extent of damage in this model is compared to an equivalent heating at 43 °C, and total necrosis of biological tissues has been shown to range from 25 to 240 minutes at 43 °C [13].

1.1.2 Thermal therapy modalities

Thermal therapy modalities for inducing hyperthermia or thermal ablation include radio-frequency [14], microwave [15], laser-induced thermotherapy [16], and focused

ultrasound (FUS) [17,18]. Cryotherapy is an ablative modality that causes necrosis by lowering tissue temperatures to extreme values [19]. The choice of which modality to utilize for a thermal therapy depends upon factors such as physician expertise, device availability, as well as tumor properties, geometry, location, and relative position to other anatomical structures [9].

The work in this dissertation utilizes the heating modality of magnetic resonance-guided focused ultrasound (MRgFUS). Focused ultrasound generates precise, localized, and completely noninvasive heating in deep tissues, while MR-guidance allows the temperature distribution to be monitored in near real-time. The noninvasive nature of MRgFUS makes it an attractive alternative to traditional cancer therapies, yet acceptance as a mainstream clinical option remains elusive. In the United States, MRgFUS has only been FDA approved for treatment of uterine fibroids and pain palliation of bone metastases, though studies are underway for the treatment of brain, breast, liver, kidney, pancreas, bone, and prostate cancers [18,20].

1.1.3 Objective: Accurate biothermal modeling in MRgFUS

Biothermal modeling is utilized to predict dynamic temperature distributions generated and altered by the therapeutic heating modality, tissue energy storage and dissipation, and blood flow. Implementation of biothermal modeling in the planning, monitoring, control, and evaluation of MRgFUS therapies can help to minimize treatment time, maximize efficacy, and ensure the safety of healthy normal tissues, while increasing clinical confidence in MRgFUS treatments. Recognizing that model predictions will only be as accurate as the individual parameters comprising the model, the purpose of this

dissertation is to develop and evaluate techniques for obtaining patient-specific values for each of the significant parameters used in biothermal modeling of MRgFUS treatments.

Since this work requires an understanding of focused ultrasound, magnetic resonance imaging (MRI), and biothermal modeling, a discussion of the essential physics for each area is presented in this chapter. Motivations for biothermal modeling and improved estimation of biothermal parameters are established and an overview of each chapter in this dissertation is given.

1.2 Essentials of focused ultrasound

1.2.1 Ultrasound frequency, spatial resolution, and depth of penetration

Ultrasound refers to inaudible acoustic waves with frequencies ranging from approximately 20 kHz to several hundred MHz [21]. It has the ability to propagate through human soft tissue and is regularly used in the clinic for diagnostic and therapeutic purposes. The range of ultrasonic frequencies typically used in medical applications is constrained by two factors: the desire for good spatial resolution and the need to penetrate into deep tissues.

Spatial resolution will be shown to be directly proportional to the wavelength (λ) of the ultrasound, which is a function of the tissue speed of sound (c) and the ultrasonic frequency (f), as seen in Equation 1.1:

$$\lambda = \frac{c}{f}. \tag{1.1}$$

Because most human tissues have a speed of sound approximately equal to that of water (c=1500 m/s), higher frequencies will lead to shorter wavelengths and better spatial resolution.

The intensity of the ultrasound beam decreases with increasing depth into the tissue from several effects, including reflections at tissue interfaces with differing acoustic impedances and from the diverging wavefront which spreads the area over which the ultrasound intensity is distributed. However, the primary cause of intensity loss in most tissues is attenuation of the beam itself, which, in the absence of other effects, is described by the equation

$$I(z) = I_0 e^{-2\alpha z}, \tag{1.2}$$

where I is the average ultrasound intensity (W/m^2) as a function of depth z into the tissue, I_0 represents the intensity at the skin surface, and α is the tissue's attenuation coefficient. Because α increases with increasing ultrasonic frequencies, utilizing lower frequencies will improve the depth of penetration.

The competing constraints of spatial resolution (high frequencies) and depth of penetration (low frequencies) require compromise in therapeutic ultrasound applications and result in therapeutic frequencies typically ranging from 0.75-3 MHz [22]. Based on Equations 1.1 and 1.2, these frequencies will yield wavelengths of 0.5-2.1 mm with half-intensity penetrating depths of approximately 1.3-7.1 cm for average nonfatty soft tissues [23].

1.2.2 Ultrasound absorption and focusing

The attenuation coefficient is the sum of local scattering effects (which are often assumed negligible) and the absorption of the ultrasound beam by the tissue. If scattering is neglected, the power deposition ($\dot{Q}'''_{FUS}$) of ultrasound into a tissue region is equal to the loss of ultrasound intensity in that region, which can be calculated by differentiating

Equation 1.2 with respect to z. After differentiation, substituting Equation 1.2 yields

$$\dot{Q}'''_{FUS} = -2\alpha I. \tag{1.3}$$

The dot in the notation of $\dot{Q}'''_{FUS}$ indicates energy measured *per unit time,* and the triple prime indicates *per unit volume;* hence, the units of $\dot{Q}'''_{FUS}$ are W/m^3. In Equation 1.3, $\dot{Q}'''_{FUS}$ is negative because it represents a loss in the intensity of the ultrasound beam. These losses come from conversion of the ultrasound wave's mechanical energy into thermal energy and result in a temperature rise in the tissue. It is noteworthy that the energy deposition into the tissue is proportional to the acoustic intensity defined by Equation 1.2, suggesting that power deposition from a single unfocused ultrasound source is greatest near the skin and decreases exponentially with depth into the body.

For focused ultrasound applications, the ultrasound beam is manipulated so that power deposition can be significantly greater in deep tumor tissues than in the skin and intervening tissue. By modifying the ultrasound transducer to be shaped like a lens (see Figure 1.1), the propagating ultrasound beam will be focused much like light converges after passing through a magnifying glass. The distribution of the ultrasound beam in the focal plane is related to the Bessel function of the first kind with order 1 and has a diameter (measured between the first zeros) equal to

$$d = 2.44\left(\frac{l_f}{D}\right)\lambda, \tag{1.4}$$

where D and l_f are the diameter and focal length of the ultrasound transducer, respectively. Because the intensity contributions from all parts of the transducer are converging at the focal location in this small diameter, local intensity and, by extension, power deposition can be several orders of magnitude greater than at the skin surface and

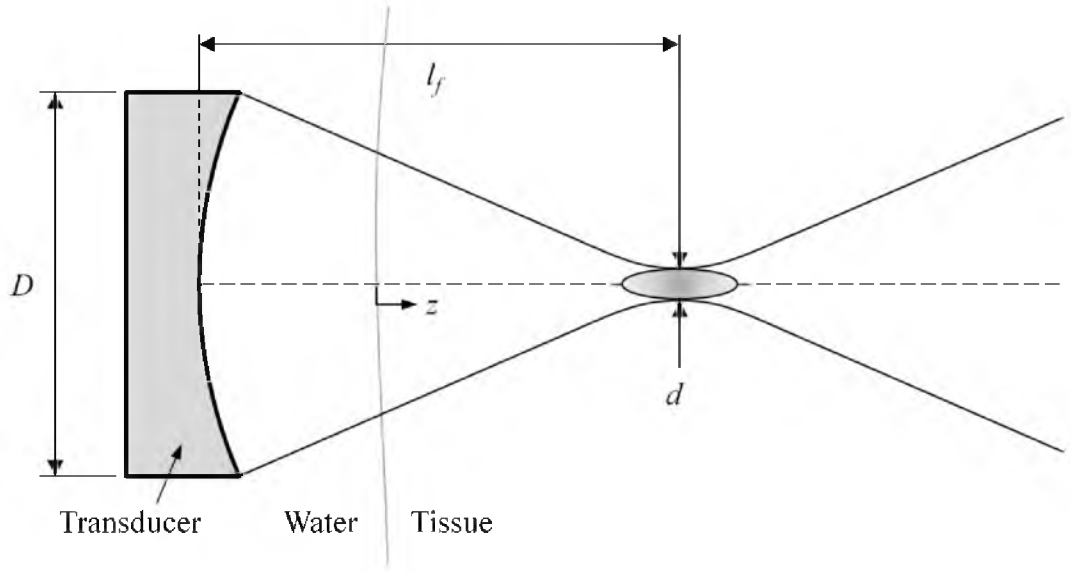

Figure 1.1: Schematic illustrating how an ultrasound transducer can focus energy deep in the tissue. The diameter of the focus d is a function of the transducer diameter D, focal length l_f, and the ultrasound wavelength.

intervening tissues. The ability of FUS to produce highly localized deep tissue power deposition noninvasively is what makes it such a powerful and promising therapeutic modality.

1.2.3 Past challenges to FUS and new solutions

The earliest demonstrations of FUS for altering localized biology were performed in the 1940s [24,25]. FUS was first used for thermal ablation in the brain [26-28] and the potential of FUS as a cancer therapy was first suggested [29] during the 1950s. Over the next few decades, one primary obstacle prevented FUS from developing into a widespread clinical option for cancer therapy: the lack of extensive real-time temperature monitoring of the treatment [30].Real-time monitoring of FUS can improve the safety of the treatment by preventing ultrasound cavitation and protecting critical structures and normal tissues from overheating. Monitoring provides feedback for controllers that can

adjust treatment parameters to optimize for time and efficacy. Dynamic monitoring of the treatment can help to identify treatment endpoints such as cumulative equivalent minutes at 43 °C [12]. Finally, and most significantly for this dissertation, monitoring of thermal therapies provides information essential to the validation of biothermal models used to plan, predict, and evaluate those treatments.

Traditional monitoring of thermal therapies has involved the insertion of thermocouples or thermistor probes at a few locations of interest to measure local temperatures. Several challenges arise with this approach. Pointwise measurements lack information about the desired spatial distribution of temperatures. Additional probes may be introduced for more information, but at the cost of increased complexity, time required for accurate positioning, and financial costs. While models may be used to fill in temperature profiles between discrete measurements, in many cases they still do not provide sufficient information to ensure the safety and efficacy of the treatment. Application of FUS can cause localized viscous heating at the probe which increases uncertainty in temperature measurements. While the noninvasive nature of FUS therapies makes them appealing, if invasive probes are required to monitor the treatment, with associated risks of infection and damage to intervening tissues, these therapies lose much of their attractiveness.

Recent developments in several noninvasive techniques for monitoring temperature distributions have renewed interest in FUS as a thermal therapy. These modalities include infrared thermography [31,32], microwave tomography [33], impedance tomography [34,35], CT Hounsfield unit changes [36,37], ultrasound temperature imaging [38,39], and magnetic resonance temperature imaging (MRTI) [40,41]. In spite

of its comparatively high cost, MRTI has become the imaging method of choice for many FUS researchers because it enables dynamic three-dimensional imaging with good spatial (~1 mm^3) and temporal resolutions (1-5 s) and accuracy (~1 °C). Magnetic resonance imaging lacks the ionizing radiation of some other modalities and is also useful for definition of the target and critical tissue boundaries as well as for immediate and long term posttreatment evaluation [42]. Thus, this single imaging platform has applications at all stages of the treatment: anatomy imaging and target definition, planning, monitoring, control, and evaluating treatment outcomes. The next section reviews the basic physics of MRI and how temperature is measured with this technology.

1.3 Essentials of magnetic resonance imaging

1.3.1 Spin, precession, and the Larmor frequency

Spin is the property of the nucleus of some atoms (those that have an odd number of protons and neutrons) that makes MRI possible. Most notably, the nucleus of hydrogen, with one proton and no neutrons, exhibits this property. Its composition explains why the terms hydrogen and proton are often used interchangeably in MRI. Because the concentration of hydrogen atoms may be up to three orders of magnitude greater than that of other isotopes used for MRI (due to the large proportion of water in our bodies), MRI of hydrogen requires much less time to acquire images with the desired spatial resolution and image quality [43-47].

The spin of a proton coupled with its charge creates a small magnetic field like a bar magnet. Placing the proton in a strong applied magnetic field, such as an MRI magnet, will cause the proton to preferentially align with that field. Spin gives the proton angular

momentum, so that if it is tipped away from the strong magnetic field by some means, in addition to spinning around its own axis, it will precess about the axis of the applied magnetic field. Precession is similar to the wobbling of a child's toy top (about the axis of the gravitational field) before it falls over, even as it continues to spin about its own axis. The frequency at which isotopes such as hydrogen precess is called the Larmor frequency (ω), which depends upon the strength of the applied magnetic field (B_0) and a constant called the gyromagnetic ratio (γ), as shown in Equation 1.5:

$$\omega = \gamma B_0. \tag{1.5}$$

Each isotope that exhibits spin has its own unique gyromagnetic ratio. Hydrogen has the highest frequency of all isotopes, with a value of 42.57 MHz/Tesla [44].

In the absence of an applied magnetic field, the spins of hydrogen are randomly distributed, effectively canceling out their overall magnetization. The presence of a strong magnetic field, however, defines two energy states in which the spins will eventually thermally equilibrate. It is slightly more probable that each individual spin is found in the lower energy (parallel) state than in the higher energy (antiparallel) state and because of the presence of so many hydrogen protons, a measurable bulk magnetic effect can be observed. The combined effect of these individual protons can be represented by a single vector ($\vec{M}$), precessing about the magnetic field B_0 at the Larmor frequency ω (see Figure 1.2).

1.3.2 Generating transverse magnetization, and detecting the magnetic field

At equilibrium in the B_0 field, the protons do not precess and the bulk magnetization is exclusively in the longitudinal direction (M_z). To generate a transverse magnetization

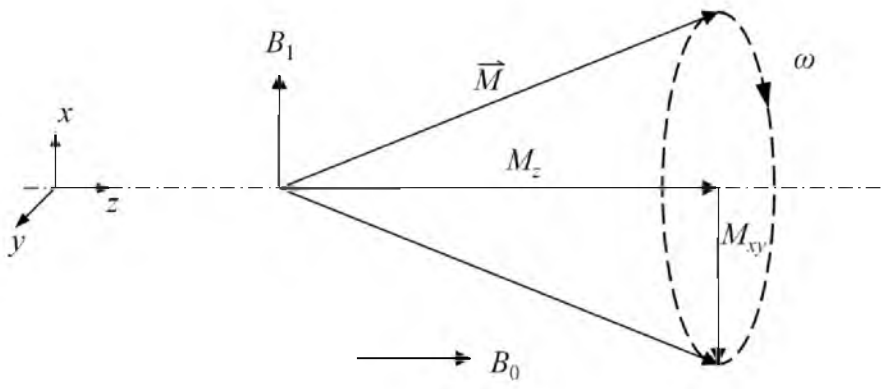

Figure 1.2: A radio-frequency pulse in the B_1 direction can tip the protons' bulk magnetization away from the main field B_0 and cause them to precess about the z axis at the Larmor frequency ω. The magnetization vector $\vec{M}$ can be separated into its longitudinal M_z and transverse M_{xy} components.

(M_{xy}), a radio-frequency (RF) pulse at the Larmor frequency, referred to as the B_1 field, is applied. This pulse tips the bulk magnetization from the longitudinal direction toward the transverse direction and synchronizes the phases of the protons' precession. Immediately following the application of the B_1 field, two effects are observed: 1) the proton spins begin to dephase and 2) the protons begin to move back toward their parallel orientation with the longitudinal B_0 field. Dephasing of the protons is related to the tissue's transverse relaxation constant T2. The rate at which the protons return to their stable alignment with B_0 is represented by the tissue's longitudinal relaxation constant T1. The flip angle (α) is the angle of the magnetization with respect to the z-direction after the application of the B_1 field. Thus, the transverse magnetization immediately following the RF pulse is related to the original longitudinal magnetization by a factor of $\sin(\alpha)$.

Receiver coils, with amplifiers tuned to the Larmor frequency, are oriented perpendicular to B_0 and used to measure the time-varying component of the protons' magnetization in the transverse plane. These coils convert the transverse magnetization

of the precessing protons into an electrical signal based on Faraday's law of electromagnetic induction [48]. Specifically, a time-varying voltage is induced in the receiver coil equal to the rate of change of the magnetic flux through the receiver coil. This voltage is amplified, filtered, digitized, and finally stored as the real and imaginary parts of the raw MRI signal.

1.3.3 Slice selection, and encoding location information

To generate an image, it is necessary to identify the location from which the MR signal originates. Since the receiver coils are noncollimated, this is accomplished by selectively exciting a slice in one direction and encoding spatial information for the other two dimensions into the MR signal [49]. Slices can be generated in any direction by introducing an applied gradient field in that direction. For simplicity, this discussion will orient the z-direction with the applied magnetic field B_0.

Applying a gradient field (G_z) in the z-direction makes B_0, and subsequently the Larmor frequency of protons in the field, a function of the z-direction. Simultaneous application of an RF pulse with a frequency matching the Larmor frequencies of the desired slice location will selectively cause only those protons to be excited. The thickness of the slice profile is a function of the gradient field distribution and the bandwidth of the slice selective RF pulse.

In much the same way, gradients (G_x and G_y) in the transverse plane are used to provide position information for the x- and y-directions. These transverse gradients are not used for selective excitation but are used to encode information about the x- and y-

positions into the MR signal itself. As an example, the signal (S) observed from a two-dimensional sequence with gradients of constant magnitude is given by [44]

$$S(t) = \iint \rho(x,y)\exp(-i\gamma G_x xt)\exp(-i\gamma G_y yt)dxdy, \quad (1.6)$$

where ρ(x,y) is the spatial distribution of spin density and ultimately represents the MR image.

1.3.4 k-space, and the Fourier transform

In practice, the collection of MR data occurs in the spatial-frequency domain, or k-space. k-Space is discretized in matrix form and the raw MR signal measured by the receiver coils is stored in this matrix. The gradient area at a given time, determined by the magnitude and duration of gradients in each transverse direction, determines the k-space position in which to store the signal data. When the k-space matrix is full, all of the information for the MR image has been acquired and the matrix can be processed to produce a final image. During image reconstruction, the inverse Fourier transform of k-space yields the MR image, which has the same number of rows and columns as the k-space matrix used to store the MR signal data. The size of k-space is also linked to the spatial resolution of the image, such that doubling the number of lines in one k-space direction will improve the spatial resolution in the corresponding image direction by a factor of two.

Because the precessing protons that generate the MR signal have different phases, the resulting image is complex. Changes in the tissue temperature will manifest themselves by a change in the phase of the complex image, as will be discussed in the next section.

1.3.5 Proton resonance frequency (PRF) shift

Temperature mapping using MRI was first investigated in 1983 using a method based upon the longitudinal relaxation time T1 [50,51]. Over a small range, T1 is linearly dependent on the absolute temperature, but T1 and its temperature dependence vary with tissue type, its coagulation status, and the MR field strength. Other temperature-dependent parameters that have been used for MR temperature measurements include the molecular diffusion coefficient of water [52,53], proton density [54], magnetization transfer [55], the transverse relaxation time T2 [56,57], the proton resonance frequency (PRF) shift [40,41], and others [58,59]. Depending on the method, temperature measurement can be relative or absolute and the linearity of temperature dependence, temperature sensitivity, advantages, and limitations of each method have been reviewed in other work [58-60].

The proton resonance frequency (PRF) shift method is the most commonly applied approach to obtaining MR temperature images [40-42,61]. The technique is explained by examining the local effects of temperature increases on water molecules in tissue. In general, the electrons of each water molecule shield the hydrogen nuclei from the full magnetic field B_0, such that the protons experience a slightly lower magnetic field and precess at a lower Larmor frequency than would otherwise be predicted. As temperature increases, the kinetic energy of water molecules goes up and hydrogen bonds between adjacent molecules weaken. At the same time, covalent bonds within the water molecule are shortened. In closer proximity to the oxygen atom, hydrogen protons are better shielded by the electron cloud of the molecule. This effective magnetic field on each

proton is further reduced, inducing a downshift in the Larmor resonance frequency of the protons, hence PRF shift.

The effect of electrons shielding hydrogen nuclei and causing a shift in the Larmor frequency is known as chemical shift and applies to all molecules containing hydrogen to varying degrees. While the difference in chemical shift observed between hydrogen atoms of water and those of fat is approximately 420 Hz at a field strength of 3 Tesla [62], chemical shift experienced in water molecules due to temperature change is much smaller. For RF-spoiled gradient echo images, the temperature (T) dependence of the image phase (Φ) can be expressed as the product of the chemical shift (σ), gyromagnetic ratio, echo time (T_E), and magnetic field strength (B_0), given by

$$\Phi(T) = \gamma T_E B_0 \sigma(T). \tag{1.7}$$

The chemical shift field has temperature dependent and nontemperature dependent components [61]. The temperature dependent component of the chemical shift varies linearly with temperature with a slope of $\alpha \approx$ -0.01 ppm/°C, which is relatively constant for many different tissues and is close to that of pure water [63]. Subtraction of the phase from a reference image eliminates all constant phase contributions, including the non-temperature dependent component of the chemical shift, and enables the measurement of temperature according to

$$\Delta T = T - T_{ref} = \left(\Phi(T) - \Phi\left(T_{ref}\right)\right)/(2\pi\alpha\gamma T_E B_0). \tag{1.8}$$

Because of the need to subtract a reference image, only changes in temperature are measureable with this technique and not absolute temperatures.

Challenges to accurate PRF measurements of temperature include artifacts introduced by the presence of lipids within a voxel, which tends to lower the proportionality constant

α. In voxels exclusively composed of lipids, temperature measurement with PRF is impossible because fat protons do not exhibit hydrogen bonding or the associated temperature-dependent chemical shift. Motion between and during image acquisitions introduces other errors in temperature measurements that must be accounted for. New methods and techniques are in development [64-68] to address these challenges and continued improvements will contribute to improved outcomes and acceptance of MRgFUS thermal therapies.

1.4 Essentials of biothermal modeling

Not only has MRTI facilitated monitoring for fully noninvasive FUS cancer therapies, but it has provided the opportunity to thoroughly evaluate various biothermal models with the extensive three-dimensional dynamic temperature data it provides. Biothermal models are essential to MRgFUS because of the desire to optimize the implementation of treatments ahead of time. Biothermal models can be used to identify locations of concern based on safety constraints intended to protect healthy tissues and critical structures, which may be challenging because of the heterogeneous patient-specific nature of human anatomy. Biothermal models are also utilized during pretreatment planning to make treatments faster and more effective than they would otherwise be, enabling the balance of healthy tissue constraints and efficient tumor treatment without excessive overdosing. During the treatment, biothermal models can be used in model predictive control to provide treatment feedback and impromptu adjustment for optimal therapies. This section of the Introduction is intended to introduce the principle equations of biothermal modeling through derivation of a generic bioheat equation, to discuss the challenges and

current approaches to modeling the required parameters of those equations, and to review the limited work that has been performed in verifying the most commonly applied biothermal model, the Pennes bioheat transfer equation [69].

1.4.1 Deriving a general bioheat equation

The first step in deriving a general equation for biothermal modeling is to identify the region to which the model will be applied. A control volume of approximately 1 mm^3 with fixed boundaries, across which mass and energy are allowed to flow, is appropriate. The size of the control volume is selected because it is large enough for the continuum assumption to hold and small enough that temperature, tissue properties, absorbed power, etc. can be assumed uniform within it. The width of a focused ultrasound beam is also approximately on this order as is the volume of a MRTI voxel. Within this control volume, which is comprised of tissue and blood, uniform, isotropic volume-averaged thermal properties are assumed and blood vessels are sufficiently small that uniform, isotropic capillary flow can be assumed.

An energy balance (in units of W) on the control volume including work ($\dot{W}$), heat ($\dot{Q}$) and mass transfer ($\dot{m}$), and storage terms (dE/dt) yields

$$\frac{dE}{dt} = \sum \dot{W} + \sum \dot{Q} + \dot{m}_{in}\theta_{in} - \dot{m}_{out}\theta_{out}, \tag{1.9}$$

where θ_{in} and θ_{out} represent the total energy (sum of the enthalpy, kinetic energy, and potential energy in J/kg) of the blood flowing into and out of the control volume, respectively [70]. Simplifying approximations include no work being performed on or by the control volume, negligible metabolic heat generation, steady flow of blood, and negligible changes in kinetic and potential energy. For this case, the only sources of heat

transfer are the absorbed FUS power ($\dot{Q}'''_{FUS}$) from Equation 1.3 and heat transfer by conduction, which is modeled by Fourier's law of conduction [71]. Because any convective exchange of energy between tissue and blood within the control volume does not affect the control volume boundaries, convection heat transfer will not appear in this model. Applying the above approximations, introducing the definition of specific heats [70], and reducing Equation 1.9 on a per volume basis (W/m^3) gives

$$\rho c \frac{dT}{dt} = \dot{Q}'''_{FUS} + k\nabla^2 T - \frac{\dot{m} c_{bl}\left(T_{bl,out} - T_{bl,in}\right)}{V}, \tag{1.10}$$

where T is the temperature of the control volume, ρ, c, and k are the volume-averaged tissue properties of density, specific heat capacity, and thermal conductivity, respectively, c_{bl} is the blood specific heat capacity, $T_{bl,out}$ is the average temperature of blood in all capillaries leaving the control volume, $T_{bl,in}$ is the corresponding average blood temperature entering the control volume, and V is the volume of the control volume.

The primary challenge of all biothermal modeling is accurately accounting for the final term in Equation 1.10, which would require knowledge of local blood temperatures going into and out of each control volume, as well as flow rates and connectivity throughout the vasculature. As this is very difficult both experimentally and computationally, the final term of Equation 1.10 will be replaced for now with a generic term $\dot{Q}'''_{bl}$, which accounts for energy losses from the control volume related to blood flow or perfusion:

$$\rho c \frac{dT}{dt} = \dot{Q}'''_{FUS} + k\nabla^2 T - \dot{Q}'''_{bl}. \tag{1.11}$$

For accurate modeling and prediction of temperature distributions for MRgFUS therapies, the general bioheat transfer equation (BHTE) given by Equation 1.11 requires

accurate knowledge of three primary parameters: the three-dimensional distribution of ultrasound power absorbed in the tissue ($\dot{Q}'''_{FUS}$), the tissue thermal diffusivity (κ), defined as $\kappa = k/\rho c$, which determines how quickly energy is conducted away from the focal zone, and $\dot{Q}'''_{bl}$, the perfusion-related energy losses. Obtaining accurate experimental estimates of these three parameters is the primary objective of this dissertation.

1.4.2 Specific absorption rate: Previous work and estimation approaches

Ultrasound power absorption for MRgFUS may be represented by the specific absorption rate (SAR) of the tissue, where

$$SAR = \frac{\dot{Q}'''_{FUS}}{\rho}. \tag{1.12}$$

Experimentally determined SAR values would benefit biothermal modeling of MRgFUS because calculated temperature distributions using SAR values from ultrasound simulation software do not match those found experimentally [72,73]. Discrepancies are often explained by hardware imperfections or the presence of beam-altering effects like scattering, multiple reflections, and refraction, which are difficult to measure *in vivo*. Many SAR predictive methods exclude some or all of these effects. Thus, experimentally determined SAR patterns have the potential to improve and validate ultrasound predictive models as well as being directly applicable to the improved biothermal modeling of MRgFUS thermal therapies.

SAR can be determined indirectly in the experimental setting by determining the rate of temperature increase immediately after the ultrasound power has been turned on [74]. This approach assumes that conduction and perfusion-related energy losses are small

compared to the absorbed power and energy storage terms of the BHTE. Equation 1.11 reduces under these conditions to the definition of SAR:

$$SAR = c\frac{dT}{dt}\Big|_{t=0^+}. \tag{1.13}$$

Previous researchers have determined for their applications that the approximations of minimal losses to conduction and blood flow are valid over time intervals of tens of seconds [74-78]. Such studies have utilized a linear fit to the temperature data for SAR estimates from microwaves and unfocused ultrasound transducers, which have widely distributed power deposition patterns. The SAR patterns of FUS are much sharper and smaller than those examined previously, challenging the validity of the linear fit method for FUS. Additionally, these studies relied upon thermistor and thermocouple measurements, the placement of which in relation to the FUS focal zone would likely introduce uncertainties and SAR estimate errors. In this dissertation, three-dimensional MR temperature data will be used to evaluate traditional and newly developed SAR estimation methods for the tightly focused beams of FUS. Establishing an accurate experimental SAR estimation method is key to accurate MRgFUS pretreatment planning and to the evaluation of biothermal and ultrasound predictive models.

1.4.3 Thermal diffusivity: Previous work and estimation approaches

Large spatial temperature gradients induced by FUS heating make tissue thermal diffusivity values a significant factor in the spatial and temporal accuracy of biothermal modeling of MRgFUS. While many researchers draw thermal diffusivity values directly from published property tables, the high degree of variability present in those tables demonstrates the necessity of patient-specific thermal diffusivity determination [79].

In the past, patient-specific estimation of thermal and acoustic properties from experimental temperatures was accomplished using thermistor probes [75,80-83]. More recent investigators have used thermistors [84], as well as infrared imaging [85,86], backscattered ultrasound imaging [87,88], and magnetic-resonance imaging [89,90] for estimation of thermal properties. Of note, Cheng and Plewes [89] published a noninvasive thermal diffusivity estimation method that uses the cooling MR temperature data following a short pulse of FUS. This method has been applied by several researchers with varying degrees of success in both *ex vivo* and *in vivo* tissues [89-92]. This dissertation will provide the first evaluation of the accuracy of this method by comparison of thermal diffusivity estimates with measurements from a standard invasive technique. An alternative MRgFUS-based thermal diffusivity estimation method will also be developed and its precision and accuracy will be investigated in *ex vivo* and *in vivo* tissues using clinically relevant heating and MR parameters. Accurate, noninvasive patient-specific thermal diffusivity values are essential to validation of biothermal models and will also be beneficial for the pretreatment planning, predictive control, and evaluation of MRgFUS thermal therapies.

1.4.4 Perfusion-related energy losses: Previous work

As mentioned previously, determining the magnitude and distribution of perfusion-related energy losses ($\dot{Q}_{bl}'''$) is the primary challenge of creating, verifying, and validating biothermal models. The challenge arises because blood flow exhibits nonhomogeneous dynamic responses to heating, has different effects from large vasculature and capillary beds, and is anisotropic and patient-specific in nature.

In biothermal modeling, it is generally accepted that large vessels should be modeled discretely while contributions from smaller vasculature can be treated collectively as a continuum [93]. Different criteria have been used to distinguish between large thermally significant vessels and smaller insignificant vessels. Chato [94] declared that the distinction between thermally significant vessels and small vessels in full equilibrium with the tissue depends mainly on vessel diameter and volumetric blood flow rate. Chen and Holmes [95] determined that on the arterial side, vessels with a diameter less than 0.5 mm would reach full equilibrium with the tissue temperature while vessels smaller than 0.8 mm in diameter would equilibrate on the venous side. Other theoretical work identified a transition diameter at 0.5 mm [96-98]. Shrivastava and Roemer [99] concluded that inflowing blood and surrounding tissue temperatures were more important than vessel diameter and that the determination of which vessels are thermally significant should be performed on a case-by-case basis. Regardless of where the transition occurs, this dissertation is interested exclusively in the modeling of microvasculature for which individual blood vessel effects can be summed and averaged over the control volume of interest.

The most often used continuum bioheat transfer model is the Pennes model (PBHTE) [69], in which the transfer of energy from the tissue to the blood is characterized by

$$\dot{Q}_{bl}''' = wc_{bl}(1-\varepsilon)(T - T_{ar}), \tag{1.14}$$

where w is the Pennes perfusion parameter, c_{bl} is the specific heat capacity of the blood, ε is a unitless constant identifying how close the exiting blood is to being in equilibrium with the tissue, and T_{ar} is the temperature of the incoming arterial blood. Empirically derived, the Pennes perfusion parameter w, measured in kg/m^3/s, is only equal to the true

capillary blood perfusion ($\dot{m}/V$ in Equation 1.10) in limited situations [100], although researchers regularly use them interchangeably. Predictably, the PBHTE is least accurate when heating is localized near large blood vessels [100-103]. In its most commonly applied form, full thermal equilibrium is assumed between the tissue and blood (ε=0) and the arterial blood temperature T_{ar} is taken to be a constant fixed core temperature, reducing Equation 1.14 to

$$\dot{Q}_{bl}''' = wc_{bl}(T - T_{ar}). \tag{1.15}$$

Thus, the PBHTE assumes that perfusion acts as a direction independent heat sink with heat losses proportional to the difference between local and arterial blood temperatures. The validity of assuming full equilibrium depends upon vessel diameter as discussed above and the assumption of constant incoming arterial blood temperature should hold if there is minimal time or space over which blood can exchange energy with the tissue, as would be the case with short duration FUS heatings. Despite its limitations and assumptions, the PBHTE has been shown to be sufficiently accurate in some limited cases [104-109]. While several investigators have attempted to formulate a better alternative [95,100,110,111], no one has developed a more reliable and fundamental description of heat transfer in living tissues.

In spite of its frequent application, only a few partial attempts have been made to experimentally establish the validity of the PBHTE. These studies have included data from cooled [112] and unheated [69] human forearms, cooled [113] and heated [114] human thigh muscle, FUS-heated greyhound thigh muscle [115], and *ex vivo* perfused bovine [116] and porcine kidneys [109]. While the solutions used to model the PBHTE in these studies have varied from analytical, finite-difference, and finite-element methods

with varying degrees of sophistication, in all of these efforts, validation has relied upon isolated thermocouple or thermistor measurements, or at best, a few measurements along a single line.

Fifty years after the PBHTE was first published, Wissler [105] performed a reanalysis of Pennes' original data and concluded with the following statement:

> Many potentially significant factors have been ignored both in Pennes' paper and in this paper. Some of them, such as the geometry and inhomogeneous structure of the forearm, are relatively easy to correct, because very effective numerical methods exist for solving the heat-conduction equation. Others, such as heat transfer between thermally significant vessels and tissue, are not so easily resolved. However, further progress is probably more severely limited by the paucity of definitive experimental data than by lack of theoretical methods for determining more realistic temperature fields. In conclusion, the purpose of this paper is to show that much of the criticism directed toward the Pennes model is not justified. Experimental data reported by Pennes are probably as good as we will ever have, unless a noninvasive technique is developed for measuring deep tissue temperatures.

This dissertation aims to address that "paucity of definitive experimental data." With the noninvasive deep tissue temperature monitoring of MRTI and the other techniques for quantifying the relevant parameters of the BHTE, this dissertation will develop the methods necessary to thoroughly evaluate the PBHTE and any other applicable biothermal models for use in MRgFUS thermal therapies.

1.5 Summary

This dissertation will use the tools of MRgFUS to develop methods for identifying the significant parameters of the BHTE: SAR, tissue thermal diffusivity, and perfusion-related energy losses. First, Chapter 2 will develop and test an analytical method to improve the accuracy of SAR values obtained from MRgFUS temperature data. SAR is determined by calculating the initial slope of an analytical solution (for a one-

dimensional radial Gaussian heating pattern) fit to the experimental temperature versus time data in simulations and a tissue-mimicking phantom. This new method is compared with the traditional linear approach to estimating SAR and a simplified exponential model for different fitting times, beam sizes, perfusion levels, and thermal diffusivity values. The work of Chapter 2 was published in *Physics in Medicine and Biology* in June 2012 [117].

Chapter 3 will discuss the significance of selecting MRTI sampling characteristics for use in estimating SAR and thermal diffusivity with MRgFUS. Any errors introduced into the MRTI temperature data by inappropriate sampling choices will propagate into estimates based on those data. The sampling characteristics of spatial averaging, temporal sampling, and Gaussian noise are parametrically evaluated against a variety of FUS beam sizes. The spatial region used for fitting of temperature data is assessed for its effect on the precision of estimates. This chapter provides researchers with appropriate MRTI conditions for obtaining accurate estimates of SAR and tissue thermal diffusivity. Chapter 3 was published in *Physics in Medicine and Biology* in September 2013 [118].

In Chapter 4, two thermal diffusivity estimation methods that utilize MRgFUS temperature data are evaluated and compared with a standard invasive measurement technique for *ex vivo* porcine muscle and *in vivo* rabbit back muscle. The first method assumes a Gaussian temperature distribution is maintained throughout the cooling period following a FUS heating pulse and uses the rate of expansion of the Gaussian temperatures' width to quantify the tissue thermal diffusivity. The second method uses the analytical solution developed in Chapter 2 for SAR estimation to make noninvasive estimates of thermal diffusivity. The method of Chapter 2 is extended to include both the

heating and cooling solutions when fitting for the tissue thermal diffusivity. The work presented in Chapter 4 is currently in review with the *International Journal of Hyperthermia.*

Chapter 5 develops a novel approach to quantifying term $\dot{Q}_{bl}'''$, the perfusion-related energy losses of Equation 1.11, using MRgFUS cooling temperature data. Two different methods for quantifying $\dot{Q}_{bl}'''$ are presented, one requiring both experimental and modeled temperature data and the other using experimental data exclusively. The methods are verified and compared based on simulations of the PBHTE and experiments in an *ex vivo* porcine kidney perfused at different flow rates.

Chapter 6 provides a summary and conclusions to the work in the dissertation. The combination of parameter estimation methods described and developed in this dissertation will make possible a more thorough evaluation of biothermal models than any performed previously. When implemented clinically, these methods will improve the accuracy of patient treatment planning, monitoring and control, resulting in safer, faster, and more efficacious MRgFUS thermal therapies.

1.6 References

1. Sullivan R (1996) The identity and work of the ancient Egyptian surgeon. J R Soc Med 89: 467-473.

2. Fienus T (1598) De cauteriis libri quinque. Louvain: B Zangrium.

3. Severino MA, van Horne J (1668) De la medecine efficace. Geneve: P Chouet.

4. Wolff J (1907) Die Lehre von der Krebskrankheit. Jena: G Fischer.

5. Kim JH, Hahn EW (1979) Clinical and biological studies of localized hyperthermia. Cancer Res 39: 2258–2261.

6. Kampinga HH (2006) Cell biological effects of hyperthermia alone or combined with radiation or drugs: a short introduction to newcomers in the field. Int J Hyperthermia 22: 191-196.

7. Staruch R, Chopra R, Hynynen K (2010) Localised drug release using MRI-controlled focused ultrasound hyperthermia. Int J Hyperthermia, 27: 156-171.

8. Thomsen S (1991) Pathologic analysis of photothermal and photomechanical effects of laser-tissue interactions. Photochem Photobiol 53: 825-835.

9. Haen SP, Pereira PL, Salih HR, Rammensee HG, Gouttefangeas C (2011) More than just tumor destruction: immunomodulation by thermal ablation of cancer. Clin Dev Immunol doi:10.1155/2011/160250

10. Rosberger DF, Coleman DJ, Silverman R, Woods S, Rondeau M, et al. (1994) Immunomodulation in choroidal melanoma: reversal of inverted CD4/CD8 ratios following treatment with ultrasonic hyperthermia. Biotechnol Ther 5: 59–68.

11. Zhang Y, Deng J, Feng J, Wu F (2010) Enhancement of antitumor vaccine in ablated hepatocellular carcinoma by high-intensity focused ultrasound. World J Gastroenterol 16: 3584-3591.

12. Sapareto SA, Dewey WC (1984) Thermal dose determination in cancer therapy. Int J Radiat Oncol Biol Phys 10: 787-800.

13. Dewhirst MW, Viglianti BL, Lora-Michiels M, Hanson M, Hoopes PJ (2003) Basic principles of thermal dosimetry and thermal thresholds for tissue damage from hyperthermia. Int J Hyperthermia 19: 267–294.

14. Siperstein AE, Gitomirski A (2000) History and technological aspects of radiofrequency thermoablation. Cancer J 6: 5293-5303.

15. Duan YQ, Gao YY, Ni XX, Wang Y, Feng L, et al. (2007) Changes in peripheral lymphocyte subsets in patients after partial microwave ablation of the spleen for secondary splenomegaly and hypersplenism: a preliminary study. Int J Hyperthermia 23: 467-472.

16. Pacella CM , Francica G , Di Lascio FM , Arienti V , Antico E , et al. (2009) Long-term outcome of cirrhotic patients with early hepatocellular carcinoma treated with ultrasound-guided percutaneous laser ablation: a retrospective analysis. J Clin Oncol 16: 2615-2621.

17. Fischer K, Gedroyc W, Jolesz FA (2010) Focused ultrasound as a local therapy for liver cancer. Cancer J 16: 118–124.

18. Kennedy J E (2005) High-intensity focused ultrasound in the treatment of solid tumors. Nat Rev Cancer 5: 321-327.

19. Chiu D, Niu L, Mu F, Peng X, Zhou L, et al. (2010) The experimental study for efficacy and safety of pancreatic cryosurgery. Cryobiology 60: 281-286.

20. Al-Bataineh O, Jenne J, Huber P (2012) Clinical and future applications of high intensity focused ultrasound in cancer. Cancer Treatment Rev 38: 346-353.

21. Christensen DA (1988) Ultrasonic bioinstrumentation. John Wiley & Sons. 235 p.

22. Speed CA (2001) Therapeutic ultrasound in soft tissue lesions. Rheumatol 40: 1331-1336.

23. International Commission on Radiation Units and Measurements (1998) ICRU Report 61: Tissue Substitutes, Phantoms and Computational Modelling in Medical Ultrasound. Bethesda, MD: ICRU Publications.

24. Lynn JG, Zwemer RL, Chick AJ, Miller AE (1942) A new method for the generation and use of focused ultrasound in experimental biology. J Gen Physiol 26: 179-193.

25. Lynn JG, Putnam TJ (1944) Histology of cerebral lesions produced by focused ultrasound. Am J Pathol 20: 637-649.

26. Fry WJ, Barnard JW, Fry FJ, Krumins RF, Brennan JF (1955) Ultrasonic lesions in the mammalian central nervous system. Science 122: 517-518.

27. Fry FJ (1958) Precision high intensity focusing ultrasound machines for surgery. Am J Phys Med 37: 152-156.

28. Fry WJ, Fry FJ (1960) Fundamental neurological research and human neurosurgery using intense ultrasound. IRE Trans Med Electron ME-7: 166-181.

29. Burov AK (1956) High intensity ultrasonic vibrations for action on animal and human malignant tumors. Dokl Akad Nauk SSR 106: 239-241.

30. ter Haar G (2007) Therapeutic applications of ultrasound. Prog Biophys Mol Biol 93: 111-129.

31. Ogan K, Roberts WW, Wilhelm DM, Bonnell L, Leiner D, et al. (2003) Infrared thermography and thermocouple mapping of radiofrequency renal ablation to assess treatment adequacy and ablation margins. Urology 62: 146-151.

32. Ruminski J, Kaczmarek M, Renkielska A, Nowakowski A (2007) Thermal parametric imaging in the evaluation of skin burn depth. IEEE Trans Biomed Eng 54: 303-312.

33. Meaney PM, Paulsen KD, Fanning MW, Li D, Fang Q (2003) Image accuracy improvements in microwave tomographic thermometry: phantom experience. Int J Hyperthermia 19: 534-550.

34. Amasha HM, Anderson AP, Conway J, Barber DC (1988) Quantitative assessment of impedence tomography for temperature measurements in microwave hyper-thermia. Clin Phys Physiol Meas 9: 49-53.

35. Blad B, Persson B, and Lindstrom K (1992) Quantitative assessment of impedence tomography for temperature measurements in hyperthermia. Int J Hyperthermia 8: 33-43.

36. Bruners P, Levit E, Penzkofer T, Isfort P, Ocklenburg C, et al. (2010) Multi-slice computed tomography: a tool for non-invasive temperature measurement? Int J Hyperthermia 26: 359-365.

37. Weiss N, Sosna J, Goldberg SN, Azhari H (2014) Non-invasive temperature monitoring and hyperthermic injury onset detection using X-ray CT during HIFU thermal treatment in ex vivo fatty tissue. Int J Hyperthermia 30: 119-125.

38. Mass Moreno R, Damianou C (1996) Noninvasive temperature estimation in tissue via ultrasound echo shifts. Part I. Analytical model. J Acoust Soc Amer 100: 2514-2521.

39. Simon C, VanBaren P, Ebbini ES (1998) Two-dimensional temperature estimation using diagnostic ultrasound. IEEE Trans Ultrason Ferroelect Freq Contr 45: 989-1000.

40. De Poorter JD, De Wagter C, De Deene Y, Thomsen C, Stahlberg F, et al. (1995) Noninvasive MRI thermometry with the proton resonance frequency (PRF) method: in vivo results in human muscle. Magn Reson Med 33: 74-81.

41. Ishihara Y, Calderon A, Watanabe H, Okamoto K, Suzuki Y, et al. A precise and fast temperature mapping using water proton chemical shift. Magn Reson Med 33: 814-823.

42. Stafford RJ, Taylor BA (2012) Practical clinical thermometry. In: Moros E, editor. Physics of thermal therapy: fundamentals and clinical applications. Boca Raton, FL: CRC Press. pp. 41-55.

43. Rahman AU (1986) Nuclear magnetic resonance: basic principles. New York: Springer. 358 p.

44. Brown RW, Thompson MR, Venkatesan R (1999) Magnetic resonance imaging. Haacke EM, editor. New York: Wiley-Liss. 914 p.

45. Liang ZP, Lauterbur PC (2000) Principles of magnetic resonance imaging: a signal processing perspective. New York: IEEE, Inc. 416 p.

46. Levitt M (2001) Spin dynamics: basics of nuclear magnetic resonance. New York: John Wiley & Sons. 406 p.

47. Plewes DB, Kucharczyk W (2012) Physics of MRI: a primer. J Magn Reson Imaging, 35: 1038-1054.

48. Griffiths DJ, Reed College (1999) Introduction to electrodynamics (Vol. 3). Upper Saddle River, NJ: Prentice Hall. 576 p.

49. Lauterbur PC (1973) Image formation by induced local interactions: examples employing nuclear magnetic resonance. Nature 242: 190-191.

50. Parker DL, Smith V, Sheldon P, Crooks LE, Fussell L (1983) Temperature distribution measurements in two-dimensional NMR imaging. Med Phys 10: 321–325.

51. Parker DL (1984) Applications of NMR imaging in hyperthermia: an evaluation of the potential for localized tissue heating and noninvasive temperature monitoring. IEEE Trans Biomed Eng 31: 161-167.

52. Le Bihan D, Delannoy J, Levin RL (1989) Temperature mapping with MR imaging of molecular diffusion: application to hyperthermia. Radiology 171: 853-857.

53. Bleier AR, Jolesz FA, Cohen MS, Weisskoff RM, Dalcanton JJ, et al. (1991) Real-time magnetic resonance imaging of laser heat deposition in tissue. Magn Reson Med 21: 132-137.

54. Chen J, Daniel BL, Pauly KB (2006) Investigation of proton density for measuring tissue temperature. J Magn Reson Imaging 23: 430-434.

55. Young IR, Hand JW, Oatridge A, Prior MV (1994) Modeling and observation of temperature changes in vivo using MRI. Magn Reson Med 32: 358-369.

56. Graham SJ, Bronskill MJ, Henkelman RM (1998) Time and temperature dependence of MR parameters during thermal coagulation of ex vivo rabbit muscle. Magn Reson Med 39: 198-203.

57. Gandhi S, Daniel BL, Butts K (1998) Temperature dependence of relaxation times in bovine adipose tissue. In: Proc 6th Annual Meeting ISMRM, Sydney, Australia; 1998. p 701.

58. Rieke V, Butts Pauly K (2008) MR thermometry. J Magn Reson Imaging 27: 376-390.

59. Lüdemann L, Wlodarczyk W, Nadobny J, Weihrauch M, Gellermann J, et al. (2010) Non-invasive magnetic resonance thermography during regional hyperthermia. Int J Hyperthermia 26: 273-282.

60. Quesson B, de Zwart JA, Moonen CT (2000) Magnetic resonance temperature imaging for guidance of thermotherapy. J Magn Reson Imaging 12: 525-533.

61. de Senneville BD, Quesson B, Moonen CT (2005) Magnetic resonance temperature imaging. Int J Hyperthermia 21: 515-531.

62. Yu H, Shimakawa A, McKenzie CA, Brodsky E, Brittain JH, et al. (2008) Multiecho water-fat separation and simultaneous R 2* estimation with multi-frequency fat spectrum modeling. Magn Reson Med 60: 1122-1134.

63. Peters RD, Hinks RS, Henkelman RM (1998) Ex vivo tissue-type independence in proton-resonance frequency shift MR thermometry. Magn Reson Med 40: 454-459.

64. Todd N, Diakite M, Payne A, Parker DL (2013) Hybrid proton resonance frequency/T1 technique for simultaneous temperature monitoring in adipose and aqueous tissues. Magn Reson Med 69: 62-70.

65. Todd, N, Diakite M, Payne A, Parker DL (2013) In vivo evaluation of multi-echo hybrid PRF/T1 approach for temperature monitoring during breast MR-guided focused ultrasound surgery treatments. Magn Reson Med doi: 10.1002/mrm.24976

66. Diakite M, Odéen H, Todd N, Payne A, Parker DL (2013) Toward real-time temperature monitoring in fat and aqueous tissue during magnetic resonance–guided high-intensity focused ultrasound using a three-dimensional proton resonance frequency T1 method. Magn Reson Med doi: 10.1002/mrm.24900

67. de Senneville BD, Roujol S, Moonen C, Ries M (2010) Motion correction in MR thermometry of abdominal organs: a comparison of the referenceless vs. the multibaseline approach. Magn Reson Med 64: 1373-1381.

68. Grissom WA, Rieke V, Holbrook AB, Medan Y, Lustig M, et al. (2010) Hybrid referenceless and multibaseline subtraction MR thermometry for monitoring thermal therapies in moving organs. Med Phys 37: 5014-5026.

69. Pennes HH (1948) Analysis of tissue and arterial blood temperatures in the resting human forearm. J Appl Physiol 1: 93-122.

70. Cengel YA, Boles MA (2006) Thermodynamics: an engineering approach (5^{th} ed). New York: McGraw-Hill. 988 p.

71. Incropera FP, DeWitt DP (2002) Fundamentals of heat and mass transfer (5^{th} Ed). Hoboken, NJ: John Wiley & Sons. 981 p.

72. Mahoney K, Fjield T, McDannold N, Clement G, Hynynen K (2001) Comparison of modelled and observed in vivo temperature elevations induced by focused ultrasound: implications for treatment planning. Phys Med Biol 46: 1785-1798.

73. Payne A, Vyas U, Todd N, de Bever J, Christensen DA, et al. (2011) The effect of electronically steering a phased array ultrasound transducer on near-field tissue heating. Med Phys 38: 4971-4981.

74. Guy AW, Lehmann JF, Stonebridge JB (1974) Therapeutic applications of electromagnetic power. Proc IEEE 62: 55-75.

75. Roemer RB, Fletcher AM and Cetas TC (1985) Obtaining local SAR and blood perfusion data from temperature measurements: steady state and transient techniques compared. Int J Radiation Oncology Biol Phys 11: 1539-1550.

76. Sherar MD, Gladman AS, Davidson SRH, Trachtenberg J, Gertner MR (2001) Helical antenna arrays for interstitial microwave thermal therapy for prostate cancer: tissue phantom testing and simulations for treatment. Phys Med Biol 46: 1905-1918.

77. Samaras T, van Rhoon GC, and Sahalos JN (2002) Theoretical investigation of measurement procedures for the quality assurance of superficial hyperthermia applicators. Int J Hyperthermia 18: 416-425.

78. Gladman AS, Davidson SRH, Easty AC, Joy ML, Sherar MD (2004) Infrared thermographic SAR measurements of interstitial hyperthermia applicators: errors due to thermal conduction and convection. Int J Hyperthermia 20: 539-555.

79. Hasgall PA, Neufeld E, Gosselin MC, Klingenböck A, Kuster N (2013) IT'IS Database for thermal and electromagnetic parameters of biological tissues. Version 2.4. www.itis.ethz.ch/database

80. Goss SA, Cobb JW, Frizzell LA (1977) Effect of beam width and thermocouple size on the measurement of ultrasonic absorption using the thermoelectric technique. IEEE Ultrasonics Symp Proc 206-211.

81. Parker KJ (1983) The thermal pulse decay technique for measuring ultrasonic absorption coefficients. J Acoust Soc Amer 74: 1356-1361.

82. Parker KJ (1985) Effects of heat conduction and sample size on ultrasonic absorption measurements. J Acoust Soc Amer 77: 719-725.

83. Valvano JW, Allen JT, Bowman HF (1984) The simultaneous measurement of thermal conductivity, thermal diffusivity, and perfusion in small volumes of tissue. J Biomech Eng 106: 192-197.

84. Kharalkar NM, Hayes LJ, Valvano JW (2008) Power-pulse integrated-decay technique for the measurement of thermal conductivity. Meas Sci Technol 19 075104.

85. Milner TE, Goodman DM, Tanenbaum BS, Anvari B, Nelson JS (1996) Noncontact determination of thermal diffusivity in biomaterials using infrared radiometry. J Biomed Opt 1: 92-97.

86. Telenkov SA, Youn J, Goodman DM, Welch AJ, Milner TE (2001) Non-contact measurement of thermal diffusivity in tissue. Phys Med Biol 46: 551-558.

87. Anand A, Kaczkowski PJ (2008) Noninvasive measurement of local thermal diffusivity using backscattered ultrasound and focused ultrasound heating. Ultrasound Med Biol 34: 1449-1464.

88. Anand A, Kaczkowski PJ (2009) Noninvasive determination of in situ heating rate using kHz acoustic emissions and focused ultrasound. Ultrasound Med Biol 35: 1662-1671.

89. Cheng HL, Plewes DB (2002) Tissue thermal conductivity by magnetic resonance thermometry and focused ultrasound heating. J Magn Reson Imaging 16: 598-609.

90. Dragonu I, de Oliveira PL, Laurent C, Mougenot C, Grenier N, et al. (2009) Non-invasive determination of tissue thermal parameters from high intensity focused ultrasound treatment monitored by volumetric MRI thermometry. NMR Biomed 22: 843-851.

91. Cornelis F, Grenier N, Moonen CT, Quesson B (2011) In vivo characterization of tissue thermal properties of the kidney during local hyperthermia induced by MR-guided high-intensity focused ultrasound. NMR Biomed 24:799-806.

92. Zhang J, Mougenot C, Partanen A, Muthupillai R, Hor PH (2013) Volumetric MRI-guided high-intensity focused ultrasound for noninvasive, in vivo determination of tissue thermal conductivity: initial experience in a pig model. J Magn Reson Imaging 37: 950-957.

93. Chato JC (1985) Measurement of thermal properties of biological materials. In: Shitzer A, Eberhard RC, editors. Heat transfer in medicine and biology. New York: Plenum. pp. 167-192.

94. Chato JC (1980) Heat transfer to blood vessels. J Biomech Eng 102:110-118.

95. Chen MM, Holmes KK (1980) Microvascular contributions to tissue heat transfer. Ann NY Acad Sci 335:137-150.

96. Roemer RB (1991) Optimal power deposition in hyperthermia I. The treatment goal: the ideal temperature distribution II. The role of large blood vessels. Int J Hyperthermia 7:317-341.

97. Crezee J (1993) Experimental verification of thermal models. PhD Thesis. University of Utrecht.

98. Kolios MC, Sherar MD, Hunt JW (1996) Blood flow cooling and ultrasonic lesion formation. Med Phys 23:1287-1298.

99. Shrivastava D, Roemer RB (2006) Readdressing the issue of thermally significant blood vessels using a countercurrent vessel network. J Biomech Eng 128: 210-216.

100. Roemer RB, Dutton AW (1998) A generic tissue convective energy balance equation: Part I-theory and derivation. J Biomech Eng 120: 395-404.

101. Kolios MC, Sherar MD, Hunt JW (1996) Blood flow cooling and ultrasonic lesion formation. Med Phys 23: 1287-1298.

102. Kolios MC, Worthington AE, Holdsworth DW, Sherar MD, Hunt JW (1999) An investigation of the flow dependence of temperature gradients near large vessels during steady state and transient tissue heating. Phys Med Biol 44: 1479-1497.

103. Huang HW, Shih TC, Liauh CT (2010) Predicting effects of blood flow rate and size of vessels in a vasculature on hyperthermia treatments using computer simulation. Biomed Eng Online 9: 18.

104. Roemer RB, Forsyth K, Oleson JR, Clegg ST, Sim DA (1988) The effect of hydralazine dose on blood perfusion changes during hyperthermia. Int J Hyperthermia 4: 401-415.

105. Wissler EH (1988) An analytical solution countercurrent heat transfer between parallel vessels with a linearaxial temperature gradient. J Biomech Eng 110: 254-256.

106. Strohbehn JW, Curtis EH, Paulsen KD, Yuan XC, Lynch DR (1989) Optimization of the absorbed power distribution for an annular phased array hyperthermia system. Int J Radiation Oncology Biol Phys 16: 589-599.

107. Clegg ST, Roemer RB (1993) Reconstruction of experimental hyperthermia temperature distributions: application of state and parameter estimation. J Biomech Eng 115: 380-388.

108. Arkin H, Xu LW, Roemer RB (1994) Recent developments in modeling heat transfer in blood perfused tissues. IEEE Trans Biomed Eng 41: 97-107.

109. Kolios MC, Worthington AE, Sherar MD, Hunt JW (1998) Experimental evaluation of two simple thermal models using transient temperature analysis. Phys Med Biol 43: 3325-3340.

110. Weinbaum S, Jiji LM (1985) A new simplified bioheat equation for the effect of blood flow on local average tissue temperature. J Biomech Eng 107: 131-139.

111. Weinbaum S, Xu LX, Zhu L, Ekpene A (1997) A new fundamental bioheat equation for muscle tissue: Part I-perfusion term. J Biomech Eng 119: 278-288.

112. Wissler EH (1998) Pennes' 1948 paper revisited. J Appl Physiol 85: 35-41.

113. Mitchell JW, Galvez TL, Hengle J, Myers GE, Siebecker KL (1970) Thermal response of human legs during cooling. J Appl Physiol 29: 859-865.

114. Sekins KM, Lehmann JF, Esselman P, Dundore D, Emery AF, et al. (1984) Local muscle blood flow and temperature responses to 915MHz diathermy as simultaneously measured and numerically predicted. Arch Phys Med Rehabil 65: 1-7.

115. Moros EG, Dutton AW, Roemer RB, Burton M, Hynynen K (1993) Experimental evaluation of two simple thermal models using hyperthermia in muscle in vivo. Int J Hyperthermia 9: 581-598.

116. Crezee J, Lagendijk JW (1990) Experimental verification of bioheat transfer theories: measurement of temperature profiles around large artificial vessels in perfused tissue. Phys Med Biol 35: 905-923.

117. Dillon CR, Vyas U, Payne A, Christensen DA, Roemer RB (2012) An analytical solution for improved HIFU SAR estimation. Phys Med Biol 57: 4527-4544.

118. Dillon CR, Todd N, Payne A, Parker DL, Christensen DA, et al. (2013) Effects of MRTI sampling characteristics on estimation of HIFU SAR and tissue thermal diffusivity. Phys Med Biol 58: 7291-7307.

CHAPTER 2

AN ANALYTICAL SOLUTION FOR IMPROVED HIFU SAR ESTIMATION

Reprinted with permission from

IOP Publishing.

Dillon CR, Vyas U, Payne A, Christensen DA, Roemer RB (2012)

An analytical solution for improved HIFU SAR estimation.

Phys Med Biol 57: 4527-4544.

IOP PUBLISHING PHYSICS IN MEDICINE AND BIOLOGY
Phys. Med. Biol. 57 (2012) 4527–4544 doi:10.1088/0031-9155/57/14/4527

An analytical solution for improved HIFU SAR estimation

C R Dillon[1], U Vyas[1], A Payne[2,3], D A Christensen[1,4] and R B Roemer[1,2,3]

[1] Department of Bioengineering, University of Utah, 72 S Central Campus Drive, Salt Lake City, UT 84112, USA
[2] Department of Mechanical Engineering, University of Utah, 50 S Central Campus Dr, Salt Lake City, UT 84112, USA
[3] Utah Center for Advanced Imaging Research, 729 Arapeen Drive, Salt Lake City, UT 84108, USA
[4] Department of Electrical and Computer Engineering, University of Utah, 50 S Central Campus Dr, Salt Lake City, UT 84112, USA

E-mail: christopher.dillon@utah.edu

Received 29 October 2011, in final form 16 May 2012
Published 22 June 2012
Online at stacks.iop.org/PMB/57/4527

Abstract

Accurate determination of the specific absorption rates (SARs) present during high intensity focused ultrasound (HIFU) experiments and treatments provides a solid physical basis for scientific comparison of results among HIFU studies and is necessary to validate and improve SAR predictive software, which will improve patient treatment planning, control and evaluation. This study develops and tests an analytical solution that significantly improves the accuracy of SAR values obtained from HIFU temperature data. SAR estimates are obtained by fitting the analytical temperature solution for a one-dimensional radial Gaussian heating pattern to the temperature versus time data following a step in applied power and evaluating the initial slope of the analytical solution. The analytical method is evaluated in multiple parametric simulations for which it consistently (except at high perfusions) yields maximum errors of less than 10% at the center of the focal zone compared with errors up to 90% and 55% for the commonly used linear method and an exponential method, respectively. For high perfusion, an extension of the analytical method estimates SAR with less than 10% error. The analytical method is validated experimentally by showing that the temperature elevations predicted using the analytical method's SAR values determined for the entire 3D focal region agree well with the experimental temperature elevations in a HIFU-heated tissue-mimicking phantom.

Nomenclature

A	fitting parameter (°C s^{-1})
B	fitting parameter (°C)
c	speed of sound (m s^{-1})
c_p	specific heat (J (kg °C)$^{-1}$)
C	fitting parameter (°C s^{-1})
D	fitting parameter (s^{-1})
F	fitting parameter (dimensionless)
I_o	ultrasound intensity (W m^{-2})
k	thermal conductivity (W (m °C)$^{-1}$)
Q	power deposition density (W m^{-3})
r	radial distance from the beam axis (m)
SAR	specific absorption rate (W kg^{-1})
t	time (s)
t_s	sampling interval (s)
t_{tot}	total time for fit (s)
T	tissue temperature elevation from reference temperature (°C)
T_{ar}	arterial blood temperature (°C)
T_{PD}	temperature elevation (Pulse decay) (°C)
T_{SH}	temperature elevation (Step-heating) (°C)
w	perfusion coefficient (kg (m^3 s)$^{-1}$)
w_{loss}	effective heat loss coefficient (kg (m^3 s)$^{-1}$)
α	ultrasound absorption coefficient (Np m^{-1})
β	ultrasound Gaussian variance (m^2)
γ	fitting parameter (dimensionless)
κ	thermal diffusivity (m^2 s^{-1})
ρ	density (kg m^{-3})
τ	fitting parameter (s)

1. Introduction

One of the key biophysical elements for understanding and planning high intensity focused ultrasound (HIFU) treatments is knowledge of the power deposition delivered to the tissues. Absorbed power distributions during thermal therapies have historically been reported in terms of specific absorption rate (SAR) values, e.g. Guy *et al* (1974). While knowledge of the ultrasound transducer characteristics and power used in experiments is important, these data alone are insufficient to determine the SAR actually absorbed in the tissue due to the complicated effects of acoustic coupling, variations in patient and transducer geometry and variability in acoustic and thermal properties among tissues and subjects. Thus, accurate SAR values obtained experimentally will make standardized comparisons of HIFU data possible and will provide accurate input for evaluating SAR predictive models. The improved accuracy of SAR predictive models will lead to reliable and efficient patient treatment planning, control, and evaluation.

There is strong evidence to suggest that established SAR predictive models commonly used in thermal therapies do not accurately predict what occurs in HIFU treatments and that they, while being quite sophisticated and powerful, still need significant improvement. For example, Mahoney *et al* (2001) showed that, while ultrasound patterns modeled by the Raleigh–Sommerfeld integral method matched well with scanning hydrophone measurements

in degassed water, the temperature fields observed in *in vivo* rabbit thigh were wider than predicted and peak temperatures observed were significantly lower than predicted by SAR and temperature models. They explained that ultrasound scattering, reflections, and refraction, which are present in tissue but not in water, would likely change the ultrasound SAR pattern and cause the differences observed in predicted and experimental temperatures. These beam-altering effects are difficult to measure *in vivo* with traditional techniques and many SAR predictive methods exclude some or all of these effects. A primary objective of this paper is to provide a method for accurately estimating experimental SAR that can be used to improve, identify discrepancies in, and validate SAR predictive models to be used in patient treatment planning of HIFU thermal therapies.

A second motivation for obtaining accurate SAR estimates from experimental data is their usefulness in accurately characterizing experiments for comparison among investigators. For example, it has been shown that ultrasound attenuation values increase significantly during treatments, and that changes in attenuation are linked to the degree of ablation (Damianou *et al* 1997, Zderic *et al* 2004). Accurate pre- and post-treatment estimates of SAR will help quantify changes in attenuation and may be used to assess the effectiveness of the HIFU treatment (Vyas *et al* 2010).

While no method exists for measuring SAR directly from experiments, an indirect method for identifying SAR utilizes experimental temperature versus time curves and Pennes' bioheat transfer equation (Pennes 1948):

$$\rho c_p \frac{\partial T}{\partial t} = k\left(\frac{\partial^2 T}{\partial x^2} + \frac{\partial^2 T}{\partial y^2} + \frac{\partial^2 T}{\partial z^2}\right) - w c_p (T - T_{ar}) + Q. \tag{1}$$

Immediately following a power-on step function, conduction and blood flow heat transfer losses are small compared to the applied power, defined by $Q = \rho \mathrm{SAR}$, and energy storage terms. Under these conditions, (1) reduces to the definition of SAR (Guy *et al* 1974):

$$\mathrm{SAR} = c_p \left.\frac{\mathrm{d}T}{\mathrm{d}t}\right|_{t=0^+}. \tag{2}$$

In practice, obtaining SAR experimentally has involved measuring temperature following a step in heating, fitting the resulting data to a pre-specified function (usually temperature being a linear function in time), and then determining the slope of that function at time zero. SAR may only be accurately evaluated from knowledge of the *initial* slope of the temperature rise.

Previous hyperthermia-related researchers (Guy *et al* 1974, Roemer *et al* 1985, Sherar *et al* 2001, Samaras *et al* 2002, Gladman *et al* 2004) have noted for their applications that the approximations of minimal losses to conduction and blood flow are valid over time intervals of tens of seconds. Those investigators showed the accuracy and usefulness of a linear fit for SAR estimates from microwaves and unfocussed ultrasound transducers, which have widely distributed power deposition patterns. However, in HIFU treatments with their characteristic small focal zones, one would expect that conduction effects might become important at very short times after heating is initiated, raising questions about the accuracy and practicality of the linear fit method for HIFU.

A simple alternative function to the linear solution, an exponential curve, could be used to introduce temporal curvature caused by conduction and/or blood flow. Such a solution would be valid if both conduction and blood flow losses were approximately proportional to the temperature difference between the tissue and the arterial blood (Roemer *et al* 1985). If an exponential fit did indeed adequately represent the temperature rise, data from time intervals longer than the linear segment could be utilized and more accurate estimates of the initial slope used in SAR determination might be possible.

Table 1. Property and parameter values for simulations of SAR and temperature. Nominal values are given in bold.

Tissue properties	Values
Perfusion (kg $(m^3\ s)^{-1}$	0, **1**, 5, 10, 20, 30, 40, 50
Thermal conductivity (W $(m\ °C)^{-1}$)	0.2, **0.4**, 0.6
Specific heat (J $(kg\ °C)^{-1}$)	2600, **3400**, 4200
Density (kg m^{-3})	900, **1000**, 1100, 1200
Ultrasound parameters	**Values**
Power level (acoustic watts)	**5**, 10, 15
Focal zone size: Lateral × Axial FWHM (mm × mm)	Small: 0.65 × 3.7, **medium: 1.3 × 7.5**, large: 2.6 × 14.8

A more physics-based approach for estimating SAR would use a more fundamental model of the evolution of temperature with time, e.g. based on Pennes' equation (1), to obtain better descriptions of the temporal curvature. An analytical solution to (1) can be obtained if the geometric shape of the heating term (Q) is known. Multiple investigators have developed analytical models for the estimation of experimental parameters or tissue properties which employ point, spherical, or cylindrically symmetric one- or two-dimensional Gaussian heating sources (Goss *et al* 1977, Parker 1983, 1985, Valvano *et al* 1984, Arkin *et al* 1986, Kress and Roemer 1987, Nyborg 1988, Diederich *et al* 1989, Cheng and Plewes 2002, Cheng and Roemer 2005, Kharalkar *et al* 2008, Dragonu *et al* 2009). However, none of those investigators have used their analytical solutions to estimate SAR from temperature versus time data.

In this study, we compare SAR values estimated from fits to simulated step-function heating data using the linear method, an exponential fit, and an analytical solution using a one-dimensional radial Gaussian heating pattern based on the model of Parker (1985). The effects of tissue properties, applied power level, blood flow and transducer focal zone size are considered parametrically, as are the temperature sampling intervals and total time period used for each fitting method. The one-dimensional radial Gaussian analytical solution is derived for locations lateral to the axis of beam propagation and applied to find SAR values at those locations. Additionally, an analytical step-function solution for tissues with high perfusion rates (Kress and Roemer 1987) is extended to predict SAR at the center of the focal zone. These SAR estimation methods are compared to each other in simulated treatments and by comparison with experimental data from HIFU heating of a tissue-mimicking phantom.

2. Methods

2.1. Simulations

SAR patterns for a solid transducer (14.5 cm aperture and 13 cm radius of curvature) were simulated using the hybrid angular spectrum (HAS) method (Vyas and Christensen 2012). The simulations modeled a homogeneous medium with the transducer focused 3 cm deep in the tissue. The tissue speed of sound was 1500 m s^{-1} and acoustic attenuation was 5 Np m^{-1}. Since the HAS method does not include scattering, absorption was assumed to be the same as attenuation. The SAR patterns from these simulations were used as the reference standard for assessing the accuracy of each SAR estimation method. In order to study a normal range of properties found in living soft tissues (Duck 1990, ICRU 1998), every combination of tissue properties and ultrasound parameters found in table 1 was used in the simulations. The nominal values used throughout the study are given in bold in table 1.

For each simulated SAR pattern, the bioheat equation (1) was implemented in an explicit finite-difference (FD) solver to calculate temperatures for 30 s of heating. The FD solver used forward difference approximations for time derivatives with central difference approximations for spatial derivatives. The solver has been verified by comparison with several different analytical solutions using varied boundary conditions, initial conditions, and heat sources and has been used previously to validate experimental data with thermal models (Todd *et al* 2010, Payne *et al* 2011). For the small focal zone, the isotropic FD grid spacing was 0.1 mm, while for the medium and large focal zone sizes, it was 0.3 mm. To maintain numerical stability and accuracy, the temporal resolution of the FD solver was 0.01 s for the small focal zone calculations and 0.10 s for the medium and large focal zones.

To simulate the experimental acquisition of temperature data, a range of sampling intervals t_s from those practical for point-wise thermometry (0.25 and 1 s) to those more practical for magnetic resonance temperature imaging (MRTI) (5 and 10 s) was used. Except where effects of sampling interval were being studied, the nominal sampling interval of 5 s was used.

The length of time for each fit also affects SAR estimation accuracy. Therefore the total time for fit t_{tot} was varied from the minimum time possible for each estimation method studied to the entire duration of the ultrasound heating (30 s). The minimum total time for fit is dependent upon both the sampling interval and the number of unknown parameters in the estimation model, with each method requiring one more data point than its number of unknown parameters. Therefore, since the $t = 0$ data point was always used, for the nominal sampling interval $t_s = 5$ s, the minimum t_{tot} for a one-, two- and three-parameter fit is 5, 10, and 15 s respectively. The minimum total fitting times were used as the nominal total fitting times.

2.2. *SAR estimation models*

Since only changes in temperature are of significance, each model used for SAR estimation assumes that the tissue at time zero and the arterial blood are at the baseline reference temperature of zero:

$$T(t = 0) = T_{\text{ar}} = 0. \tag{3}$$

2.2.1. Linear model. The linear model assumes that all conduction and perfusion losses are negligible over the time interval used to generate the fit. The Pennes' equation (1) then reduces to

$$Q = \rho c_p \frac{\mathrm{d}T}{\mathrm{d}t}. \tag{4}$$

Separating and integrating with initial condition (3) yields a linear temperature profile:

$$T_{\text{LIN}} = \frac{Q}{\rho c_p} t = At. \tag{5}$$

The slope A is the linear method's single fitting parameter, which is obtained experimentally by applying a least-squares first-order polynomial (linear) fit (MATLAB function: polyfit) to the temperature versus time data at the position being studied. That process minimizes the least-squares difference between the treatment temperatures (either simulated or experimental) and the temperatures predicted by the linear solution (5). Once A is found, applying (5) to (2) yields the linear method's SAR estimate:

$$\text{SAR}_{\text{LIN}} = c_p A. \tag{6}$$

2.2.2. Exponential model. Mathematically, the exponential model combines the effects of conduction and perfusion into an effective loss term (w_{loss}) that is proportional to the difference between the tissue and arterial blood temperatures:

$$w_{loss}c_p(T - T_{ar}) = wc_p(T - T_{ar}) - k\left(\frac{\partial^2 T}{\partial x^2} + \frac{\partial^2 T}{\partial y^2} + \frac{\partial^2 T}{\partial z^2}\right). \tag{7}$$

Substituting (7) into (1) yields

$$\rho c_p \frac{\partial T}{\partial t} = Q - w_{loss}c_p T. \tag{8}$$

This first order ODE (8) with initial condition (3) is solved and simplified using fitting parameters B and τ to give the exponential temperature solution:

$$T_{EXP} = \frac{Q}{w_{loss}c_p}[1 - \exp(-w_{loss}t/\rho)] = B[1 - \exp(-t/\tau)]. \tag{9}$$

After fitting the temperature versus time data with a least-squares two-parameter fit (MATLAB function: fminsearch) for B and τ, differentiating (9) with respect to time to obtain the slope at time zero provides SAR estimates for the exponential method from (2) as

$$\mathrm{SAR}_{EXP} = c_p\frac{B}{\tau}. \tag{10}$$

2.2.3. Analytical model. The analytical model assumes that the ultrasonic power deposition pattern can be approximated by a 1D radial (cylindrical coordinates) Gaussian:

$$Q = 2\alpha I_0 \cdot \exp(-r^2/\beta). \tag{11}$$

The term β represents the ultrasound Gaussian variance and is essentially a measure of the beam width. This solution also assumes that axial conduction and all perfusion effects are negligible. For the small elliptically shaped focal zones typical of HIFU transducers, heat transfer is dominated by radial conduction because the spatial temperature gradients in that direction are much greater than in the axial direction. Thus, Kress and Roemer (1987) suggested that axial conduction could be neglected when the aspect ratio of the axial to lateral beam width is greater than two. HIFU beams in general, as well as each focal zone size assessed in this study, meet this criterion. Using these assumptions, Parker (1985) showed that the step-heating solution on the beam axis ($r = 0$) is given by

$$T_{ANA}(r = 0, t) = \frac{C}{D}\ln(1 + Dt), \tag{12}$$

where $C = 2\alpha I_0/\rho c_p$ and $D = 4\kappa/\beta$. Equation (12) can be fit to the temperature versus time data in a least-squares two-parameter fit for C and D. Differentiating and applying (2), the analytical method SAR estimates are given by

$$\mathrm{SAR}_{ANA}(r = 0) = c_p C. \tag{13}$$

If 3D temperature versus time data were available (such as is possible with MRTI), they could be used directly to estimate SAR for the entire heating region. This estimation would require an analytical step-heating solution for $r \neq 0$. To obtain such a solution, which has not been done in previous studies, note that when the ultrasound power is applied in an 'instantaneous' pulse, the temperature solution for Parker's (1985) one-dimensional radial Gaussian beam for all values of r and t is given by

$$T_{PD}(r, t) = \frac{2\alpha I_0 \Delta t}{\rho c_p(1 + 4\kappa t/\beta)}\exp\left(\frac{-r^2}{(4\kappa t + \beta)}\right). \tag{14}$$

The off-axis analytical step-heating solution can then be obtained as the summation over time of a series of pulse decay solutions:

$$T_{\mathrm{SH}}(r,t) = \int_0^t T_{\mathrm{PD}}(r,\tau)\,\mathrm{d}\tau. \tag{15}$$

Substituting (14) into (15) and integrating extends Parker's on-axis solution (12) to the off-axis analytical temperature solution:

$$T_{\mathrm{ANA}}(r,t) = C\left(\frac{\beta}{4\kappa}\right)\left[\mathrm{Ei}\left(\frac{-r^2}{\beta}\right) - \mathrm{Ei}\left(\frac{-r^2}{\beta(1+4\kappa t/\beta)}\right)\right], \tag{16}$$

where Ei represents the exponential integral defined by

$$\mathrm{Ei}(x) = -\int_{-x}^{\infty} \frac{\mathrm{e}^{-\varphi}}{\varphi}\,\mathrm{d}\varphi. \tag{17}$$

To find off-axis SAR estimates, (16) can be applied in two ways. First, when the radial position (r) relative to the axis of beam propagation is unknown, (16) is evaluated with the previously defined constant D and the new constant $F = r^2/\beta$ to give

$$T_{\mathrm{ANA}}(r,t) = \frac{C}{D}\left[\mathrm{Ei}(-F) - \mathrm{Ei}\left(\frac{-F}{(1+Dt)}\right)\right]. \tag{18}$$

A least-squares three-parameter fit for C, D, and F would then minimize differences between (18) and the temperature versus time data. Alternatively, if the radial distances (r) from the axis of beam propagation are known, as is likely in MRTI, a three-parameter fit applied directly to (16) will yield estimates for C, the thermal diffusivity κ, and the Gaussian variance β.

Differentiating these solutions with respect to time and evaluating at time $t = 0$, SAR can be evaluated from (2) by the equation

$$\mathrm{SAR}_{\mathrm{ANA}}(r \neq 0) = c_p C \cdot \exp\left(-\frac{r^2}{\beta}\right) = c_p C \cdot \exp(-F). \tag{19}$$

2.2.4. The extended analytical model: including perfusion. The analytical model above neglects the effects of blood perfusion, which draws heat away from the focal region and changes the shape of local temperature versus time curves. While this effect may be small for most tissues, which have low perfusions, in highly perfused organs such as the liver or kidney, using an analytical solution that neglects perfusion to estimate SAR may generate large errors. Kress and Roemer (1987) used the heating pattern for a one-dimensional radial Gaussian beam like Parker, but extended it to include the effects of global blood perfusion. Their extended step-heating solution was given as

$$T_{\mathrm{EXT}}(r=0,t) = \frac{C}{D}\exp(\gamma)[\mathrm{Ei}(-\gamma(1+Dt)) - \mathrm{Ei}(-\gamma)], \tag{20}$$

where the non-dimensional perfusion parameter is $\gamma = wc_p\beta/4k$. A least-squares three-parameter fit yields values for C, D, and γ. After differentiation and evaluation at time zero, SAR for the extended analytical method is calculated from (2) according to

$$\mathrm{SAR}_{\mathrm{EXT}}(r=0) = c_p C. \tag{21}$$

2.3. Experimental validation

2.3.1. Obtaining experimental temperature data. HIFU heating experiments were performed in a non-perfused tissue-mimicking phantom (ATS Laboratories, Bridgeport, CT, USA). The phantom was heated continuously for 20 s using an MR-compatible 256-element phased-array ultrasound system (Image Guided Therapy, Bordeaux, France) which operates at a frequency of 1 MHz and has a 14.5 cm aperture with 13 cm radius of curvature. Transducer power output was 18 acoustic watts. The geometric focus of the transducer was located 2.1 cm inside the phantom and the focus was steered electronically an additional 1 cm deep into the phantom. Deionized, degassed water coupled the ultrasound transducer to the phantom.

Images were acquired at $2 \times 2 \times 2$ mm^3 resolution in a 3T Siemens Trio MRI scanner using a standard 3D segmented EPI sequence. Other imaging parameters included TR/TE (ms) = 25/10, FA = 15°, bandwidth: 976 Hz/pixel, matrix: $128 \times 96 \times 16$, and a temporal resolution of 5.0 s per image volume. Temperatures were reconstructed using the proton resonance frequency method (De Poorter *et al* 1995, Ishihara *et al* 1995) and post-processed with zero-filled interpolation by a factor of 4 in all directions, resulting in 0.5 mm isotropic voxel spacing (Todd *et al* 2011). Temperature data were acquired at the following times after the onset of ultrasound heating: 3.1, 8.1, 13.1, and 18.1 s.

2.3.2. Determining SAR from experimental data. Utilizing the 3D temperature data, SAR estimates were made for every voxel in a $40 \times 40 \times 32$ mm^3 region around the focal zone (x, y, z where z is depth along the axis of beam propagation). All three estimation methods used the minimum total time required to estimate the fitting parameters: 5, 10, and 15 s for the linear, exponential, and analytical methods, respectively. For the linear and exponential methods, the temperature versus time data for each voxel ($80 \times 80 \times 64 = 409\,600$ voxels) were fit to temperature curves (5) and (9), and then SAR was estimated from (6) and (10), respectively.

The off-axis implementation of the analytical method allows more than a single voxel's data to be used in finding SAR estimates. Because β is a constant at each axial depth for a homogeneous phantom (but may vary with depth) and κ is also constant, a least-squares fit can be applied to temperature data from multiple voxels at the same depth simultaneously, generating a single estimate for fitting parameters C, κ, and β.

For these experimental data, the axis of beam propagation ($r = 0$) was determined by identifying the location of maximum temperature increase at each of the 64 axial depths in the focal region. Radial distances from that location to the center of voxels in a square region of interest 3.5×3.5 mm^2 (49 total voxels) centered at and perpendicular to the beam axis provided values for r in (16). For each depth, the 49 temperature versus time curves were fit simultaneously, minimizing the least-squares difference for all voxels at once and generating a single (planar) estimate for each parameter C, κ, and β. After applying this simultaneous parameter estimation at each depth, SAR was estimated from (19) for each voxel within the entire $40 \times 40 \times 32$ mm^3 region.

2.3.3. Validation of experimental SAR using modeled temperatures. To validate SAR estimation methods, the experimentally obtained SAR patterns from each fitting technique were used as inputs in a FD solver to calculate temperatures for comparison with experimental temperatures. Thermal properties of the phantom, obtained from ATS Laboratories, were $c_p = 3500$ J (kg °C)$^{-1}$ and $k = 0.5$ W (m °C)$^{-1}$. Density was measured at $\rho = 1025$ kg m^{-3}.

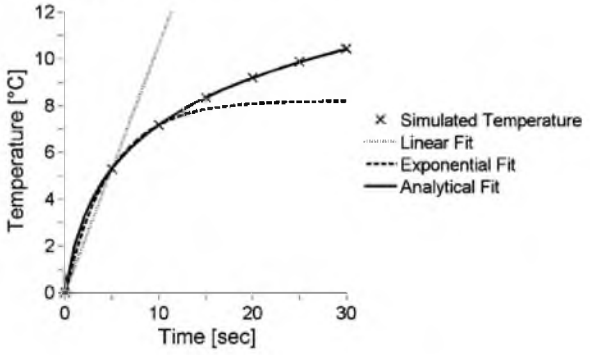

Figure 1. Representative temperature versus time plots at the center of the focal zone. Tissue properties were set at nominal values from table 1 with $t_s = 5$ s and the nominal (minimum) fitting times: $t_{tot} = 5, 10, 10$ s for the linear, exponential and analytical methods.

The spatial resolution of the calculated temperatures was 0.5 mm isotropic and the temporal resolution of the FD solver was 0.1 s.

By comparing the magnitudes and lateral distributions of the experimental temperatures with those predicted from the experimentally derived SAR, the relative accuracy of SAR estimation magnitudes and spatial distributions were assessed.

3. Simulation results

3.1. A representative time–temperature curve

Figure 1 is a representative time–temperature plot from simulations for the center of the focal zone using the nominal values (bold values in table 1). It also shows the results of the three fitting techniques for the nominal case. The results of the extended analytical fit that includes perfusion (20) are not shown since they are essentially identical to the analytical fit results.

3.2. SAR estimation at the center of the focal zone

Figure 2(a) shows the SAR estimation errors versus total fitting times at the center of the focal zone for three different sampling intervals: 1, 5, and 10 s. The analytical method estimates SAR with less than 10% error for all fitting times and, for each estimation method, SAR results are most accurate for a short total fitting time. The extended analytical method for estimating SAR that includes perfusion, though not shown, follows the data of the analytical method in figure 2 with less than $\pm 1\%$ difference. Arrows in figure 2(a) indicate the results when using the nominal sampling interval and fitting times.

The effects of focal zone size on SAR estimation accuracy at the center of the focal zone are shown in figure 3. The linear and exponential estimation methods improve significantly with increasing focal zone size. The analytical method estimates SAR to within 10% for all focal zone sizes studied. Results of the extended analytical method (not shown) match those of analytical method in figure 3 with less than $\pm 2\%$ variation.

Figure 4 shows SAR estimation errors associated with increasing perfusion. At low perfusion levels, the analytical method (that neglects perfusion) provides results comparable to the extended analytical method that includes perfusion. In highly perfused tissues (>10 kg

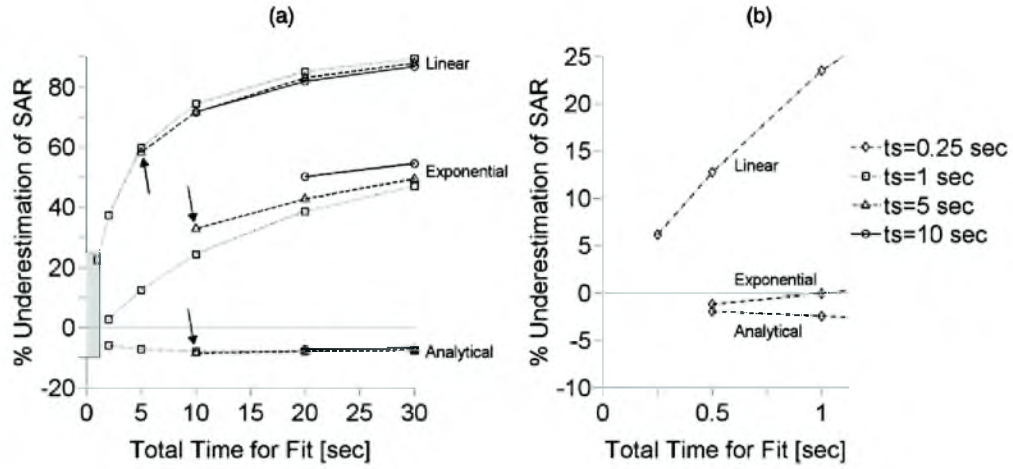

Figure 2. (a) Effect of total time for fit (t_{tot}) on SAR estimation at the center of the focal zone for different sampling interval (t_s) and estimation methods with other parameters set at nominal values. Arrows indicate SAR errors associated with nominal sampling interval and fitting times. (b) Inset of the shaded region within figure 2(a) that shows SAR estimation with a sampling interval $t_s = 0.25$ s.

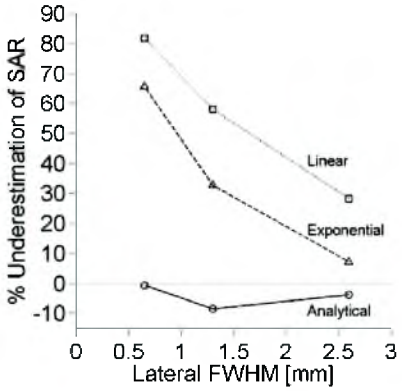

Figure 3. Effect of focal zone size on SAR estimation with other parameters set at nominal values.

$(m^3\ s)^{-1}$), errors in the simple analytical method continue to increase while errors in the extended analytical solution remain small and constant.

Figure 5 shows the effect of thermal diffusivity, $\kappa = k/(\rho c_p)$, on SAR estimates. Variation from the minimum to maximum values increases estimation errors for the linear and exponential methods by 43.0% and 41.8%, respectively. Errors in the analytical method vary from 5.5% to 8.5% across all thermal diffusivity values. The extended analytical method follows the data from the analytical method with less than $\pm 3\%$ difference.

Increasing the acoustic power level from the nominal 5 acoustic watts to 10 and 15 acoustic watts yields results identical to those presented in figures 2 through 5. Hence, variation in acoustic power level has no effect upon the accuracy of SAR regardless of estimation method or parameter values.

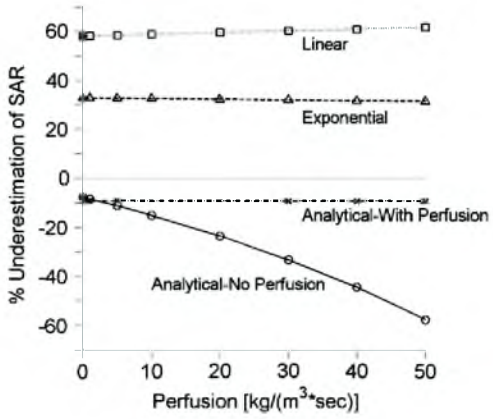

Figure 4. Effects of perfusion upon SAR estimation at the center of the focal zone with other parameters set at nominal values.

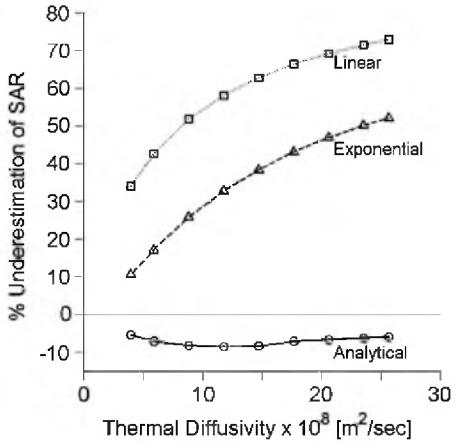

Figure 5. Effects of tissue thermal diffusivity upon SAR estimation at the center of the focal zone with other parameters set at nominal values.

3.3. Effects of spatial variation on SAR estimation

Figures 6(a)–(c) show SAR estimation as a function of lateral position for the small, medium, and large focal zones, respectively. Each lateral profile shown is at the depth of the maximum SAR. These results used the first off-axis analytical fitting approach described in section 2.2.3 with equation (18). The off-axis analytical method reproduces the SAR profile more accurately than the linear and exponential methods for all focal zone sizes. No results are presented for the extended analytical method since it cannot be applied for off-axis locations.

In figures 7(a)–(c), the axial SAR estimates are shown for the small, medium, and large focal zones, respectively. Each axial location lies on the axis of the ultrasound beam ($r = 0$). The analytical method is the most accurate predictor of SAR for all focal zone sizes. The linear and exponential methods underestimate SAR within the focal zone and improve as focal zone size increases. The extended analytical method results (not shown) matched the analytical method to within $\pm 2\%$.

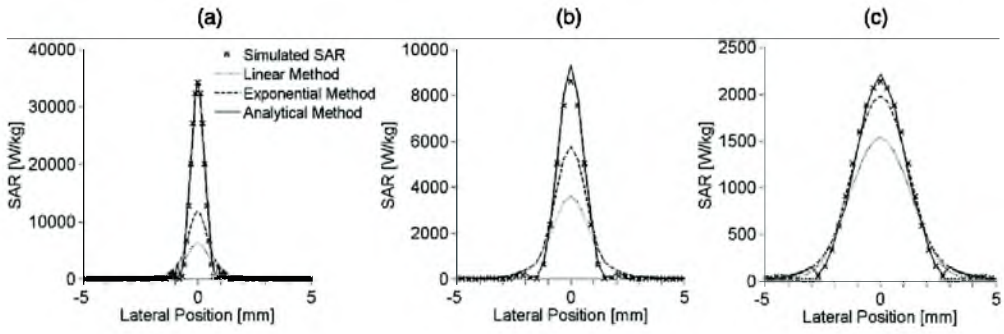

Figure 6. Lateral SAR estimation using the linear, exponential and off-axis analytical methods for (a) small, (b) medium, and (c) large focal zone sizes at the depth of maximum SAR with other parameters set at nominal values.

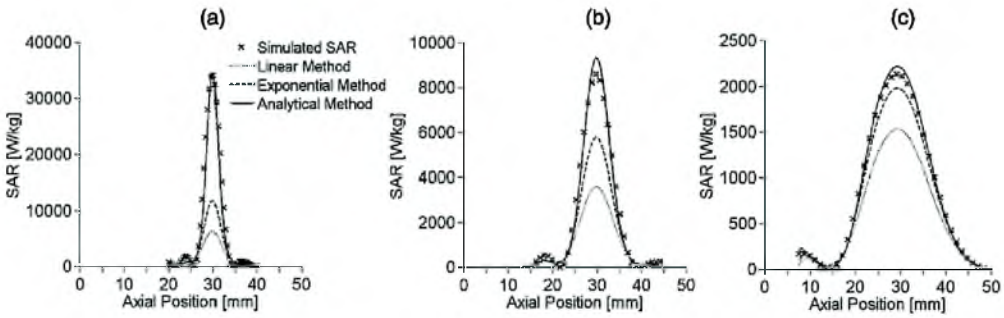

Figure 7. Axial SAR estimation using the linear, exponential and on-axis analytical methods for (a) small, (b) medium, and (c) large sized focal zones along the axis of beam propagation with other parameters set at nominal values.

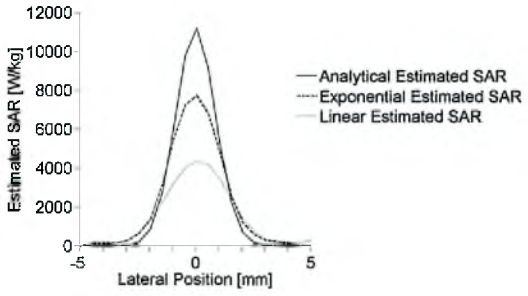

Figure 8. Lateral profiles for experimentally determined SAR at the depth of maximum heating.

4. Experimental results

4.1. Experimentally estimated SAR

Lateral SAR patterns estimated from experimental heating of the tissue-mimicking phantom are shown in figure 8 at the depth of maximum temperature elevation. The estimated lateral FWHM of the ultrasound beam is 3.08, 2.58, and 2.03 mm for the linear, exponential, and analytical fitting methods, respectively.

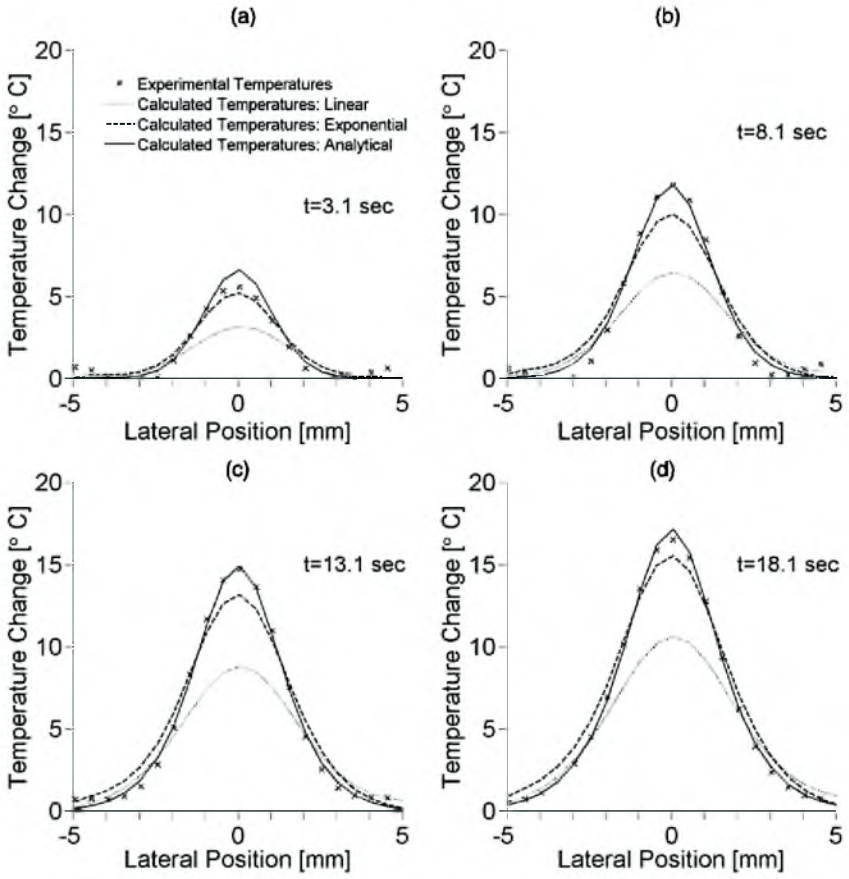

Figure 9. Lateral temperature distributions of experimental temperatures and calculated temperatures from heating patterns acquired using different SAR estimation methods at heating times of (a) 3.1 s, (b) 8.1 s, (c) 13.1 s, and (d) 18.1 s.

4.2. Experimental and simulated temperature comparisons

The lateral distributions of the experimental temperatures and calculated temperatures (based on experimentally obtained SAR values) are shown in figure 9 for four different times during the heating period at the depth of maximum temperature elevation. The analytical method for estimating SAR matches experimental FWHM of temperatures with less than $\pm 5\%$ error and has a maximum temperature error of approximately 1 °C. The linear estimation method provides a lateral FWHM 28–38% wider than experimental results and underestimates the maximum temperature by almost 6 °C, while the exponential method overestimates the lateral FWHM by 13–21% and underestimates temperatures by up to 2 °C.

5. Discussion

The analytical method clearly estimates SAR more accurately than the linear and exponential methods. Importantly, it does so very robustly, with less than 10% error- independent of beam size, tissue properties (excluding high perfusions), applied power, and fitting parameters. It has the additional advantage that it can be applied to find SAR estimates at off-axis focal zone positions and can be altered to include perfusion effects at the center of the focal zone.

Application of the standard linear SAR estimation method, while valid for applications with heating modalities with diffuse SAR patterns, should be avoided for HIFU SAR estimation except where temperature sampling intervals can be made very small. While the exponential SAR estimation method is consistently more accurate than the linear method, it is inferior when compared with the analytical results.

5.1. The standard linear method

The primary advantage of the frequently used linear method is its simplicity- it applies a single-parameter fit to the temperatures. While the assumption of linearity makes the solution simple, it also provides the prime source of error in the method. In HIFU treatments, the focal zone is so small and the spatial temperature gradients so large that conduction effects become apparent almost immediately, limiting the accuracy of the linear method.

Only when the sampling interval and total time for fit are reduced to 0.25 s, which is difficult to accomplish experimentally, is the linear SAR estimation error less than 10%. This is consistent with Parker's criterion ($4\kappa t_{tot}/\beta \leqslant 0.1$) for use of the linear approximation when estimating acoustic absorption (Parker 1985).

5.2. The exponential method

The motivation for testing the exponential method is the desire to introduce a simple model of curvature to the fitting procedure. While this solution is simple, conduction effects are not exponential in nature but vary with time as the spatial second derivative of temperature changes. Because of this, the exponential solution does not match the temperature rise as well as the analytical fit. However, with increasing focal zone size, the spatial temperature gradients are reduced, conduction losses decrease, and SAR estimates using the exponential fit are increasingly more accurate (figures 6 and 7).

Like the linear method, the exponential SAR estimation method has its lowest errors for the minimum total time for fit and in tissues with low thermal diffusivity. The improved accuracy of SAR estimations with short total times for the fit suggests that an exponential curve may be used as a reasonable approximation for the time–temperature curve for short periods of time. It should be noted that, for very short fitting times (<1 s for the nominal case), the temperature versus time curve does indeed approach linearity and attempting to apply an exponential curvature causes slight overestimation of the initial slope and SAR (figure 2(b)).

5.3. The analytical method: simulation results

At the center of the focal zone, the analytical method for estimating SAR employs a two-parameter least-squares fit to the temperature versus time data. The method assumes a 1D radial Gaussian SAR profile, while neglecting perfusion and axial conduction. Results indicate that these approximations are quite accurate for estimating SAR in HIFU if perfusion levels are less than 5 kg $(m^3\ s)^{-1}$. The analytical method yields less than 10% error at the center of the focal zone, regardless of tissue properties or experimental parameters (excluding high perfusions).

It is possible that that neglecting perfusion and axial conduction causes the slight, but consistent overestimation in SAR using the analytical method. Since these two heat loss mechanisms are not accounted for by the analytical solution, the analytical method's fitting process compensates by increasing the model's radial conduction, which is determined by the fitting parameter D. For each of the simulations, the estimated parameter D was larger than

its true value. From its definition, $D = 4\kappa/\beta$, overestimating D implies that either the thermal diffusivity has increased or the Gaussian variance, a measure of the beam width, has decreased. Either of these changes would cause an increase in radial conduction. Overestimation of D with increased SAR at the center of the focal zone generates the temperature gradients necessary to account for perfusion and axial heat losses when only radial conduction is present. Though incorrect physically, this compensation provides SAR results that are significantly more accurate than the linear and exponential methods. Only for very short fitting times (<1 s) and larger focal zones (lateral FWHM> 2.6 mm) can the exponential and linear methods provide SAR estimates comparable in accuracy to the analytical solution.

The acquisition time (i.e. sampling interval) of MRTI sequences can range from approximately one second to greater than five seconds, depending upon the desired field of view, spatial resolution, and signal-to-noise ratio requirements. Figure 2 shows that the analytical method is essentially independent of the sampling interval t_s. This result suggests that by using the analytical method, HIFU researchers using MRTI may implement longer acquisition times to improve spatial resolution without significantly affecting SAR estimation accuracy.

Many tissues of interest in HIFU thermal therapies have low perfusion levels. Resting muscle and fat, for example, each have perfusion levels less than 0.65 kg $(m^3\ s)^{-1}$. In these tissues, using the simple analytical solution will provide SAR estimates accurate to within 10%. However, other tissues such as the kidney may have perfusion levels up to, and even exceeding, 50 kg $(m^3\ s)^{-1}$ (Duck 1990). In such cases, it is advantageous to use the analytical solution including perfusion developed by Kress. While this solution is only available at the center of the focal zone, SAR errors using this analytical fit remain less than 10% even for very high perfusion rates (figure 4).

Each of the estimation methods requires knowledge of the tissue specific heat. Errors in specific heat values will alter SAR estimation accuracy in a linear fashion. This is motivation for obtaining patient specific property values for HIFU treatment planning.

5.4. The analytical method: experimental results

Applying the estimation methods to experimental data verified the simulation results that the magnitude and spatial distribution of SAR can be accurately estimated from temperature versus time data with the analytical method.

Using the MRTI temperature field, the beam axis location is easily identified, and therefore every voxel's radial position r can also be accurately determined with uncertainty in r no greater than the in-plane voxel dimensions. Knowledge of r provides additional information to the off-axis analytical solution so the thermal diffusivity, κ, and ultrasound Gaussian variance, β, can be estimated directly (see section 2.2.3). These estimates are most accurate at the depth of maximum SAR, where the model's approximations are most valid. From the experimental data, the thermal diffusivity of the ATS phantom was estimated at $1.49 \times 10^{-7}\ m^2\ s^{-1}$, 7.2% higher than the value given by the manufacturer. While κ was slightly overestimated, the fit for β appears to be reasonably accurate since lateral distributions of the experimental and calculated temperatures match to $\pm 5\%$ throughout the heating. Given the discussion on parameter D in section 5.3, these results were expected.

There are several advantages to fitting temperature data for several voxels simultaneously in the experimental validation. Computationally, the simultaneous parameter estimation at each of the 64 axial depths reduced the number of fits necessary to estimate SAR for the entire 3D field from ~400 000 to 64, thus reducing computation time from several hours to approximately

one minute. Additionally, using simultaneous parameter estimation significantly reduces the effects of noise that are present when estimates are generated for each voxel independently.

The primary disadvantage of using data from many locations for simultaneous parameter estimation is that the estimated SAR is constrained to a Gaussian distribution at each axial depth. This is a very good approximation near the center of the focal zone but becomes increasingly tenuous at axial depths away from the center. This approximation may also be less valid when estimating SAR in inhomogeneous tissue or when the beam is steered significantly in the lateral direction. Finally, because the assumption of a Gaussian distribution quickly forces the estimated SAR to zero at locations lateral to the focal zone, this method is not effective in quantifying the effects of ultrasound side lobes, grating lobes, and scattering outside the focus.

In addition to improving SAR estimation, the analytical temperature solutions (12), (16), and (20) could be applied in other ways to improve HIFU treatments. For example, the solutions could be used in model predictive filtering techniques (Todd *et al* 2010) to improve MRI temperature coverage and increase both spatial and temporal resolution. In a real-time controller, forward predicting the temperatures with analytical solutions could be applied for thermal dose optimization. The solutions could also help to eliminate the effects of temperature acquisition artifacts, such as viscous heating (Goss *et al* 1977).

Assumptions necessary to the experimental validation are that the MR temperatures are accurate, the published and measured thermal properties used in thermal models are accurate, and that the FD thermal model accurately represents the heating process in the treatment volume. Quantifying effects of MR noise, temporal and spatial averaging, uncertainty in power-on time, and partial volume effects is left for future studies. The effects of acoustic non-linearity and tissue inhomogeneity on SAR estimation were also not assessed in this study. However, if these effects do not alter the nearly Gaussian nature of the ultrasound beam, the analytical method should remain accurate.

6. Conclusion

The primary finding of this study is that the 1D radial Gaussian analytical solution for estimating SAR is a significant improvement over the standard linear method and the simple exponential method. The analytical method estimates SAR with a high degree of accuracy, independent of beam size, tissue properties, power level, and temperature sampling intervals. At low perfusion levels, the simple analytical solution can be used to acquire SAR estimates at all axial and lateral locations. For highly perfused tissues, the extended analytical solution including perfusion provides accurate SAR estimates at the center of the focal zone. When applying the method to experimental data, noise effects in SAR estimation can be significantly reduced by performing a simultaneous parameter estimation to the temperature versus time data for longer times and for several locations at each axial depth. Using this method also provides estimates for the thermal diffusivity and ultrasound Gaussian variance. The improved analytical SAR estimation method should be useful for the comparison of results from different HIFU studies and for the validation of SAR predictive software used in patient treatment planning of HIFU thermal therapies.

Acknowledgments

The authors gratefully acknowledge support from Siemens Healthcare AG, the FUS Foundation, the Ben and Iris Margolis Foundation, and NIH grants R01 CA87785 and R01

CA134599. We also thank Dr Nick Todd and Dr Dennis Parker for their contribution to the work.

References

Arkin H, Holmes K R, Chen M M and Bottje W G 1986 Thermal pulse decay method for simultaneous measurement of local thermal conductivity and blood perfusion: a theoretical analysis *J. Biomech. Eng.* **108** 208–14

Cheng H L and Plewes D B 2002 Tissue thermal conductivity by magnetic resonance thermometry and focused ultrasound heating *J. Magn. Reson. Imaging* **16** 598–609

Cheng K S and Roemer R B 2005 Blood perfusion and thermal conduction effects in Gaussian beam, minimum time single-pulse thermal therapies *Med. Phys.* **32** 311–7

Damianou C A, Sanghvi N T, Fry F J and Maass-Moreno R 1997 Dependence of ultrasonic attenuation and absorption in dog soft tissues on temperature and thermal dose *J. Acoust. Soc. Am.* **102** 628–34

De Poorter J D, De Wagter C, De Deene Y, Thomsen C, Stahlberg F and Achten E 1995 Noninvasive MRI thermometry with the proton resonance frequency (PRF) method: *in vivo* results in human muscle *Magn. Reson. Med.* **33** 74–81

Diederich C J, Clegg S and Roemer R B 1989 A spherical source model for the thermal pulse decay method of measuring blood perfusion: a sensitivity analysis *J. Biomech. Eng.* **111** 55–61

Dragonu I, de Oliveira P L, Laurent C, Mougenot C, Grenier N, Moonen C T W and Quesson B 2009 Non-invasive determination of tissue thermal parameters from high intensity focused ultrasound treatment monitored by volumetric MRI thermometry *NMR Biomed.* **22** 843–51

Duck F A 1990 *Physical Properties of Tissue: A Comprehensive Reference Book* (New York: Academic)

Gladman A S, Davidson S R H, Easty A C, Joy M L and Sherar M D 2004 Infrared thermographic SAR measurements of interstitial hyperthermia applicators: errors due to thermal conduction and convection *Int. J. Hyperthermia* **20** 539–55

Goss S A, Cobb J W and Frizzell L A 1977 Effect of beam width and thermocouple size on the measurement of ultrasonic absorption using the thermoelectric technique *IEEE Ultrason. Symp. Proc.* 206–11

Guy A W, Lehmann J F and Stonebridge J B 1974 Therapeutic applications of electromagnetic power *Proc. IEEE* **62** 55–75

International Commission on Radiation Units and Measurements 1998 *ICRU Report 61: Tissue Substitutes, Phantoms and Computational Modelling in Medical Ultrasound (ICRU Publications, Bethesda, MD)*

Ishihara Y, Calderon A, Watanabe H, Okamoto K, Suzuki Y, Kuroda K and Suzuki Y 1995 A precise and fast temperature mapping using water proton chemical shift *Magn. Reson. Med.* **33** 814–23

Kharalkar N M, Hayes L J and Valvano J W 2008 Power-pulse integrated-decay technique for the measurement of thermal conductivity *Meas. Sci. Technol.* **19** 075104

Kress R and Roemer R 1987 A comparative analysis of thermal blood perfusion measurement techniques *J. Biomech. Eng.* **109** 218–25

Mahoney K, Fjield T, McDannold N, Clement G and Hynynen K 2001 Comparison of modelled and observed *in vivo* temperature elevations induced by focused ultrasound: implications for treatment planning *Phys. Med. Biol.* **46** 1785–98

Nyborg W L 1988 Solutions of the bio-heat transfer equation *Phys. Med. Biol.* **33** 785–92

Parker K J 1983 The thermal pulse decay technique for measuring ultrasonic absorption coefficients *J. Acoust. Soc. Am.* **74** 1356–61

Parker K J 1985 Effects of heat conduction and sample size on ultrasonic absorption measurements *J. Acoust. Soc. Am.* **77** 719–25

Payne A, Vyas U, Todd N, de Bever J, Christensen D A and Parker D L 2011 The effect of electronically steering a phased array ultrasound transducer on near-field tissue heating *Med. Phys.* **38** 4971–81

Pennes H H 1948 Analysis of tissue and arterial blood temperatures in the resting human forearm *J. Appl. Physiol.* **1** 93–122

Roemer R B, Fletcher A M and Cetas T C 1985 Obtaining local SAR and blood perfusion data from temperature measurements: steady state and transient techniques compared *Int. J. Radiat. Oncol. Biol. Phys.* **11** 1539–50

Samaras T, van Rhoon G C and Sahalos J N 2002 Theoretical investigation of measurement procedures for the quality assurance of superficial hyperthermia applicators *Int. J. Hyperthermia* **18** 416–25

Sherar M D, Gladman A S, Davidson S R H, Trachtenberg J and Gertner M R 2001 Helical antenna arrays for interstitial microwave thermal therapy for prostate cancer: tissue phantom testing and simulations for treatment *Phys. Med. Biol.* **46** 1905–18

Todd N, Payne A and Parker D L 2010 Model predictive filtering for improved temporal resolution in MRI temperature imaging *Magn. Reson. Med.* **63** 1269–79

Todd N, Vyas U, de Bever J, Payne A and Parker D L 2011 The effects of spatial sampling choices on MR temperature measurements *Magn. Reson. Med.* **65** 515–21

Valvano J W, Allen J T and Bowman H F 1984 The simultaneous measurement of thermal conductivity, thermal diffusivity, and perfusion in small volumes of tissue *J. Biomech. Eng.* **106** 192–7

Vyas U and Christensen D A 2012 Ultrasound beam simulations in inhomogeneous tissue geometries using the hybrid angular spectrum method *IEEE Trans. Ultrason. Ferroelectr. Freq. Control* **59** 1093–100

Vyas U, Todd N, Payne A, Parker D and Christensen D A 2010 Non-invasive ultrasound tissue property measurement using MRI temperature maps of low-powered heating *Ann. Meet. of Soc. Thermal Med. (Clearwater, FL)* pp 102

Zderic V, Keshavarzi A, Andrew M A, Vaezy S and Martin R W 2004 Attenuation of porcine tissues *in vivo* after high-intensity ultrasound treatment *Ultrasound Med. Biol.* **30** 61–6

CHAPTER 3

EFFECTS OF MRTI SAMPLING CHARACTERISTICS ON ESTIMATION OF HIFU SAR AND TISSUE THERMAL DIFFUSIVITY

Reprinted with permission from

IOP Publishing.

Dillon CR, Todd N, Payne A, Parker DL, Christensen DA, Roemer RB (2013)

Effects of MRTI sampling characteristics on estimation of

HIFU SAR and tissue thermal diffusivity.

Phys Med Biol 58: 7291-7307.

IOP Publishing Physics in Medicine and Biology
Phys. Med. Biol. **58** (2013) 7291–7307 doi:10.1088/0031-9155/58/20/7291

Effects of MRTI sampling characteristics on estimation of HIFU SAR and tissue thermal diffusivity

C R Dillon[1], N Todd[2], A Payne[2,3], D L Parker[2], D A Christensen[1,4] and R B Roemer[1,2,3]

[1] Department of Bioengineering, University of Utah, 36 S Wasatch Drive Rm 3100, Salt Lake City, UT 84112, USA
[2] Department of Radiology, University of Utah, 729 S Arapeen Dr, Salt Lake City, UT 84108, USA
[3] Department of Mechanical Engineering, University of Utah, 50 S Central Campus Drive, Salt Lake City, UT 84112, USA
[4] Department of Electrical and Computer Engineering, University of Utah, 50 S Central Campus Drive, Salt Lake City, UT 84112, USA

E-mail: christopher.dillon@utah.edu

Received 22 March 2013, in final form 25 July 2013
Published 26 September 2013
Online at stacks.iop.org/PMB/58/7291

Abstract

While the non-invasive and three-dimensional nature of magnetic-resonance temperature imaging (MRTI) makes it a valuable tool for high-intensity focused ultrasound (HIFU) treatments, random and systematic errors in MRTI measurements may propagate into temperature-based parameter estimates used for pretreatment planning. This study assesses the MRTI effects of zero-mean Gaussian noise (SD = 0.0–2.0 °C), temporal sampling (t_{acq} = 1.0–8.0 s), and spatial averaging (Res = 0.5–2.0 mm isotropic) on HIFU temperature measurements and temperature-based estimates of the amplitude and full width half maximum (FWHM) of the HIFU specific absorption rate and of tissue thermal diffusivity. The ultrasound beam used in simulations and *ex vivo* pork loin experiments has lateral and axial FWHM dimensions of 1.4 mm and 7.9 mm respectively. For spatial averaging simulations, beams with lateral FWHM varying from 1.2–2.2 mm are also assessed. Under noisy conditions, parameter estimates are improved by fitting to data from larger voxel regions. Varying the temporal sampling results in minimal changes in measured temperatures (<2% change) and parameter estimates (<5% change). For the HIFU beams studied, a spatial resolution of 1 × 1 × 3 mm^3 or smaller is required to keep errors in temperature and all estimated parameters less than 10%. By quantifying the errors associated with these sampling characteristics, this work provides researchers with appropriate MRTI conditions for obtaining estimates of parameters essential to pretreatment modeling of HIFU thermal therapies.

1. Introduction

For high-intensity focused ultrasound (HIFU) treatments to be broadly accepted in the clinic, progress must be made in patient-specific treatment planning, monitoring and control. A key component to this goal is accurate modeling of the bioheat transfer equation (BHTE) (Pennes 1948), for which investigators need accurate knowledge of the magnitude and spatial distribution of the ultrasonic specific absorption rate (SAR) and of tissue thermal properties (Roemer 1999). However, due to variations among and within different organs, variability across individuals, and limitations of treatment hardware or prediction software (Mahoney *et al* 2001, Payne *et al* 2011), the modeled SAR values and table thermal parameters used in the BHTE may cause significant errors in temperature calculations used to predict thermal dose.

Previous work has shown that a new analytical method for obtaining HIFU SAR from experimental temperature data is significantly more accurate than the traditional linear method (Guy *et al* 1974, Roemer *et al* 1985) and will be a valuable tool in assessing and improving SAR predictive software (Dillon *et al* 2012). This method estimates the amplitude of the focal SAR as well as its lateral full width at half maximum (FWHM). In addition to providing estimates for SAR amplitude and width, the method generates an estimate for thermal diffusivity of the tissue in the focal region. Utilizing these improved parameter estimates in the BHTE during therapy planning, monitoring and control has the potential to improve the efficacy and efficiency of HIFU thermal therapies.

In the past, estimation of thermal and acoustic properties from experimental temperatures was accomplished using thermocouples or thermistor probes (Guy *et al* 1974, Goss *et al* 1977, Parker 1983, 1985, Valvano *et al* 1984, Roemer *et al* 1985). More recent investigators have used thermistors (Kharalkar *et al* 2008) as well as infrared imaging (Milner *et al* 1996, Telenkov *et al* 2001, Bobkova *et al* 2010, Giridhar *et al* 2012), backscattered ultrasound imaging (Anand and Kaczkowski 2008, 2009) and magnetic-resonance imaging (Cheng and Plewes 2002, Dragonu *et al* 2009) for estimation of ultrasound intensities and thermal properties. The use of magnetic-resonance temperature imaging (MRTI) for HIFU thermal therapies and estimation of relevant parameters is extremely valuable since it can provide fully three-dimensional non-invasive temperature measurements in and around the focal zone. By utilizing the extensive data available from MRTI, significant improvements in estimating SAR profiles and tissue thermal properties should be possible.

Unfortunately, the MRTI acquisition process can introduce errors into temperature measurements which may be propagated into temperature-based estimations of tissue properties and treatment parameters, including SAR and thermal diffusivity. First, unavoidable noise in MR temperature measurements can have a marked effect on the accuracy of estimation methods. Second, the MR acquisition process necessitates measuring continuously changing temperatures over a finite time period and combining them into measurements ascribed to discrete time points. Finally, the spatially distributed temperatures are averaged to create discrete temperature measurements for each voxel. This spatial averaging may cause misrepresentation of temperatures and has already been assessed for its effect on temperature and thermal dose calculations (Todd *et al* 2011, O'Neill *et al* 2012).

This paper presents simulation and experimental results assessing the effects of MRTI noise, temporal sampling, and spatial averaging on HIFU temperature measurements and on estimation of SAR amplitude and FWHM, and thermal diffusivity. These three parameters are estimated using the analytical method of Dillon *et al* 2012. Several HIFU power deposition patterns are assessed with lateral FWHM values ranging from 1.2 to 2.2 mm, making these results applicable to a range of HIFU focal beam sizes and experimental conditions.

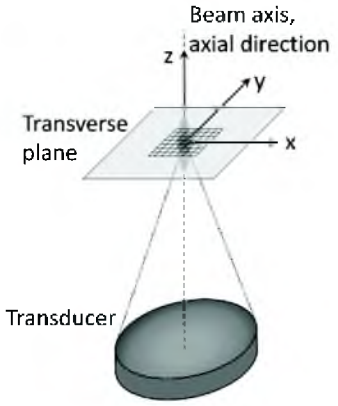

Figure 1. Orientation of coordinate axes in relation to the ultrasound transducer and focal zone for simulations and experiments. The 7 × 7 voxel-fitting region used in each transverse plane and centered on the beam axis is also shown.

By quantifying the errors associated with MRTI sampling characteristics, this work should provide researchers with an appropriate set of conditions for obtaining non-invasive accurate estimates of parameters essential to pretreatment modeling of HIFU thermal therapies.

2. Methods

2.1. Simulation of SAR and temperature data

Simulated SAR patterns were generated by the hybrid angular spectrum method (Vyas and Christensen 2012) applied to a 256-element phased-array HIFU transducer and system (Imasonics, Besancon, France and Image Guided Therapy, Bordeaux, France) that was also used in experiments. The transducer had an aperture of 14.5 cm, frequency of 1 MHz, and radius of curvature of 13 cm. The simulated transducer power output was 10 acoustic watts focused 3 cm deep in the homogeneous tissue model, which had a tissue speed of sound of 1500 m s^{-1}, density of 1000 kg m^{-3}, and acoustic pressure attenuation of 5.0 Np m^{-1}. These fixed values were used to generate the reference standard results for assessing the accuracy of estimates made from temperature data. The simulated SAR pattern had a lateral and axial FWHM of 1.4 mm and 7.9 mm, respectively, with a maximum SAR value of 15 300 W kg^{-1}. In both simulations and experiments, axial refers to the beam propagation direction (z) and terms lateral or transverse refer to directions perpendicular to beam propagation (x-y or r), as seen in figure 1.

For each simulated SAR pattern, the BHTE was implemented in an explicit finite-difference (FD) solver to calculate temperatures for 32 s of heating. Thermal parameters used in the model were thermal conductivity of 0.5 W $(m\ °C)^{-1}$, specific heat of 3500 J $(kg\ °C)^{-1}$, and density of 1000 kg m^{-3}; thus, the thermal diffusivity reference value was $\kappa = 1.43 \times 10^{-7}\ m^2\ s^{-1}$. Because the method will ultimately be applied *in vivo*, a Pennes perfusion coefficient of 1.0 kg $(m^{-3}\ s^{-1})$ was used in all simulations.

2.2. Simulation of MRTI noise

In simulations for the noise analysis, an isotropic grid spacing of 0.3 mm was used for generating FD temperatures with a temporal resolution of 0.1 s to maintain numerical stability.

Those temperatures were then undersampled to a 4.0 s temporal resolution, which is more representative of MRTI.

Following the undersampling of temperatures, zero-mean Gaussian noise was introduced to the simulated temperature data with standard deviations (SD) ranging from 0.5 °C to 2.0 °C, levels representative of noise in MRTI. The noise-free case was also analyzed for a reference comparison.

The estimation of parameters from these simulated temperatures is described fully in section 2.5. Those estimations typically utilized a 7×7 voxel region of temperature-versus-time data centered about the beam axis in the transverse plane (figure 1). For the noisy temperature data, the parameters were also estimated using temperature data from 3×3, 5×5, 9×9, and 11×11 voxel-fitting regions. Noise introduction and parameter estimation was repeated 400 times for each noise level.

2.3. Simulation of MR temporal sampling

For temporal sampling studies, the 0.3 mm isotropic FD grid spacing was again used in temperature simulations for consistency. While this spatial resolution would be difficult to obtain experimentally, it is still appropriate because simulations for temporal sampling are independent of the FD grid spacing. In these simulations, the FD time step was varied to alter the temporal sampling as discussed below.

Measurements for a single 3D volume of MR temperature images may take several seconds to acquire. Temporal sampling is a product of taking temperature measurements over this finite time period and attributing those temperatures to a single time point. The traditional method in which temperature data are temporally acquired and combined for proton resonant frequency MRTI (De Poorter *et al* 1995, Ishihara *et al* 1995) can be simulated with FD and Fourier transform techniques.

First, temperature changes for a single FD time step (dt) are evaluated in a thermal model of the BHTE. The temperature changes are converted to phase changes and a constant magnitude (which does not affect temperature calculations) is added to the phase data to generate complex image data. Taking the Fourier transform of these complex images converts them to k-space. The data for the first line of k-space in the phase encoding direction are saved. The next time step of the thermal model is calculated, temperatures are again converted to k-space, and the second line of the k-space phase encoding direction is saved. The process is repeated until all of k-space is full. After a complete set of k-space has been saved, taking the inverse Fourier transform of those data will yield a complex image which can be converted to temporally sampled temperatures. Since the most significant information is found at the center of k-space, the temperature data are assigned to the simulation time at which data for the center of k-space was modeled and saved. With the next time step of the FD model, the first line of a new set of k-space data is saved and the process begins anew.

By varying the model time step dt, which is analogous to the MRTI pulse-sequence repetition time TR, the simulated MR acquisition time (t_{acq}) can be altered as

$$t_{acq} = \mathrm{d}t \cdot nY, \tag{1}$$

where nY represents the number of k-space lines in the phase encoding direction. In this analysis, the time step dt was varied so that acquisition times of one to 8 s could be achieved, times representative of the current capabilities of 2D and 3D MRTI. These simulations assume that the ultrasound start time is synchronized with the start of MR image acquisition, which is easily accomplished by pulse-sequence triggering in the MR-guided HIFU system.

The parameter estimations for temporal sampling simulations, described in detail in section 2.5, used as many data points from the temperature-versus-time curves as were available

for the 32 s of heating. Note that with longer acquisition times fewer data are available for fitting: for $t_{acq} = 1.0$ s, 32 data points are available from each temperature-versus-time curve, whereas for $t_{acq} = 8.0$ s, only four points are available in each curve.

2.4. Simulation of MR spatial averaging

For spatial averaging, the initial grid spacing for temperature simulations was set at 0.1 mm isotropic. The time step of the FD solver was 0.01 s for stability, and the data were undersampled to 4.0 s per measurement. These data were then spatially averaged with an algorithm that mimics the spatial averaging of MRTI (Todd *et al* 2011). Since the size of the focal zone plays a significant role in the errors induced by spatial averaging, simulations were generated for several different focal zone sizes with the lateral FWHM measurements varying from 1.2 to 2.2 mm in addition to the reference FWHM of 1.4 mm. Altering the size of the reference focal zone with the same ultrasound transducer was accomplished by adjusting the simulated transducer frequency while keeping the total attenuation constant at 5.0 Np m^{-1}. While adjusting the frequency to alter the focal zone size would not normally be applied in practice, doing so in simulations provides a variety of ultrasound power deposition patterns that could be used to assess errors of HIFU systems with different focal zone sizes.

Simulating the spatial averaging of MRTI requires temperature simulation data with very fine spatial resolution (0.1 mm isotropic). After changing the simulated temperatures to phase data, adding a constant magnitude term, and converting into k-space with a Fourier transform, the edges of k-space are masked to zeros. This masking causes the loss of the high frequency data in the k-space domain, which reduces the spatial resolution of the temperatures. In each direction that is masked, the ratio of the total original lines to the remaining unmasked lines will be the ratio of the new spatial resolution to the initial resolution. For example, a matrix size of 200 × 200 × 300 at an initial resolution of 0.1 mm isotropic could be masked with zeros except for the central 10 × 10 × 15 region, resulting in a resolution of 2.0 mm isotropic grid spacing since 200/10 = 300/15 = 2.0/0.1. Taking the inverse Fourier transform will convert the zero-filled k-space data back to complex images from which spatially averaged temperatures are calculated.

By zero-filling the k-space data, the spatially averaged temperature data will have the same grid spacing as the initial data but the spatial resolution will be altered. Essentially, the lower resolution data is being zero-filled interpolated so that the grid spacing remains unchanged.

For spatially averaged data, the parameter estimation methods used a subset of the final 0.1 mm grid spacing data. Data for the 7 × 7 voxel-fitting region were taken every 0.3 mm centered at the beam axis so the total region of data fitting was consistent for assessment of simulated noise, temporal sampling, and spatial averaging effects.

Since focused ultrasound beams are longer in the axial direction than in the transverse direction, the spatial distribution of temperature varies less in the axial direction. Because of this, high-resolution imaging in the axial direction is less important than in the transverse plane. Using a different ratio for the zero-filled mask in the *k-z* direction will change the resolution of the axial slices. In this study, after determining the isotropic resolution required for the reference focal zone, the voxel dimension in the *z*-direction was increased to assess effects of changing axial resolution while keeping the lateral voxel dimensions constant.

2.5. Estimation of SAR amplitude and FWHM, and thermal diffusivity

The analytical temperature solution used for the temperature-based parameter estimations assumes a 1D radial Gaussian heating pattern (Parker 1983, 1985, Kress and Roemer 1987,

Cheng and Plewes 2002, Dragonu *et al* 2009, Anand and Kaczkowski 2008, 2009) and that axial conduction and perfusion effects are negligible (Dillon *et al* 2012). The solution, at non-zero radial positions in the transverse plane, during heating is given by

$$T(r,t) = C\left(\frac{\beta}{4\kappa}\right)\left[Ei\left(\frac{-r^2}{\beta}\right) - Ei\left(\frac{-r^2}{\beta(1+4\kappa t/\beta)}\right)\right], \tag{2}$$

where $C = 2\alpha I_0/(\rho c_p)$ and Ei represents the exponential integral. In term C, α represents the tissue acoustic pressure absorption coefficient, I_0 is the ultrasonic intensity on the beam axis, while ρ and c_p are the tissue density and specific heat, respectively. When the radial distance r from the beam axis and the time t since the onset of ultrasound heating are known, a least-squares three parameter fit of equation (2) to the simulated or experimental temperature data is possible by concurrently optimizing C, κ, and β. The fitting process utilizes temperatures from a 7 × 7 voxel-fitting region in a single transverse plane centered about the beam axis. The 7 × 7 region was selected because it includes data over the entire width of the ultrasound beam. Each of the 49 temperature-versus-time curves is fit to equation (2) simultaneously in a least-squares manner, generating a single estimate for C, the thermal diffusivity κ, and the Gaussian variance β at each depth. Stepping through each transverse plane in the axial direction, the estimation process is repeated through the entire focal zone.

Because SAR is directly related to the initial slope of temperature rise, by taking the first derivative of equation (2) evaluated at $t = 0$ and $r = 0$, the maximum SAR amplitude in each transverse plane can be estimated from

$$\mathrm{SAR}_{\max} = c_p C. \tag{3}$$

The relationship between the Gaussian variance β and the estimated lateral FWHM of the SAR is given by

$$\mathrm{FWHM} = 2\sqrt{\beta \ln 2}. \tag{4}$$

Finally, an estimate for the tissue thermal diffusivity is found directly from fitting parameter κ at the depth of the global maximum SAR value, where the approximation of no axial conduction is most valid.

In the estimation of SAR amplitude, the only information required in addition to the temporal and spatial distribution of temperatures is the tissue specific heat capacity, which ultimately divides out when implemented in the bioheat equation. The tissue thermal diffusivity and FWHM of the ultrasound beam can be determined from the temperature data alone.

Due to the approximations of the 1D radial Gaussian model, there are errors inherent to the estimation method prior to introduction of MR effects (Dillon *et al* 2012). Using this method in the absence of MR noise, temporal sampling and spatial averaging, for the reference focal zone size (lateral FWHM = 1.4 mm, axial FWHM = 7.9 mm), maximum SAR is overestimated by 6–9%, FWHM is underestimated by 5–7%, and thermal diffusivity is overestimated by 2–6%. The effects of MR noise, temporal sampling, and spatial averaging upon estimation of SAR amplitude and FWHM, and diffusivity should therefore be considered with this initial offset in mind.

2.6. Experimental data

HIFU heating experiments were performed in *ex vivo* pork loin using the MR-compatible 256-element phased-array ultrasound system that was modeled in the simulation study, but operating at a power output of 8.8 acoustic watts. The maximum heating occurred 4.8 cm deep in the pork loin at the geometric focus of the ultrasound transducer. Deionized, degassed water coupled the ultrasound transducer to the pork loin sample.

For the reference case, images were acquired with a pair of two-channel surface coils built in-house at $1 \times 1 \times 3$ mm^3 resolution in a 3T Siemens Trio MRI scanner using a standard 3D segmented echo planar imaging (EPI) sequence. Other imaging parameters included TR/TE = 35/11 ms, FA = 15°, bandwidth: 766 Hz pixel^{-1}, matrix: $192 \times 108 \times 10$ (8 slices plus 25% slice oversampling), EPI factor = 9, and a temporal resolution of 4.2 s per image volume. Imaging slices were oriented perpendicular to the axis of beam propagation in the transverse plane. Ultrasound heating was synchronized to begin with the acquisition of the fifth MR image and measurement times were assigned to the halfway point of each MR acquisition. The total heating time was 42 s. Temperatures were reconstructed using a reference-less (Rieke *et al* 2004) proton resonance frequency method (De Poorter *et al* 1995, Ishihara *et al* 1995) and post-processed with zero-filled interpolation to yield 0.5 mm isotropic voxel spacing (Todd *et al* 2011).

To confirm both system stability and that the pork loin's thermal and acoustic properties were unchanged through the experiment, a total of four reference runs were interleaved between the heating runs used to assess the effects of temporal sampling and spatial averaging. Final reference results are combined and presented as the mean and standard deviation of these runs. A cooling period of 6–10 min was utilized between each heating run to ensure a uniform baseline temperature profile at the start of each ultrasound heating. Because the estimation method is based on changes in temperature, any increase in the baseline temperature from thermal accumulation in the tissue should not affect results.

To assess spatial averaging changes, the reference field of view in the lateral plane was doubled. This resulted in a spatial resolution of $2 \times 2 \times 3$ mm^3 while all other ultrasound and MR parameters were unchanged. To demonstrate effects of varied temporal sampling, the matrix size was increased to $192 \times 162 \times 10$ (8 slices plus 25% slice oversampling) while maintaining the reference spatial resolution, thus altering the temporal resolution to $t_{acq} = 6.3$ s per image volume. In this case, the total heating time was 44 s, slightly longer than the reference heating time. All other imaging and ultrasound parameters were kept the same as the reference case, and each set of temperature data was post-processed with zero-filled interpolation to 0.5 mm isotropic voxel spacing. The sampling characteristics of these MRTI data were selected to represent a practical and reasonable set of conditions that would be encountered in clinical, patient-specific applications.

In all cases, the axis of beam propagation ($r = 0$) was found in each transverse slice by identifying the peak of a least-squares Gaussian fit to the radial temperature data from all images acquired during heating. Radial distances from the axis of beam propagation to the center of voxels in a square 7×7 region of interest (3.5×3.5 mm^2 centered on the beam axis) provided values for r in equation (2). At each depth, the 49 temperature-versus-time curves were fit with equation (2) simultaneously, minimizing the least-squares difference for all voxels at once and generating a single (planar) estimate for each parameter C, κ, and β. Assuming a pork specific heat of 2760 J (kg °C)$^{-1}$, the SAR amplitude was calculated from equation (3) and the FWHM was estimated using equation (4). The tissue thermal diffusivity was determined by parameter κ at the depth of the global maximum SAR.

3. Results

3.1. Simulated temperature-versus-time curves at maximum SAR location

Figures 2–4 show how noise, temporal sampling and spatial averaging, respectively, affect temperature-versus-time curves at the location of maximum SAR for the simulated reference case. In each plot, the unaveraged, noiseless temperatures are shown with dashed lines.

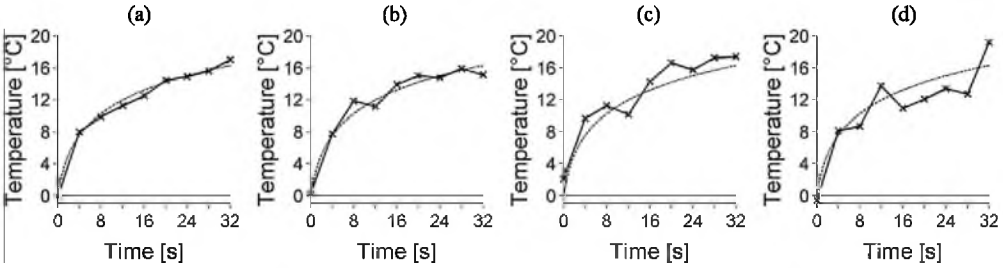

Figure 2. Varying noise levels in simulated temperature-versus-time curves at the center of the focal zone. The standard deviation of the noise is (a) 0.5 °C, (b) 1.0 °C, (c) 1.5 °C, and (d) 2.0 °C. The dashed line represents the noiseless and unsampled FD temperature-versus-time curve.

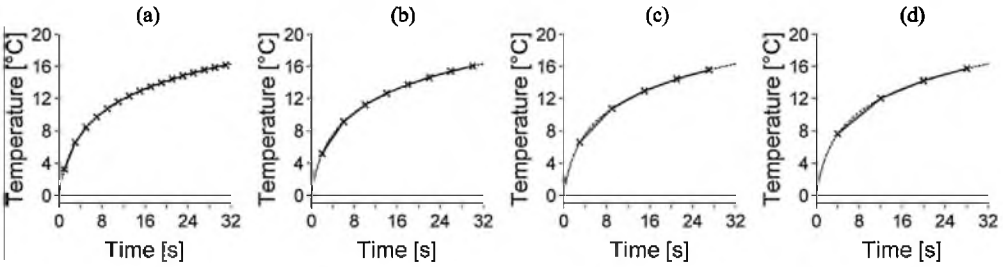

Figure 3. Temporal sampling effects on simulated temperature-versus-time curves at the center of the focal zone. The simulated MR acquisition time is (a) 2 s, (b) 4 s, (c) 6 s, and (d) 8 s. The unaveraged FD temperature-versus-time curve is shown as a dashed line.

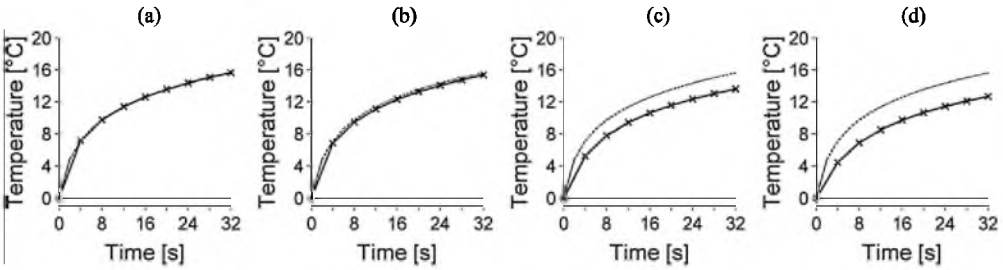

Figure 4. Spatial averaging effects on simulated temperature-versus-time curves at the center of the focal zone. The simulated isotropic spatial resolution is (a) 0.5 mm, (b) 1.0 mm, (c) 1.5 mm, and (d) 2.0 mm. The unaveraged FD temperature-versus-time curve is shown as a dashed line.

3.2. Parameter estimation: MRTI noise simulations

Errors in the estimated maximum SAR, SAR FWHM, and thermal diffusivity for 400 simulations of noisy temperature data at each noise level are shown in figure 5. The horizontal line within each box represents the median SAR error and box boundaries indicate the 25th and 75th percentiles. Whiskers extend to the most extreme data values or 1.5 times the interquartile range (IQR). Any values beyond 1.5 times the IQR are outliers marked with a plus sign. In each case, as noise levels increase, the spread of parameter estimation values also increases.

Figures 5(a)–(c) use temperature-versus-time data from a 3 × 3 voxel-fitting region simultaneously for each estimation while figures 5(d)–(f) use a 7 × 7 voxel-fitting region centered on the beam axis. For high levels of noise (SD = 2 °C), table 1 shows that increasing

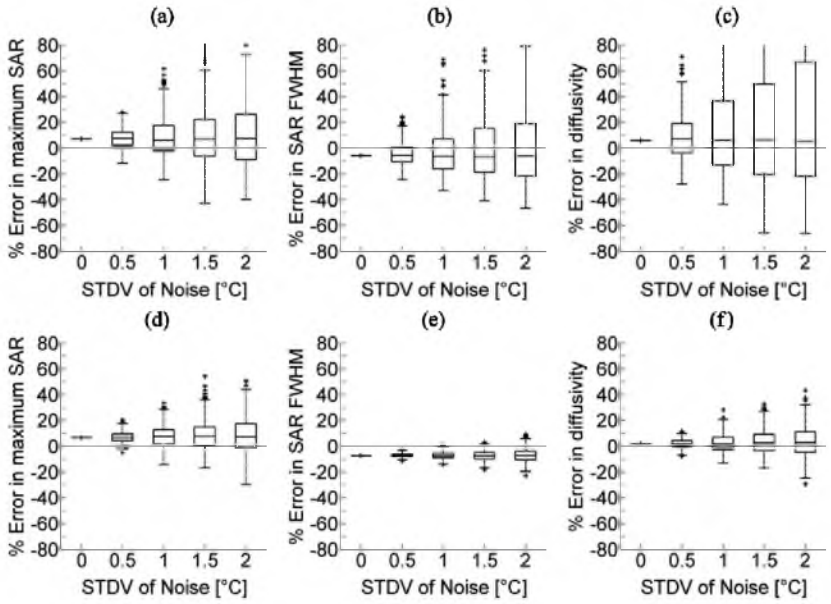

Figure 5. Effects of simulated MR noise on parameter estimation of (a) and (d) maximum SAR, (b) and (e) SAR FWHM, and (c) and (f) thermal diffusivity. Figures 4(a)–(c) use temperature data from a 3 × 3 voxel-fitting region while figures 4(d)–(f) use temperature data from a 7 × 7 voxel-fitting region for parameter estimation. Simulations were repeated 400 times at each noise level and box plots include the median value (midline), upper and lower quartiles (box boundaries), with whiskers extending to the most extreme values or 1.5 times the IQR. Plus signs indicate outliers.

Table 1. Errors of estimated SAR amplitude and FWHM, and thermal diffusivity for different voxel-fitting regions. Simulations repeated 400 times with a noise standard deviation of 2 °C. Errors are presented as the median percent error of the 400 simulations and the breadth of the IQR.

Size of voxel-fitting region	Maximum SAR median% error (IQR)	SAR FWHM median% error (IQR)	Thermal diffusivity median% error (IQR)
3 × 3	7.6 (35.4)	−6.3 (40.2)	5.4 (88.7)
5 × 5	8.2 (21.8)	−7.0 (9.4)	4.6 (23.3)
7 × 7	7.2 (18.9)	−7.2 (6.7)	3.0 (15.8)
9 × 9	7.5 (18.2)	−7.3 (6.1)	2.4 (13.1)
11 × 11	8.3 (17.6)	−6.9 (6.3)	6.0 (11.2)

the number of temperature-versus-time curves for fitting reduces the IQR of estimates for maximum SAR, SAR FWHM, and thermal diffusivity.

3.3. Parameter estimation: MR temporal sampling simulations

While not shown, variation in errors caused by simulated temporal sampling were less than 5% for temperatures and all parameter estimates. In temperature measurements at the location of maximum heating, errors were less than ± 1%. Errors in maximum SAR estimation ranged from 6.6% error for $t_{acq} = 1$ s to 11.3% error for $t_{acq} = 8$ s. Errors in FWHM estimation ranged from −8.5% to −9.4% for the same acquisition times. Diffusivity was overestimated consistently, ranging from 1.7% overestimation for $t_{acq} = 1$ s to 5.8% for $t_{acq} = 8$ s.

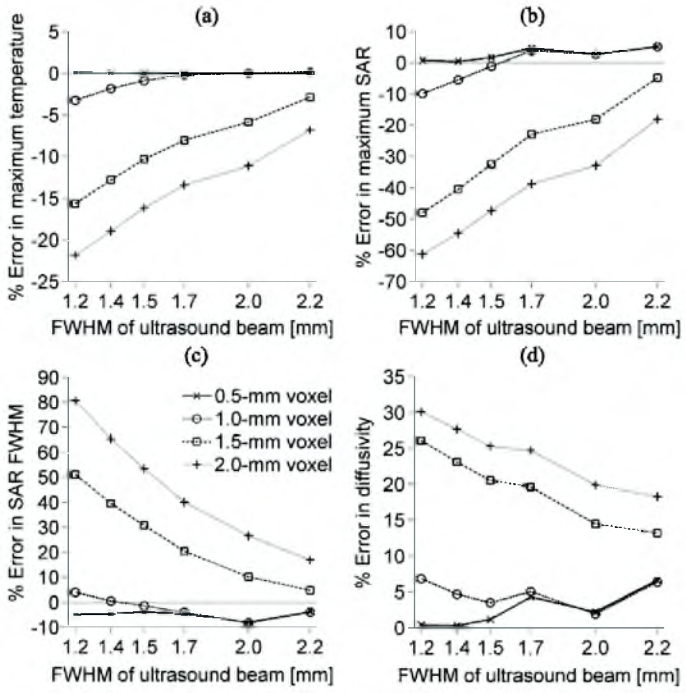

Figure 6. Simulated spatial averaging errors for varied isotropic voxel spacings and ultrasound focal zone sizes. (a) shows errors in spatially averaged temperatures at the location of maximum heating, while parameter estimation errors caused by spatial averaging are shown in (b) for maximum SAR, (c) for estimated beam FWHM, and (d) for thermal diffusivity.

3.4. Parameter estimation: MR spatial averaging simulations

Simulated MR spatial averaging results for several HIFU focal zone sizes with lateral FWHM measurements ranging from 1.2 to 2.2 mm are presented in figure 6. Figure 6(a) shows that spatial averaging causes temperature measurements to be lower than the unaveraged values. Plots are only shown are for the location of maximum heating, where errors are the largest, though temperatures are underestimated throughout the focal zone. Using those inaccurate temperature measurements in parameter estimation generally leads to underestimation of maximum SAR (figure 6(b)) and overestimation of the SAR FWHM (figure 6(c)) and tissue thermal diffusivity (figure 6(d)). For the HIFU focal zone sizes studied, an isotropic voxel spacing no larger than 1.0 mm is required to measure the maximum temperature rise with less than 5% error. Using 1.0 mm isotropic voxel spacing also keeps all parameter estimation errors less than $\pm 10\%$ for beams with a lateral FWHM less than 2.2 mm.

3.5. Parameter estimation: non-isotropic spatial averaging simulations

Though these simulation results are not shown, for the reference focal zone size (lateral FWHM = 1.4 mm, axial FWHM = 7.9 mm) with a transverse voxel dimension of $1 \times 1\ \text{mm}^2$, the axial voxel dimension can be increased from isotropy up to 3 mm without affecting the accuracy of temperatures and estimates of SAR amplitude and FWHM, and thermal diffusivity. The axial voxel dimension can be increased up to 4.3 mm with errors in temperature, FWHM and diffusivity estimates still less than $\pm 10\%$, and errors in SAR amplitude less than 20%. At 5 mm for the axial voxel dimension, errors in temperature deviate from the isotropic case

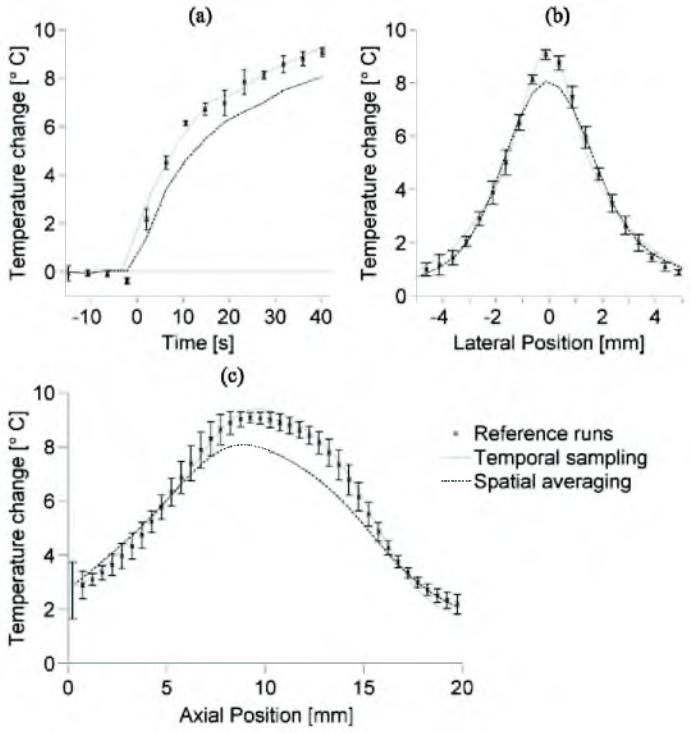

Figure 7. Experimental temperatures for reference runs ($1 \times 1 \times 3$ mm^3 spatial resolution, $t_{acq} = 4.2$ s), temporal sampling data ($1 \times 1 \times 3$ mm^3 spatial resolution, $t_{acq} = 6.3$ s), and spatial averaging data ($2 \times 2 \times 3$ mm^3 spatial resolution, $t_{acq} = 4.2$ s) in *ex vivo* pork loin. (a) is a temperature-versus-time curve at the location of maximum heating, while (b) and (c) are respectively lateral and axial temperature profiles from the last measurements of the ultrasound heating. Error bars ($N = 4$) extend to ± 1 standard deviation of the reference temperature data. Lateral positions are measured from the beam axis and axial positions are measured from the imaging plane nearest the transducer.

by more than 10% and subsequent errors in parameter estimation can be affected by as much as 25%.

3.6. Experimental temperature results

Figure 7 compares the temperature rise results from the reference experimental runs ($1 \times 1 \times 3$ mm^3, $t_{acq} = 4.2$ s) with altered temporal sampling ($1 \times 1 \times 3$ mm^3, $t_{acq} = 6.3$ s) and spatial averaging ($2 \times 2 \times 3$ mm^3, $t_{acq} = 4.2$ s) cases. Error bars on reference temperatures extend to plus or minus one standard deviation. Figure 7(a) is a temperature-versus-time plot at the location of maximum heating within the focal zone. The maximum temperature rise measured in the focal zone for the reference runs ($N = 4$) had a mean of 9.15 °C with a standard deviation of 0.18 °C. For the temporal sampling and spatial averaging cases, the maximum measured temperature rises were 9.42 °C and 8.07 °C, respectively. Those maximum temperatures occurred in the final measurements acquired during heating, at 40.2 s for the reference and spatial averaging cases and at 41.2 s for the temporal sampling case. Figures 7(b) and (c) show the lateral and axial temperature profiles through the focal zone at those times. Noise levels in temperature measurements for the reference, temporal sampling,

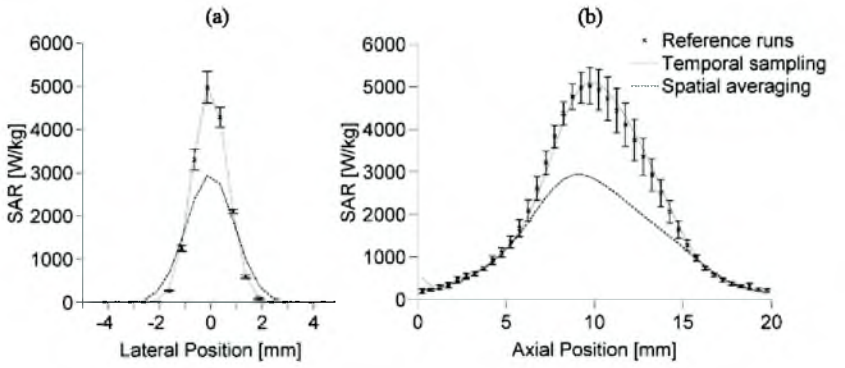

Figure 8. Experimentally estimated SAR profiles in *ex vivo* pork loin from reference, temporal sampling, and spatial averaging data in the (a) lateral and (b) axial directions. Error bars extend to ± 1 standard deviation from the mean of reference runs. Lateral positions are measured from the beam axis and axial positions are measured from the imaging plane nearest the transducer.

Table 2. Experimental parameter estimation results in *ex vivo* pork loin. Reference values are presented as the mean and standard deviation of estimates from the four reference runs.

	Maximum SAR (W kg^{-1})	SAR FWHM (mm)	Thermal diffusivity (m^2 s^{-1})
Reference mean (SD)	5023 (428)	1.56 (0.04)	1.44×10^{-7} (0.10×10^{-7})
Temporal sampling	5117	1.58	1.53×10^{-7}
Spatial averaging	3148	2.21	1.79×10^{-7}

and spatial averaging cases had a standard deviation of 0.26 ± 0.01 °C, 0.23 °C, and 0.10 °C, respectively.

3.7. Parameter estimation: experimental SAR, FWHM, and thermal diffusivity

The estimated lateral and axial SAR profiles through the focal zone for the different cases are shown in figures 8(a) and (b), respectively. Error bars mark one standard deviation above and below the mean value for the reference runs. Table 2 summarizes the experimental parameter estimation results showing the maximum SAR, SAR FWHM, and thermal diffusivity values obtained by fitting equation (2) to the temperature data. Published values for pork loin thermal diffusivity range from 1.17×10^{-7} to 1.66×10^{-7} m^2 s^{-1} (Kent *et al* 1984, Sanz *et al* 1987).

4. Discussion

The primary finding of this study is that the accuracy of parameter estimates using the analytical method of Dillon *et al* 2012 is strongly dependent upon the accuracy of MRTI temperature measurements, which are influenced primarily by the degree of spatial averaging. Errors in temperature measurements caused by the MRTI acquisition process are not only propagated, but are exacerbated when those temperatures are utilized for SAR and diffusivity estimation. Temporal sampling of temperature data caused by MRTI had little effect on temperatures or parameter estimation. Estimation errors caused by noise in temperature measurements, while unavoidable, can be reduced by fitting with a voxel region that covers the entire focal zone.

4.1. MRTI noise

The simulation results of figure 5 show that utilizing temperature-versus-time data from a 7 × 7 voxel-fitting region, when compared with a 3 × 3 voxel-fitting region, significantly reduces both the incidence and magnitude of parameter estimation errors caused by noise. These results are even clearer from table 1; the more than fivefold increase in data of the 7 × 7 region compared to the 3 × 3 region reduced the IQR of maximum SAR, FWHM, and thermal diffusivity estimation error by 47%, 83%, and 82%, respectively.

While increasing the number of voxels for parameter estimation reduces errors, it also creates an increased computational burden during the fitting process. For example, parameter estimation for 40 slices of experimental temperature data using a 3 × 3 voxel-fitting region per slice took 26 s to compute in MATLAB on an Intel Core 2 Duo Processor T6500 at 2.1 GHz with 4.00 GB of RAM, while estimation for the same slices using data from a 7 × 7 voxel-fitting region took 144 s. In addition, voxels added to the fitting process are increasingly distant from the beam axis, their temperature changes are smaller, and noise makes up a larger portion of the overall temperature signal. In brief, there exist diminishing returns from increasing the number of fitting voxels in efforts to decrease noise-induced errors. Finding the appropriate balance between error reduction, computation time, and temperature signal-to-noise ratio becomes an important aspect in determining the number of voxels used in fitting for SAR amplitude and FWHM, and thermal diffusivity estimation. A good rule of thumb may be to only include voxel locations that are between the first zeros of the lateral SAR profile.

Increasing the time used to reach a certain temperature for parameter estimation could also mitigate the effects of noise. While Dillon *et al* 2012 showed that increasing the number of data points from each temperature-versus-time curve in the absence of noise did not significantly change the accuracy of SAR estimation, that is not the case for noisy temperature data. Just as increasing the number of voxels for fitting improves parameter estimation, increasing the number of data points in each temperature-versus-time curve introduces additional useful data to the fitting process, helping to reduce noise-induced errors in SAR amplitude, SAR FWHM, and diffusivity estimation. In this sense a longer heating time at a lower power during pretreatment sessions would allow more data points for fitting, reduce noise-induced errors, and provide more accurate estimations of the beam FWHM and tissue thermal diffusivity. Based on the results of Dillon *et al* 2012, the SAR could be scaled directly from these low-power pretreatment pulses to the higher powers to be used in the ablative treatment. It should be noted that accurately scaling SAR in this manner is limited to the linear acoustic propagation regime. At higher powers that could induce cavitation, nonlinear effects can lead to enhanced heating, significantly changing the SAR distribution in addition to generating sharp temperature spikes which are difficult to measure with MRTI (Khokhlova *et al* 2009).

4.2. MR temporal sampling

The effects of temporal sampling upon MRTI temperatures appear to be minimal based on both simulation and experimental results. From simulated temperature and parameter estimations (section 3.3), there is a small decrease in accuracy with increasing acquisition time (<5% change). Because no ground truth temperature measurements are available for the experimental results and the actual parameter values are unknown, only trends in the experimental results can be commented upon. Comparing the reference experimental runs ($t_{acq} = 4.2$ s) with the temporal sampling run ($t_{acq} = 6.3$ s), there is no discernible change in the experimental temperature profile (figure 7) or parameter estimates (figure 8 and table 2), suggesting the minimal effect of temporal sampling.

It is known that the limiting factor in temporal sampling of MR temperature measurements is the rate of change of the temperature slope dT/dt. In this study, because the ultrasound is triggered to turn on and off in synchronization with the MRTI acquisition, the temperature slope does not vary enough within each measurement to greatly affect temperature measurements.

The standard progression through k-space for temporal sampling described in section 2.3 is not the same as the segmented EPI progression used in the experiments. In a segmented EPI sequence, k-space is divided uniformly into a number of segments determined by the EPI factor. One line of k-space in the phase encoding direction is acquired *in each EPI segment* for each pulse-sequence repetition time TR, effectively reducing the total MR acquisition time (t_{acq}) by the EPI factor. Because the EPI factor must be an odd number, data at the center of k-space, which is most significant, is always acquired at the midpoint in time of the image acquisition and progression through the central region of k-space does not include discontinuities that may occur at the transition between EPI segments. This matches the standard progression through k-space and additional simulations using the segmented EPI progression showed very little change in the temperature profiles ($< \pm 1\%$ difference) when compared with the standard k-space progression simulations.

One of the significant benefits of this estimation method is that the temporal resolution of temperature measurements plays such a limited role in the accuracy of parameter estimates. The traditional linear method for SAR estimation, on the other hand, has been shown to require temporal resolutions that are not currently feasible with three-dimensional MRTI (Dillon *et al* 2012). These results suggest that increasing the acquisition time per image to improve spatial resolution or minimize noise would be a useful approach for obtaining more accurate parameter estimates. However, a longer acquisition time would also generate fewer data points for fitting over the same heating period which may offset some of the gains from this approach. In other situations beyond parameter estimation, such as for thermal dose calculations, heating control and minimization of total treatment time, a short acquisition time is important so adjusting the temporal resolution should be used judiciously.

4.3. MR spatial averaging

Figure 6 shows that temperature errors caused by spatial averaging led to magnified errors in estimation of SAR amplitude and FWHM, and thermal diffusivity. A 15% error in the maximum temperature measurement could lead to SAR amplitude, SAR FWHM, and diffusivity errors of up to 50%, 50%, and 25% respectively. In order to obtain less than 5% error in temperatures and less than 10% error in parameter estimations using isotropic voxels, a 1 mm voxel dimension is necessary for the HIFU focal zone sizes (lateral FWHM = 1.2–2.2 mm) assessed in this study.

With current imaging methods, obtaining MR temperature measurements at 1 mm isotropic resolution introduces significant noise. Simulations for the reference focal zone size (lateral FWHM = 1.4 mm, axial FWHM = 7.9 mm) suggest that an axial voxel dimension of 3 mm with transverse plane voxel dimensions of 1×1 mm^2 will produce temperature measurements nearly identical to those obtained from 1 mm isotropic voxels. Parameter estimation of SAR amplitude and FWHM, and thermal diffusivity are also unaffected by using $1 \times 1 \times 3$ mm^3 voxels in place of $1 \times 1 \times 1$ mm^3 voxels. The stronger MR signal present from using these larger voxels should significantly reduce noise errors without introducing spatial averaging errors.

Trends in the experimental results support simulation results and highlight the importance of the degree of spatial averaging in MR-guided HIFU treatments. Peak experimental temperature measurements in the focal zone decreased by 12% when voxel spacing was

increased from $1 \times 1 \times 3$ to $2 \times 2 \times 3$ mm^3. Simulation results suggested those temperature measurements would decrease 10–17% (figure 6(a)). Experimental estimates of thermal diffusivity from temperature data obtained with $2 \times 2 \times 3$ mm^3 voxel spacing do not fall within the range of published data on pork loin thermal diffusivity (Kent *et al* 1984, Sanz *et al* 1987). The spatially averaged diffusivity estimates were 24% higher than the mean of reference estimates (table 2). This overestimation coincides with predicted simulation errors (figure 6(d)). Estimation differences between spatially averaged and reference data for SAR amplitude (−37%) and FWHM (42%) also correspond to anticipated errors from simulation data (figures 6(b), (c)).

4.4. General observations

While this estimation method is intended to be used primarily in pretreatment planning, other applications are worth noting. Estimated SAR values could be used in the validation of ultrasound prediction techniques that include scattering, which is often neglected in current modeling practice. During therapeutic sessions, this method could be applied quickly for verification of pretreatment modeling and tissue property values if the pre-sonication temperature distribution is relatively uniform. The temperature fitting process could also be applied to forward-predict temperature and thermal dose profiles for improved control and monitoring.

The power deposition patterns used in this study are specific to the HIFU phased-array system used in simulations and experiments. However, many other HIFU systems have similar power deposition patterns and conclusions of this study may likely be applied without introducing significant errors. In particular, the different focal zone sizes assessed for spatial averaging effects demonstrate that the conclusions based on our reference focal zone size (lateral FWHM = 1.4 mm, axial FWHM = 7.9 mm) should be applicable to different systems and power deposition patterns. Inclusion of larger voxel-fitting regions to reduce noise effects would apply to any HIFU system. As discussed previously, temporal sampling is primarily a function of the rate of change of the temperature slope dT/dt, and would not be greatly affected by the application system.

The applicability of this estimation method is limited to the focal region. However, in the implementation of MRgHIFU for thermal therapies, temperatures and thermal dose in the near and far fields provide important safety constraints and should be considered in pretreatment planning strategies. One possibility for obtaining near and far field SAR would be to implement this method for determination of the focal SAR profile and use it as a guide for optimizing ultrasound modeling software that includes near and far field heating. Alternatively, since the SAR distribution in the near and far field are generally more diffuse and uniform than in the focal region, the traditional linear method for finding SAR (Guy *et al* 1974, Roemer *et al* 1985) from experimental temperature data could be implemented in those regions.

There are additional potential MRTI acquisition errors that were not assessed in this study. However, effects of those errors can be inferred. A systematic bias in the reference temperature (for example, if the baseline temperature was 33 °C instead of an assumed 37 °C) would not affect these results since SAR, FWHM, and thermal diffusivity estimates are based upon changes in temperature and not the absolute magnitude of temperature as is the case in thermal dose calculations. An error in the scale of the phase to temperature conversion would cause proportional errors in SAR estimates but would not affect FWHM or thermal diffusivity estimation. Temperature errors caused by phase drift during the scan are mitigated by using reference-less reconstruction techniques (Rieke *et al* 2004). Measurement discrepancies caused by grid placement that puts the maximum power deposition at edges or corners of a voxel

were not assessed. However, zero-filling to 0.5 × 0.5 mm^2 in-plane will sufficiently mitigate most measurement discrepancy (Todd *et al* 2011).

5. Conclusion

This study demonstrates that estimates of HIFU SAR amplitude and FWHM, and thermal diffusivity are highly dependent upon the accuracy of MRTI temperature measurements. Specifically, errors in temperature measurements due to spatial averaging may lead to significant errors in parameter estimation. From simulated and experimental MRTI results, it is recommended that for HIFU beams with a lateral FWHM between 1.2 and 2.2 mm, a spatial resolution of 1 × 1 × 3 mm^3 or smaller is required to accurately measure focal temperatures and estimate the maximum SAR, SAR FWHM, and tissue thermal diffusivity. Temporal sampling results show that for the temporal resolutions studied, longer acquisition times may be used to improve spatial resolution or image SNR without adversely affecting temperature measurements or parameter estimation accuracy. Effects of noise in temperature measurements, while unavoidable, can be reduced by simultaneous fitting of more voxels in the transverse plane and including more data points from each temperature-versus-time curve.

The MRTI sampling standards identified in this study will lead to accurate estimates of SAR amplitude and FWHM, as well as tissue thermal diffusivity. Such tissue- and patient-specific results will improve the efficacy and accuracy of treatment planning, reduce treatment times, and increase clinical acceptance of and confidence in HIFU thermal therapies.

Acknowledgments

The authors would like to thank Josh de Bever for his contributions to this work and gratefully acknowledge support from Siemens Healthcare AG, the FUS Foundation, the Ben and Iris Margolis Foundation, and NIH grants R01 CA87785, R01 EB013433, and R01 CA134599.

References

Anand A and Kaczkowski P J 2008 Noninvasive measurement of local thermal diffusivity using backscattered ultrasound and focused ultrasound heating *Ultrasound Med. Biol.* **34** 1449–64

Anand A and Kaczkowski P J 2009 Noninvasive determination of in situ heating rate using kHz acoustic emissions and focused ultrasound *Ultrasound Med. Biol.* **35** 1662–71

Bobkova S, Gavrilov L, Khokhlova V, Shaw A and Hand J 2010 Focusing of high-intensity ultrasound through the rib cage using a therapeutic random phased array *Ultrasound Med. Biol.* **36** 888–906

Cheng H L and Plewes D B 2002 Tissue thermal conductivity by magnetic resonance thermometry and focused ultrasound heating *J. Magn. Reson. Imaging* **16** 598–609

De Poorter J D, De Wagter C, De Deene Y, Thomsen C, Stahlberg F and Achten E 1995 Noninvasive MRI thermometry with the proton resonance frequency (PRF) method: *in vivo* results in human muscle *Magn. Reson. Med.* **33** 74–81

Dillon C R, Vyas U, Payne A, Christensen D A and Roemer R B 2012 An analytical solution for improved HIFU SAR estimation *Phys. Med. Biol.* **57** 4527–44

Dragonu I, de Oliveira P L, Laurent C, Mougenot C, Grenier N, Moonen C T W and Quesson B 2009 Non-invasive determination of tissue thermal parameters from high intensity focused ultrasound treatment monitored by volumetric MRI thermometry *NMR Biomed.* **22** 843–51

Giridhar D, Robinson R A, Liu Y, Sliwa J, Zderic V and Myers M R 2012 Quantitative estimation of ultrasound beam intensities using infrared thermometry-Experimental validation *J. Acoust. Soc. Am.* **131** 4283–91

Goss S A, Cobb J W and Frizzell L A 1977 Effect of beam width and thermocouple size on the measurement of ultrasonic absorption using the thermoelectric technique *IEEE Ultrason. Symp.* pp 206–11

Guy A W, Lehmann J F and Stonebridge J B 1974 Therapeutic applications of electromagnetic power *Proc. IEEE* **62** 55–75

Ishihara Y, Calderon A, Watanabe H, Okamoto K, Suzuki Y, Kuroda K and Suzuki Y 1995 A precise and fast temperature mapping using water proton chemical shift *Magn. Reson. Med.* **33** 814–23

Kent M, Christiansen K, Van Haneghem I A, Holtz E, Morley M J, Nesvadba P and Poulsen K P 1984 COST 90 collaborative measurements of thermal properties of foods *J. Food Eng.* **3** 117–50

Kharalkar N M, Hayes L J and Valvano J W 2008 Power-pulse integrated-decay technique for the measurement of thermal conductivity *Meas. Sci. Technol.* **19** 075104

Khokhlova T D, Canney M S, Lee D, Marro K I, Crum L A, Khokhlova V A and Bailey M R 2009 Magnetic resonance imaging of boiling induced by high intensity focused ultrasound *J. Acoust. Soc. Am.* **125** 2420–31

Kress R and Roemer R 1987 A comparative analysis of thermal blood perfusion measurement techniques *J. Biomech. Eng.* **109** 218–25

Mahoney K, Fjield T, McDannold N, Clement G and Hynynen K 2001 Comparison of modelled and observed *in vivo* temperature elevations induced by focused ultrasound: implications for treatment planning *Phys. Med. Biol.* **46** 1785–98

Milner T E, Goodman D M, Tanenbaum B S, Anvari B and Nelson J S 1996 Noncontact determination of thermal diffusivity in biomaterials using infrared radiometry *J. Biomed. Opt.* **1** 92–7

O'Neill B E, Karmonik C, Sassaroli E and Li K C 2012 Estimation of thermal dose from MR thermometry during application of nonablative pulsed high intensity focused ultrasound *J. Magn. Reson. Imaging* **35** 1169–78

Parker K J 1983 The thermal pulse decay technique for measuring ultrasonic absorption coefficients *J. Acoust. Soc. Am.* **74** 1356–61

Parker K J 1985 Effects of heat conduction and sample size on ultrasonic absorption measurements *J. Acoust. Soc. Am.* **77** 719–25

Payne A, Vyas U, Todd N, de Bever J, Christensen D A and Parker D L 2011 The effect of electronically steering a phased array ultrasound transducer on near-field tissue heating *Med. Phys.* **38** 4971–81

Pennes H H 1948 Analysis of tissue and arterial blood temperatures in the resting human forearm *J. Appl. Physiol.* **1** 93–122

Rieke V, Vigen K K, Sommer G, Daniel B L, Pauly J M and Butts K 2004 Referenceless PRF shift thermometry *Magn. Reson. Med.* **51** 1223–31

Roemer R B 1999 Engineering aspects of hyperthermia therapy *Annu. Rev. Biomed. Eng.* **1** 347–76

Roemer R B, Fletcher A M and Cetas T C 1985 Obtaining local SAR and blood perfusion data from temperature measurements: steady state and transient techniques compared *Int. J. Radiat. Oncol. Biol. Phys.* **11** 1539–50

Sanz P D, Alonso M D and Mascheroni R H 1987 Thermophysical properties of meat products: general bibliography and experimental values *Trans. ASAE* **30** 283–9

Telenkov S A, Youn J, Goodman D M, Welch A J and Milner T E 2001 Non-contact measurement of thermal diffusivity in tissue *Phys. Med. Biol.* **46** 551–8

Todd N, Vyas U, de Bever J, Payne A and Parker D L 2011 The effects of spatial sampling choices on MR temperature measurements *Magn. Reson. Med.* **65** 515–21

Valvano J W, Allen J T and Bowman H F 1984 The simultaneous measurement of thermal conductivity, thermal diffusivity, and perfusion in small volumes of tissue *J. Biomech. Eng.* **106** 192–7

Vyas U and Christensen D A 2012 Ultrasound beam simulations in inhomogeneous tissue geometries using the hybrid angular spectrum method *IEEE Trans. Ultrason. Ferroelectr. Freq. Control* **59** 1093–1100

CHAPTER 4

THE ACCURACY AND PRECISION OF TWO NONINVASIVE, MAGNETIC RESONANCE-GUIDED FOCUSED ULTRASOUND-BASED THERMAL DIFFUSIVITY ESTIMATION METHODS

In review for publication in the

International Journal of Hyperthermia.

CR Dillon, [1] A Payne,[2,3] DA Christensen,[1,4] and RB Roemer[1,2,3]

1. Department of Bioengineering, University of Utah, Salt Lake City, Utah.
2. Department of Radiology, University of Utah, Salt Lake City, Utah.
3. Department of Mechanical Engineering, University of Utah, Salt Lake City, Utah.
4. Department of Electrical and Computer Engineering, University of Utah, Salt Lake City, Utah.

4.1 Abstract

The use of correct tissue thermal diffusivity values is necessary for making accurate thermal modeling predictions during magnetic resonance-guided focused ultrasound (MRgFUS) treatment planning. This study evaluates the accuracy and precision of two noninvasive thermal diffusivity estimation methods, a Gaussian temperature method published by Cheng and Plewes in 2002 and a Gaussian specific absorption rate (SAR) method published by Dillon et al. in 2012.

Both methods utilize MRgFUS temperature data obtained during cooling following a short (<25s) heating pulse. The Gaussian SAR method can also use temperatures obtained during heating. Experiments were performed at non-ablative levels (ΔT~10°C) in *ex vivo* pork muscle and *in vivo* rabbit back muscle. Thermal diffusivity estimates were also compared with measurements from two standard invasive methods.

Both noninvasive methods accurately estimate thermal diffusivity using cooling MR-temperature data (overall *ex vivo* error < 6%, *in vivo* < 12%). Including heating data in the Gaussian SAR method further reduces errors (*ex vivo* error < 2%, *in vivo* < 3%). Lower standard deviation values indicate that the Gaussian SAR method has better precision than the Gaussian temperature method.

With repeated sonications, either MR-based method could provide accurate thermal diffusivity values for MRgFUS therapies. Because of decreased sensitivity to noise and by utilizing both heating and cooling data, the Gaussian SAR method potentially requires fewer sonications to accurately establish thermal diffusivity.

4.2 Introduction

Because of large spatial temperature gradients near the focal zone during focused ultrasound (FUS) sonications, conduction plays a significant role in the temporal progression of FUS treatments and their ultimate outcomes. The significant parameter that accounts for conduction is the tissue thermal diffusivity. Accurate thermal diffusivity values can result in efficient pretreatment thermal modeling and treatment planning, fewer impromptu adjustments during treatments, increased efficacy and safety of treatments, and ultimately greater clinical acceptance of FUS as a thermal therapy.

Tissue thermal diffusivity can vary significantly among individuals and tissue types. As an example, the Foundation for Research on Information Technologies in Society (IT'IS) tissue property database, which includes tissue property data from many different studies in the literature, provides thermal diffusivity values of human kidney ranging from 0.114 to 0.150 mm^2/s [1]. In a simulated FUS heating pulse, this variability in thermal diffusivity leads to a 22% variation in the peak temperature after only 30 s of heating. Applied to real treatments, such errors would severely limit the value of pretreatment planning. Hence, identifying patient- and tissue-specific thermal diffusivity is essential if treatment planning is to provide its full potential contribution to treatment safety and efficacy.

A common approach to obtaining local estimates of the thermal diffusivity is to fit experimental temperature data to an analytical temperature solution that includes the thermal diffusivity as a fitting parameter. Traditionally, researchers have used invasive thermistor or thermocouple probes [2-7] for thermal property estimation. More recently

developed noninvasive techniques are not only more acceptable for clinical applications, but also provide more extensive temperature data for fitting [8-11].

In a noninvasive MR-based approach, Cheng and Plewes [12] developed a method which uses magnetic resonance-guided focused ultrasound (MRgFUS) temperature data to find the tissue thermal diffusivity. That method assumes that a Gaussian temperature distribution is present at the end of heating and that a Gaussian temperature distribution is retained during cooling. They applied their technique to several *ex vivo* tissues and *in vivo* rabbit thigh muscle, reporting precision errors of less than 10%. Subsequent studies have applied their method in *ex vivo* perfused porcine kidney (precision of 10% [13]), *in vivo* porcine kidney (precision of 40-50% [14]), and *in vivo* porcine thigh muscle (precision of 10% [15]). In those studies, the maximum focal temperature and noise in temperature measurements varied significantly, limiting the value of directly comparing precision values.

More recently, a different method using MRgFUS temperature data was proposed by Dillon et al. [16] and has been applied in tissue mimicking phantoms [16] and *ex vivo* pork muscle [17]. That method assumes a Gaussian SAR heating pattern applied to the tissue, and uses temperature data acquired during the heating, but not the cooling, period. The only available precision data for that method is from one *ex vivo* pork muscle sample (4 sonications at a single location), where the standard deviation of thermal diffusivity estimates was 7% of the mean value [17].

Interestingly, none of the studies above using MRgFUS have established the accuracy of their methods by comparing their results directly with concomitant measurements in

the same tissue samples from more established invasive methods, instead relying upon comparison with data reported in the literature.

The purpose of this study is to assess the accuracy and precision of the two MRgFUS thermal diffusivity estimation techniques developed by Cheng and Plewes [12] and Dillon et al. [16] at heating levels that do not cause tissue damage. The Cheng and Plewes method, hereafter termed the Gaussian temperature method, uses data exclusively from the cooling portion of the temperature curve. The Dillon method, hereafter called the Gaussian SAR method, has been extended to include cooling data and will be applied in two ways: 1) using only the cooling data for direct comparisons with the Gaussian temperature method, and 2) using both heating and cooling temperature data. Results will be compared with two established invasive estimation techniques in *ex vivo* pork muscle samples and *in vivo* rabbit back muscle to quantify the accuracy and precision of these noninvasive methods using clinically relevant heating and MR parameters.

4.3 Materials and methods

4.3.1 Theory: Noninvasive MR temperature-based methods

The derivation of the analytical solutions for the two noninvasive MR temperature-based methods can be found in the original papers [12,16]. For reference, the theoretical approximations applied to each noninvasive method are summarized in Table 4.1.

4.3.1.1 Gaussian temperature method. Cheng and Plewes demonstrated that the transverse plane's (Figure 4.1) analytical temperature distribution following an impulse heat source with an elliptical (axial and radial) Gaussian heating pattern is given by:

Table 4.1: Comparison of approximations of two noninvasive MRgFUS thermal diffusivity estimation methods.

Parameter	Gaussian temperature	Gaussian SAR
FUS power deposition pattern	Transverse: radial Gaussian Axial: Gaussian	Transverse: radial Gaussian Axial: uniform
Heating	Instantaneous	Short duration
Pennes' perfusion	Constant, homogeneous	Negligible
Tissue properties	Homogeneous	Homogeneous

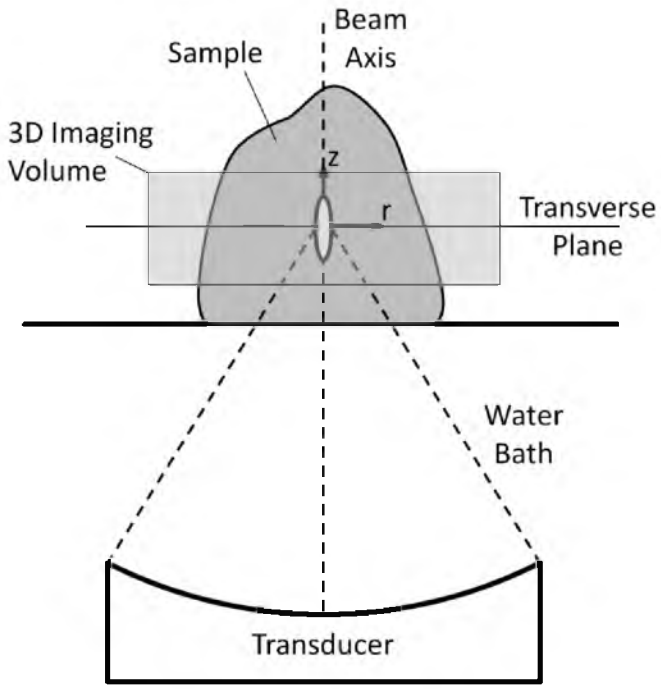

Figure 4.1. Setup for MRgFUS experiments and orientation of coordinate axes in analytical solutions used for thermal diffusivity estimation.

$$T_{Cool}(r, z = 0, t) = A \cdot exp\left[\frac{-r^2}{4\alpha t + \beta}\right], \quad (4.1)$$

where r is the radial distance (mm) from the axis of beam propagation, z=0 is the axial position (mm) at the center of the focal zone, t is the time (s) after the instantaneous heating pulse, A is the time- and perfusion-dependent temperature (°C) at the center of the focal zone, α is the local tissue thermal diffusivity (mm^2/s), and β is the transverse Gaussian variance of the focused ultrasound beam (mm^2).

The basic approximation in this method is that the temperature distribution at the beginning of cooling is Gaussian, as would be achieved by instantaneous heating with a Gaussian power deposition pattern. Estimating the thermal diffusivity with this approximation can be performed in a two-part process. First, Equation 4.1 is fit to the experimental temperatures to determine parameter $4\alpha t+\beta$, the temperature distribution's Gaussian variance, at each time point during the cooling period. The first derivative of this parameter with respect to time is directly proportional to the thermal diffusivity. Thus, plotting parameter $4\alpha t+\beta$ versus time and applying a linear fit provides the rate of increase of the Gaussian temperature variance, from which estimates of the tissue thermal diffusivity are made.

4.3.1.2 Gaussian SAR method. Dillon et al. used the analytical solution for a radial Gaussian heating pattern (uniform in the axial direction) to estimate thermal diffusivity for situations where blood perfusion effects are negligible. The transverse plane's analytical solution during heating was shown to be:

$$T_{Heat}(r, t) = C\left(\frac{\beta}{4\alpha}\right)\left[Ei\left(\frac{-r^2}{\beta}\right) - Ei\left(\frac{-r^2}{4\alpha t + \beta}\right)\right], \quad (4.2)$$

where Ei is the exponential integral function [18], t is the time (s) since the onset of ultrasound heating, and C is the initial rate of temperature increase (°C/s) at the center of the focal zone. Like the Gaussian temperature method, this solution assumes a Gaussian SAR heating pattern, but it does not require that the temperature distribution remain Gaussian, making it more applicable when longer sonication times are used.

Because thermal diffusivity also plays a significant role during tissue cooling, it should be useful to utilize both the heating and cooling curves for diffusivity estimation. This requires an analytical expression for the temperature profile after the ultrasound is turned off, which was not provided in the original Dillon et al. [16] derivation. Applying the principle of superposition, the desired cooling solution is given by:

$$T_{Cool}(r, t > t_h) = C\left(\frac{\beta}{4\alpha}\right)\left[-Ei\left(\frac{-r^2}{4\alpha t + \beta}\right) + Ei\left(\frac{-r^2}{4\alpha(t - t_h) + \beta}\right)\right], \qquad (4.3)$$

where t_h is the ultrasound heating time (s). A single three parameter fit (fitting parameters: C, α, and β) to the transverse experimental temperature data during heating (Equation 4.2) and cooling (Equation 4.3) provides an estimate of the local tissue thermal diffusivity α (mm^2/s).

4.3.2 Theory: Invasive reference methods

To obtain reference data for assessing the accuracy of the noninvasive MR temperature-based estimation methods, two commonly used invasive methods were applied to measure the tissue thermal diffusivity. These methods are applicable when perfusion effects are negligible.

4.3.2.1 Transient line-source method. The transient line-source method makes use of a long thin constant-power heating probe. The probe is invasively inserted in the sample

and the power source is turned on while a thermocouple at known radial distance, r, from the heating probe takes temperature measurements.

The theory behind the transient line-source method uses the analytical solution for an infinite line source with constant power per unit length. This analytical temperature solution during heating is given by [19]:

$$T_{Heat}(r,t) = -\frac{Q}{4\pi k} Ei\left(\frac{-r^2}{4\alpha t}\right), \tag{4.4}$$

where Q is the power per unit length (W/m) of the probe, k is the tissue thermal conductivity (W/m/°C), and Ei is the exponential integral function. After heating for a given time t_h, the analytical solution during cooling is:

$$T_{Cool}(r, t > t_h) = \frac{Q}{4\pi k}\left[-Ei\left(\frac{-r^2}{4\alpha t}\right) + Ei\left(\frac{-r^2}{4\alpha(t-t_h)}\right)\right]. \tag{4.5}$$

By applying a known power Q, measuring the temperature at a known distance r, and fitting the measured heating and cooling data to Equation 4.4 and Equation 4.5, respectively, the two fitting parameters of thermal conductivity k and thermal diffusivity α can be determined.

The similar analytic form of the cooling solutions for the transient line-source method (Equation 4.5) and the Gaussian SAR method (Equation 4.3) is noteworthy. In approximations and derivations, the only significant difference between these methods is found in the energy source term; for the transient line-source method, the source in the transverse plane is a single point and for the Gaussian SAR method, the source is a radial Gaussian. This difference manifests itself in the equations by the presence of the Gaussian variance of the ultrasound beam β in Equation 4.3 and its absence in Equation 4.5. When the methods are applied, the source term is known for the transient line-source

method and for the Gaussian SAR method, its distribution is determined via fitting parameters C and β.

4.3.2.2 Combined-property method. Thermal diffusivity is defined by the ratio of the thermal conductivity k to the density ρ and specific heat capacity c_t of the tissue ($\alpha=k/\rho c_t$). As discussed above, the transient line-source method provides estimates for the tissue thermal conductivity. Tissue density can be calculated by measuring the mass of a tissue sample and dividing by its volume, as determined by the volume of water it displaces when submerged. A digital scanning calorimeter can be used to measure the specific heat capacity from a small tissue sample. Using the combination of these invasive property measurements, a second independent measurement of the tissue thermal diffusivity can be made.

4.3.3 MRgFUS experimental setup

Ex vivo experiments were performed in four pork muscle samples purchased at a local Whole Foods Market 2 to 6 hours prior to the experiment and allowed to thermally equilibrate at room temperature in air-tight packaging. Heating was performed using an MR-compatible 256-element FUS phased-array system (Image Guided Therapy, Bordeaux, France) and no electronic steering was utilized in *ex vivo* experiments. The geometric focus was positioned 3.4 to 4.7 cm into the sample (N=8 total heating locations, n=30 total sonications). Heating times varied from 3.6 to 21.8 s with the power varied (7-18 acoustic watts) to obtain a temperature rise of approximately 10 °C by the end of heating. A delay of at least 7 minutes was provided between sonications to ensure that the tissue cooled to a uniform temperature before subsequent heating.

In vivo experiments were performed in the back muscles of two female New Zealand white rabbits (4.1, 4.5 kg). The rabbits were initially anesthetized with ketamine (40 mg/kg, IM) and xylazine (5 mg/kg, IM). Hair in the beam path was removed with clippers and depilatory cream to improve acoustic coupling. Animals were then intubated and mechanically ventilated with isofluorane (1-3%) to maintain anesthesia. Each rabbit was positioned supine on the MRgFUS system and sonications were repeated in two locations of the back muscle separated by 1.0-1.5 cm (N=4 total heating locations, n=25 total sonications), each with a focal depth of 2.0 cm. Transducer power was 8 acoustic watts and heating time ranged from 21.7-23.6 s with a minimum delay of 7 minutes between individual sonications. Heart rate, end tidal CO_2, percent oxygen saturation, and rectal temperature were monitored continuously during the experiment. Following FUS sonications, the animals were euthanized, the back muscle was exposed, and invasive thermal diffusivity measurements were made. The protocol was approved by the Institutional Animal Care and Use Committee.

MR temperature imaging (3T Siemens Trio MRI scanner) was performed during FUS experiments with the following parameters: three-dimensional segmented-EPI, TR=35-44 ms, TE=11 ms, FA=15-30°, bandwidth=738-744 Hz/pixel, Voxel size=1×1×3 mm^3, FOV=128-192×80-132 mm^2, 8 transverse slices (plus 25% oversampling), EPI factor=9, and temporal resolution=3.6-5.4 s. *Ex vivo* samples were positioned between a pair of two-channel surface coils built in-house and *in vivo* experiments used a single-loop coil positioned under the rabbit and a two-channel surface coil placed on the rabbit abdomen. Reconstruction of the MR data included weighting of the coils by the inverse covariance matrix [20] and zero-filled interpolation to 0.5-mm isotropic spatial resolution [17,21].

Temperatures measured with the proton resonance frequency method [22,23] were determined by a two-dimensional referenceless technique using a fifth-order polynomial [24]. A summary of the temperature data for these experiments along with selected ultrasound parameters is provided in Table 4.2. Noise in the temperature measurements was defined as the average of the standard deviation of the temperature measured over time for each voxel in an unheated region of the tissue.

Thermal dose values were calculated to demonstrate that this technique can be repetitively applied *in vivo* without causing extensive damage [25]. *Ex vivo* thermal dose values assumed an initial reference temperature of 37 °C, while *in vivo* calculations used the rectal temperature measured during the *in vivo* experiments, which ranged from 31 °C to 36 °C. The voxel with the highest cumulative thermal dose from a single heating sonication acquired 11 CEM43°C, which is below reported damage thresholds [25].

Table 4.2: Selected ultrasound parameters and temperature information from experimental data.

Experiment Type	Sample	Location	Total Sonications	Heating Time (s)	Power (acoustic watts)	Maximum Temperature Rise (°C)	Noise Standard Deviation (°C)
ex vivo	1	1	2	4.0	15	7.5-9.1	0.2
	2	1	4	3.6	18	6.7-6.9	0.3
		2	4	3.6	18	8.3-10.0	0.3
	3	1	4	20.0	10	8.1-9.0	0.2
		2	4	8.0	12	5.6-6.8	0.3
		3	4	12.0-20.0	12	7.4-10.0	0.3
	4	1	4	21.8	7	10.1-11.1	0.4
		2	4	21.8	7	8.1-9.8	0.5
in vivo	1	1	6	21.7	8	10.8-13.2	0.8-0.9
		2	6	21.7	8	12.3-14.5	1.1-1.5
	2	1	7	23.6	8	11.9-14.8	0.8-0.9
		2	6	23.6	8	13.5-14.5	0.7

4.3.4 Experiments: Noninvasive determination of thermal diffusivity

Estimations of tissue thermal diffusivity using the Gaussian temperature method employed a least-squares two-dimensional Gaussian fit (MATLAB function: *fminsearch*) of Equation 4.1 to the cooling MR temperature data in the slice of maximum temperature increase. The data presented herein utilized a spatial fitting region that included all voxels within a radius of r=6 mm from the beam axis. This region was selected because early results varying the size of the spatial fitting region identified a fitting radius of r≈5.5 mm, above which including additional data did not significantly affect diffusivity estimates.

Following the Cheng and Plewes criteria for inclusion [12], only Gaussian variances from cooling temperature images where the focal temperature SNR (defined as the ratio of the maximum focal temperature for a given acquisition time to the noise standard deviation) was greater than 5.0 were included in the Gaussian temperature method linear fits (MATLAB function: *polyfit*). For *in vivo* data, a focal temperature SNR>3.0 was required.

Thermal diffusivity estimates using the Gaussian SAR method employed the same circularly symmetric spatial fitting region with radius of 6 mm used in the Gaussian temperature method (the fitting radius for the Gaussian SAR method, above which estimates did not change, was r≈4 mm). Temporally, the single three-parameter fit (MATLAB function: *fminsearch*) of the Gaussian SAR method was applied in two different ways. First, for direct comparisons, the Gaussian SAR/cool only method included only the cooling data used in the Gaussian temperature method with the same SNR constraints (*ex vivo* focal temperature SNR>5.0, *in vivo* SNR>3.0). Second, the

Gaussian SAR/heat & cool method was applied using those cooling data in addition to the heating data.

4.3.5 Experiments: Invasive determination of thermal diffusivity

A commercially available device (KD2 Pro Thermal Properties Analyzer, Decagon Devices Inc., Pullman, WA, USA) was used for invasive transient line-source measurements of thermal diffusivity. The device has two 30-mm probes spaced 6 mm apart, with one probe being used for heating and the other for temperature measurements. The quoted accuracy of the device is ±10% for both thermal conductivity and thermal diffusivity in materials with a conductivity greater than 0.1 W/(m·°C).

For *ex vivo* samples, measurements were taken immediately before and after FUS experiments at a freshly cut sample surface to minimize effects of tissue dehydration and decomposition. These measurements were made at several locations throughout the pork muscle to assess the homogeneity of the tissue sample (n=7-8 per sample). Pre-experiment measurements were taken on the periphery of samples, since in one early experiment, air pockets from probe measurements near the FUS heating region introduced MR artifacts which confounded MR temperature-based thermal diffusivity estimates. No significant changes in thermal diffusivity or thermal conductivity were observed when comparing pre- and postexperiment measurements. For *in vivo* experiments, measurements were taken at several locations in the back muscle (n=4-5 per animal), including the region of FUS heating, immediately following euthanization of the animal. Measurements in the heated region did not vary significantly from other locations.

For *ex vivo* samples, density measurements were made with the displaced-water technique prior to experiments and repeated the day following experiments. Samples were stored overnight in an airtight plastic bag in a refrigerator. The sample was again cut in half and measurements taken at the freshly cut surface. No changes in density were observed before and after experiments.

Tissue specific heat capacity was measured using a digital scanning calorimeter (Q20, TA Instruments, New Castle, DE, USA). Tissue samples (30-50 mg) were hermetically sealed in aluminum pans to prevent water loss during the heating protocol, which included equilibration at 25 °C, a 1 minute isothermal period, ramped temperature increase at 10 °C/min to 65 °C, and another 1 minute isothermal period. The tissue specific heat capacity was determined as the average of values for which the prescribed heating rate (10 °C/min) was met. Variation in specific heat capacity over this temperature range was less than 4%. Also, no changes were observed when comparing pre- and postexperiment measurements of specific heat capacity. No visible lesions or tissue changes were observed in histology of the FUS heating region.

Combined-property diffusivity calculations used the mean of thermal conductivity values from the KD2 Pro divided by the mean of density and specific heat capacity measurements from pre- and postexperiment measurements. No combined-property diffusivity estimates were made in sample 3 of the *ex vivo* experiments because equipment for measuring specific heat capacity was unavailable at the time of the experiment. The combined-property method for measuring thermal diffusivity was not used for *in vivo* experiments.

4.4 Results

Both noninvasive thermal diffusivity estimation methods rely upon fitting to experimental temperature profiles. Some representative temperature data from *ex vivo* pork muscle are presented in Figure 4.2. Figure 4.2a plots the temperature versus time since the onset of ultrasound heating for two locations in the transverse plane. The first location is at the center of the focal zone and includes the maximum temperature change measured in the experiment (ΔT=11.1 °C) at 19.6 s of heating. The second location is in a nonheated region of the pork muscle, and its relatively constant baseline values (standard deviation=0.4 °C) illustrate the precision of the temperature measurements. Arrows in Figure 4.2a identify three times (t_1=24.0 s, t_2=32.7 s, t_3=45.7 s) during the cooling period for which transverse temperature data are plotted in Figure 4.2b. The results of the Gaussian temperature method's fits to those temperature data are also shown in Figure 4.2b. Figure 4.2c presents the time variation of parameter $4\alpha t+\beta$ as determined from the Gaussian fits of Figure 4.2b and other fits during cooling. The excellent linear fit (r^2=0.98) to those data is shown in Figure 4.2c, from which a Gaussian temperature method thermal diffusivity estimate of 0.128 mm^2/s was made. Figures 4.2d-f display results from the Gaussian SAR/heat & cool estimation method. Figure 4.2d replicates the temperature versus time curve at the center of the focal zone from Figure 4.2a and also includes the Gaussian SAR/heat & cool analytical fit for that position. Three times during the heating period (t_4=2.2 s, t_5=10.9 s, t_6=19.6 s) are identified for which transverse experimental temperature profiles are shown in Figure 4.2f. Figure 4.2e repeats the experimental temperature data from Figure 4.2b at times t_1, t_2, and t_3. Figures 4.2e and 4.2f also include the Gaussian SAR/heat & cool analytical

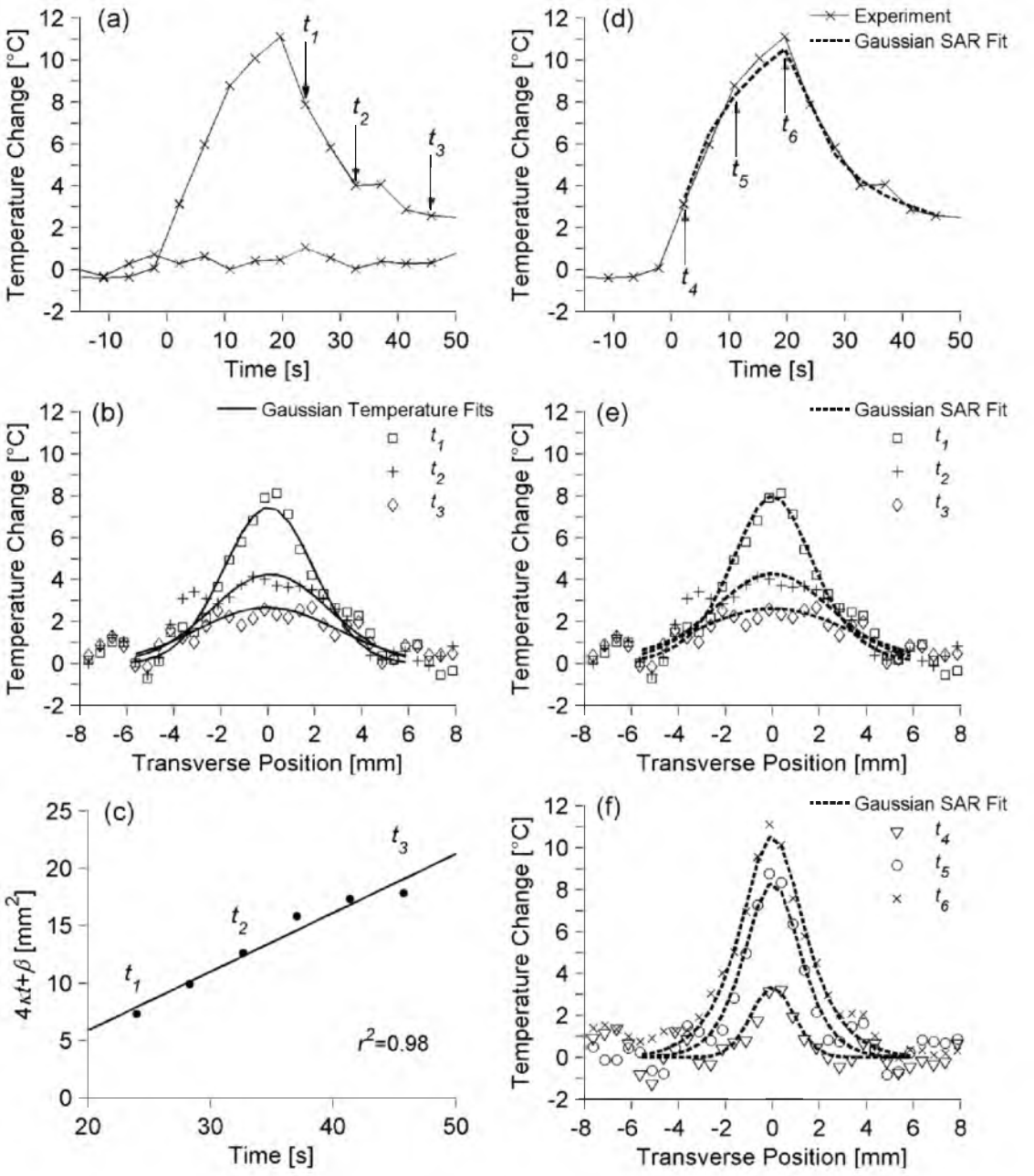

Figure 4.2: Representative *ex vivo* pork muscle temperatures and fits for thermal diffusivity estimation. (a) Temperature versus time profile at the center of the focal zone as well as baseline temperatures in a nonheated region 15 mm from the focus. Time is measured from the onset of heating. Arrows identify time points (t_1, t_2, t_3) whose transverse temperatures are plotted in (b) and compared with Gaussian temperature fits. (c) Estimates for $4\alpha t+\beta$ versus time and the linear fit of the Gaussian temperature method. (d) Temperature versus time profile at the center of the focal zone and corresponding data from the Gaussian SAR/heat & cool temperature fit. Transverse temperature profiles and the Gaussian SAR/heat & cool fit are plotted in (e) for cooling times t_1, t_2, and t_3 and in (f) for heating times t_4, t_5, t_6 (indicated by arrows in (d)).

temperature fit to experimental data at the specified time points. Differences between the Gaussian SAR/heat & cool fit presented in Figure 4.2e and the Gaussian SAR/cool only fit (not shown) are nominal with a maximum difference of 0.28 °C. The Gaussian SAR method produced thermal diffusivity estimates of 0.151 mm^2/s and 0.153 mm^2/s for the cool only and heat & cool data, respectively.

Figure 4.3 shows the *ex vivo* pork muscle results of the noninvasive MRgFUS estimation methods and both invasive methods. The far left column in Figure 4.3 shows the mean of all measurements made with each method, with error bars extending to plus and minus one standard deviation from the mean measurement. Using the transient line-source measurements for normalization, the standard deviation of all Gaussian temperature diffusivity measurements is 16% of the expected value. The standard deviation of the Gaussian SAR method is 10% for the cool only data and 7% for the heat & cool data. Using a one-tailed variance ratio test, each of these differences in standard deviation is significant with $p < 0.03$. The small standard deviation of the transient-line source method (2%) shows the homogeneity of pork muscle. The invasive combined property method exhibited the least variation of all methods, but results were limited to three measurements.

The quantitative results from *ex vivo* pork muscle experiments are presented in Table 4.3. Noninvasive MR-based thermal diffusivity estimates are presented as the mean of repeated sonications at a given location with standard deviation values in parentheses. Invasive transient line-source measurements are presented as the mean of measurements at several (n=7-8) locations with the standard deviation given in parentheses. When estimates and measurements from all samples and sonications are considered, the mean

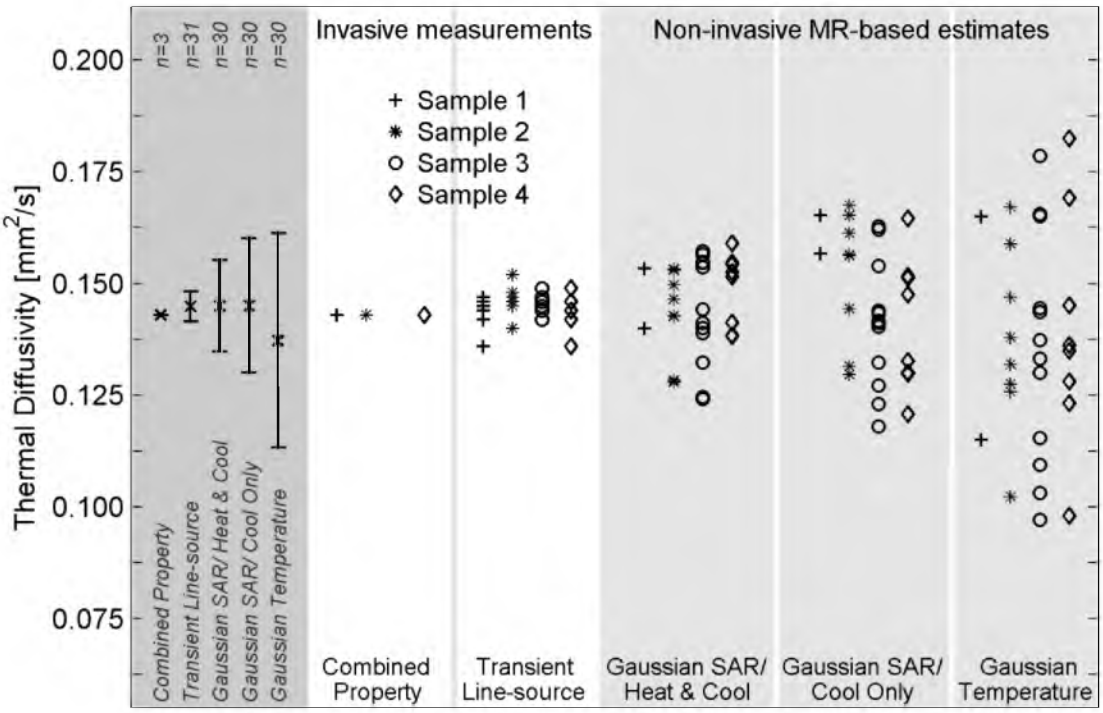

Figure 4.3. Thermal diffusivity measurements and estimates in four *ex vivo* pork muscle samples. Invasive measurements (white columns) serve as the reference standard for thermal diffusivity values. Noninvasive MR-temperature based estimates (light gray columns) were repeated multiple times in each sample. Results for the combination of all *ex vivo* pork muscle experiments are shown in the left column (dark gray) with error bars extending to ±1 standard deviation from the mean value.

Table 4.3. Summary of thermal diffusivity measurements and estimates in *ex vivo* pork muscle experiments. Results are presented as the mean value with standard deviation values in parentheses. Thermal diffusivity units are mm^2/s.

Sample	Location	Gaussian temperature	Gaussian SAR/ cool only	Gaussian SAR/ heat & cool	Transient line-source	Combined Property
1	1	0.140 (0.035)	0.161 (0.006)	0.147 (0.009)	0.145 (0.002)	0.143
2	1	0.146 (0.015)	0.140 (0.012)	0.137 (0.011)	0.146 (0.003)	0.143
	2	0.129 (0.023)	0.163 (0.005)	0.149 (0.005)		
3	1	0.150 (0.019)	0.150 (0.010)	0.149 (0.008)	0.146 (0.002)	NA
	2	0.131 (0.038)	0.138 (0.019)	0.140 (0.018)		
	3	0.125 (0.016)	0.135 (0.009)	0.142 (0.009)		
4	1	0.144 (0.018)	0.140 (0.011)	0.150 (0.008)	0.145 (0.004)	0.143
	2	0.135 (0.035)	0.142 (0.020)	0.148 (0.009)		
All	-	**0.137 (0.024)**	**0.145 (0.015)**	**0.145 (0.010)**	**0.145 (0.003)**	**0.143 (0.000)**

values are very consistent, ranging from 0.137 mm^2/s to 0.145 mm^2/s, and the noninvasive MR-temperature based estimation methods are accurate to within 6% of the standard invasive thermal diffusivity measurements.

Figure 4.4 is a coronal magnitude image from a representative *in vivo* rabbit experiment. The temperature change at the end of heating is overlaid in color, with a threshold value of 2 °C. The maximum temperature from this sonication was 13.2 °C and the standard deviation of the temperatures was 0.8 °C as determined from a nonheated region of the muscle.

The results of *in vivo* thermal diffusivity estimation and measurement in rabbit back muscle are presented in Figure 4.5. The overall mean of each method is shown in the left side column of Figure 4.5, with error bars extending to plus and minus one standard deviation from the mean. As with the *ex vivo* experiments, the normalized standard deviation of measurements was greatest in the Gaussian temperature method (83%), progressively smaller with the Gaussian SAR/cool only (23%) and Gaussian SAR/heat & cool methods (15%), and smallest with the invasive method (5%). Differences between these standard deviation values using a one-tailed variance ratio test were significant with $p < 0.03$.

Table 4.4 provides the mean and standard deviation of *in vivo* thermal diffusivity estimates and measurements displayed in Figure 4.5. The overall mean thermal diffusivity values for noninvasive estimation methods and invasive measurements matched well, varying from 0.135 mm^2/s to 0.153 mm^2/s, less than 12% error when using invasive measurements as the reference.

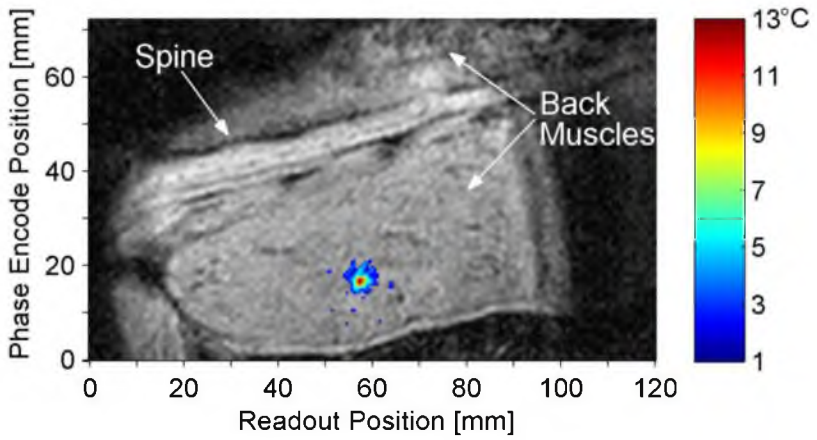

Figure 4.4. Magnitude image in coronal slice at time of maximum heating with temperature change overlay. The animal is supine, slightly oblique, with the head to the right of the image. The field of view is truncated to show only the region of interest, including the spine and back muscles. The threshold for temperature display is 2 °C.

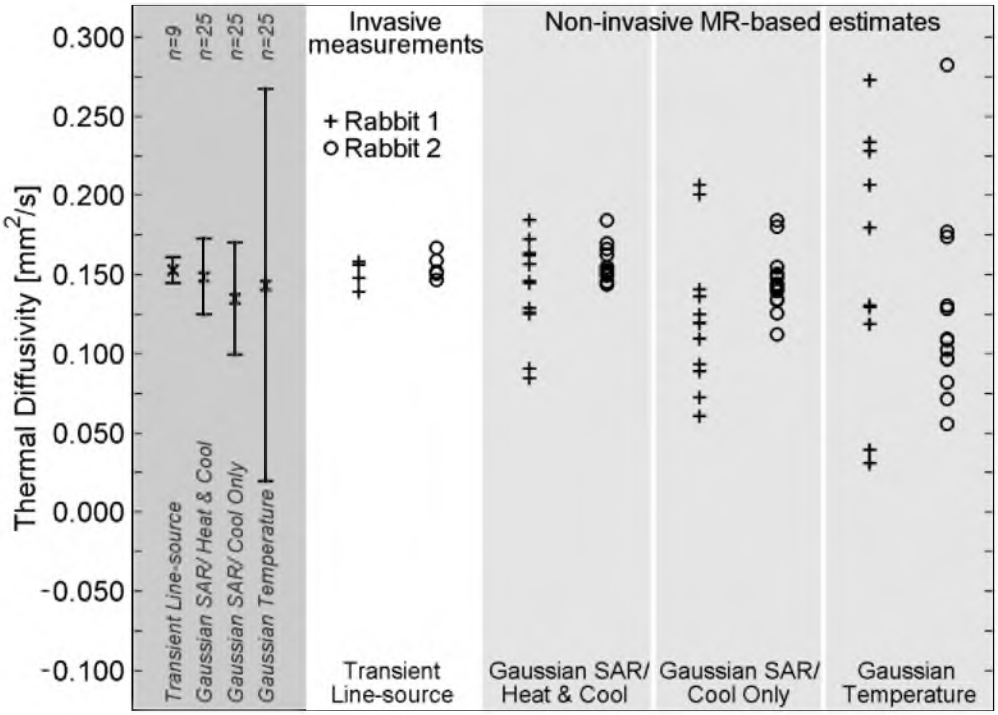

Figure 4.5. Thermal diffusivity measurements and estimates in *in vivo* rabbit back muscle. Invasive transient line-source measurements (white column) serve as the reference standard and were made at four to five locations in the back muscle. Noninvasive MR-based estimates were repeated six to seven times at two locations in each animal. Two estimates using the Gaussian temperature method in Rabbit 1 do not fit within the limits of the plot (α=-0.159, 0.554 mm^2/s). Results for the combination of all *in vivo* experiments are shown in the left column (dark gray) with error bars extending ±1 standard deviation from the mean value.

Table 4.4. *In vivo* results of thermal diffusivity measurement and estimation in rabbit back muscle experiments. Results are presented as the mean value with standard deviation values in parentheses. Thermal diffusivity units are in mm^2/s.

Rabbit	Location	Gaussian temperature	Gaussian SAR/ cool only	Gaussian SAR/ heat & cool	Transient line-source
1	1	0.136 (0.066)	0.129 (0.061)	0.132 (0.035)	0.150 (0.009)
	2	0.191 (0.239)	0.116 (0.024)	0.149 (0.026)	
2	1	0.147 (0.074)	0.148 (0.027)	0.161 (0.013)	0.155 (0.008)
	2	0.099 (0.020)	0.143 (0.006)	0.152 (0.008)	
All	-	**0.143 (0.124)**	**0.135 (0.035)**	**0.149 (0.024)**	**0.153 (0.008)**

4.5 Discussion

This study demonstrates that both the Gaussian temperature method and Gaussian SAR method can accurately and noninvasively estimate tissue thermal diffusivity in *ex vivo* and *in vivo* situations using nonablative MRgFUS temperature data. Because the precision of the Gaussian SAR method was better than the Gaussian temperature method, fewer estimates would be required with that method to confidently establish the tissue thermal diffusivity for use in pretreatment planning of MRgFUS thermal therapies.

4.5.1 Accuracy of MR-temperature based methods

This is the first study to the authors' knowledge which assesses the accuracy of either of these two MRgFUS-based thermal diffusivity estimation methods by comparison with standard invasive measurements. Comparing the mean values (× symbol) in the left columns of Figures 4.3 and 4.5, which are also found in the bottom rows of Tables 4.3 and 4.4, it is clear that the noninvasive estimation methods are consistent with the invasive standard methods for measuring thermal diffusivity. Using invasive

measurements as truth, the overall error for the noninvasive MR-based methods is less than 12% in both *ex vivo* (n=30) and *in vivo* (n=25) situations.

In practice, while an individual estimate from a single sonication may not accurately represent the tissue thermal diffusivity (see light gray columns of Figures 4.3 and 4.5), repeating sonications many times at each location would ensure confidence in the accuracy of the thermal diffusivity mean. Unfortunately, this approach is not clinically desirable for two reasons. First, it could make the pretreatment procedure long and expensive. Second, the cumulative effect of repeated heating could lead to unintended tissue damage. A better alternative is to improve the precision of these estimation techniques so that no more than one or two measurements are required to ensure an accurate tissue thermal diffusivity value.

4.5.2 Precision of MR-temperature based methods

Since precision represents the ability of a measurement to be consistently reproduced, the standard deviation of measurements repeated at the same location (or even different locations if the sample is homogeneous) serves as a measure of a method's precision. In this study, the standard deviation of all *ex vivo* pork muscle diffusivity estimates was 16% of the true diffusivity (determined by invasive measurements) for the Gaussian temperature method and 10% for the Gaussian SAR/cool only method. For *in vivo* results, the standard deviation of estimates was 83% and 23% for the Gaussian temperature and Gaussian SAR/cool only methods, respectively. Because these two methods make use of the same spatial and temporal data for fitting, these statistically significant differences in precision indicate that the Gaussian SAR/cool only method is

less sensitive to noise in the MR-temperature data than the Gaussian temperature method.

It is believed that this difference in noise sensitivity is due to the difference in how these two methods are implemented. While each of them uses the *fminsearch* algorithm, the Gaussian temperature method fits to spatial data multiple times, one fit for each time frame of the cooling period. Values for one parameter from those multiple fits are used as data for an additional linear fit to determine thermal diffusivity. The Gaussian SAR/cool only method uses exactly the same temperature data as the Gaussian temperature method, but applies a single fit to all of the spatial and temporal data. Because the method makes use of all the data at once, it should be less susceptible to errors introduced by noise.

The precision of the Gaussian SAR/cool only method is further improved by fitting the analytical temperature solution to heating data as well as cooling data, as was done in the Gaussian SAR/heat & cool method. The overall normalized standard deviation in *ex vivo* samples was reduced from 10% to 7% by including the heating data, and *in vivo* standard deviation values dropped from 23% to 15%. While it is expected that including additional temperature data improves the precision of estimates, the data included in the Gaussian SAR/heat & cool method are especially useful because the temperature SNR is greater during heating than for much of the cooling data, as can be seen in Figure 4.2. It could be argued that estimates made exclusively from heating data could be more precise because of the higher temperature SNR. However, early results of this study (not shown) demonstrated that while the temperature SNR of cooling data is lower, it still contains useful data and improves the precision of thermal diffusivity estimates. This was the initial motivation in utilizing Equation 4.3 in this study.

The significance of precision is that even when two methods are accurate, it will take fewer sonications to establish the thermal diffusivity of the tissue using a method with better precision. Currently, the precision of these noninvasive methods is limited by unavoidable MR noise, the desire to avoid ablative temperatures in pretreatment protocols (limiting the temperature SNR values obtainable), and the accuracy of MR temperature reconstruction methods [12,17,21]. With the continuing improvements being made to MR temperature imaging accuracy and precision, these noninvasive methods of estimating local tissue thermal diffusivity have the potential to become very useful in pretreatment planning of MRgFUS thermal therapies.

4.5.3 Significance of invasive method results

It should be emphasized that the standard deviation of noninvasive thermal diffusivity estimates and the standard deviation of invasive measurements with the transient line-source method are not directly comparable. Because only single measurements are made at several locations in the sample, standard deviation values for the invasive transient-line source method are a measure of the tissue sample homogeneity and do not address the precision of the measurement technique. Pork muscle was found to be very homogeneous, both within samples and across different samples, indicating that in future studies, a thermal diffusivity of 0.145 mm^2/s may be used as a reference standard. Rabbit back muscle was more variable. Because the tissue of interest in the rabbit was smaller and not excised, the invasive probes used to measure thermal diffusivity may have encountered different tissue types along their length, affecting thermal diffusivity measurements.

4.5.4 Study limitations

This study has sought to evaluate the accuracy and precision of two noninvasive MRgFUS thermal diffusivity estimation methods. The methods assume the tissue is homogeneous and further studies would be required to assess their applicability in heterogeneous tissues. Invasive measurements are also limited by this homogeneous approximation, and all of these methods, invasive and noninvasive, applied in heterogeneous tissues, measure a tissue average thermal diffusivity that would also be useful in patient treatment planning. These methods also assume the tissue thermal diffusivity is constant, which may not be a reasonable approximation for larger temperature ranges of interest in MRgFUS therapies, since property changes from water loss and protein denaturation at higher ablative temperatures can significantly alter thermal histories during heating [26].

Using an optimization routine that is more robust to outliers in the noise, such as an L1 objective function, may affect each of these thermal diffusivity estimation methods to different degrees and might affect the conclusions of this study. It is anticipated that implementing such a function would be beneficial to both of these methods and will be considered in future work.

The current study did not address how perfusion or blood flow from large vessels might affect the two noninvasive methods. Cheng and Plewes [12] demonstrated that as long as perfusion is constant and homogeneous, it does not affect the spatial distribution of temperatures and should not affect their estimation technique. Dillon et al. [16] showed in simulations that high perfusion (>10 $kg/m^3/s$) will significantly affect estimates of the FUS specific absorption rate. Such errors would also be seen in thermal

diffusivity values from that estimation method at high perfusion levels. In the current study, *in vivo* thermal diffusivity estimates using the Gaussian SAR/heat & cool method gave the same values as the invasive transient line-source method in the same tissue after the animals had been euthanized (<3% difference); therefore, perfusion values did not significantly affect the diffusivity estimates. These results were not surprising given that resting muscle perfusion is generally less than 1 $kg/m^3/s$ [1]. In tissues with higher perfusion, different analytical solutions or *ex vivo* studies for estimating thermal diffusivity may be necessary to obtain reliable results.

4.6 Conclusion

This study has shown that both of the noninvasive MRgFUS thermal diffusivity estimation methods can accurately quantify tissue thermal diffusivity if a sufficient number of heating sonications are applied. The Gaussian SAR method demonstrated better precision than the Gaussian temperature method because it is less sensitive to noise in MR-temperature data and the method can make use of heating data as well as cooling data. In the clinical setting, application of these methods for accurate determination of tissue thermal diffusivity will contribute to improved treatment safety and efficacy in MRgFUS treatment planning.

4.7 Acknowledgments

The authors would like to thank Dennis Parker, Nick Todd, and Josh de Bever for their contributions to this work. Financial support for this work was provided by Siemens Healthcare AG, the FUS Foundation, the Ben and Iris Margolis Foundation, and

NIH grants R01 EB013433 and R01 CA134599. The authors report no declarations of interest.

4.8 References

1. Hasgall PA, Neufeld E, Gosselin MC, Klingenböck A, Kuster N (2013) IT'IS database for thermal and electromagnetic parameters of biological tissues. Version 2.4. www.itis.ethz.ch/database

2. Chen MM, Holmes KR, Rupinskas V (1981) Pulse-decay method for measuring the thermal conductivity of living tissue. J Biomech Eng 103: 253-260.

3. Valvano JW, Allen JT, Bowman HF (1984) The simultaneous measurement of thermal conductivity, thermal diffusivity, and perfusion in small volumes of tissue. J Biomech Eng 106: 192-197.

4. Chato JC (1985) Measurement of thermal properties of biological materials. In: Shitzer A, Eberhard RC, editors. Heat transfer in medicine and biology. New York: Plenum. pp. 167-192.

5. Bowman HF (1985) Estimation of tissue blood flow. In: Shitzer A, Eberhard RC, editors. Heat transfer in medicine and biology. New York: Plenum. pp. 193-230.

6. Bhavaraju NC, Cao H, Yuan DY, Valvano JW (2001) Measurement of directional thermal properties of biomaterials. IEEE Trans Biomed Eng 48: 261-267.

7. Kharalkar NM, Hayes LJ, Valvano JW (2008) Power-pulse integrated-decay technique for the measurement of thermal conductivity. Meas Sci Technol 19 075104.

8. Milner TE, Goodman DM, Tanenbaum BS, Anvari B, Nelson JS (1996) Noncontact determination of thermal diffusivity in biomaterials using infrared radiometry. J Biomed Opt 1: 92-97.

9. Telenkov SA, Youn J, Goodman DM, Welch AJ, Milner TE (2001) Non-contact measurement of thermal diffusivity in tissue. Phys Med Biol 46: 551-558.

10. Kondyurin AV, Sviridov AP, Obrezkova MV, Lunin VV (2009) Noncontact measurement of thermal and optical parameters of biological tissues and materials using IR laser radiometry. Russian J Phys Chem A 83: 1405-1413.

11. Anand A, Kaczkowski PJ (2008) Noninvasive measurement of local thermal diffusivity using backscattered ultrasound and focused ultrasound heating. Ultrasound Med Biol 34: 1449-1464.

12. Cheng HL, Plewes DB (2002) Tissue thermal conductivity by magnetic resonance thermometry and focused ultrasound heating. J Magn Reson Imaging 16: 598-609.

13. Dragonu I, de Oliveira PL, Laurent C, Mougenot C, Grenier N, et al. (2009) Non-invasive determination of tissue thermal parameters from high intensity focused ultrasound treatment monitored by volumetric MRI thermometry. NMR Biomed 22: 843-851.

14. Cornelis F, Grenier N, Moonen CT, Quesson B. (2011) In vivo characterization of tissue thermal properties of the kidney during local hyperthermia induced by MR-guided high-intensity focused ultrasound. NMR Biomed 24:799-806.

15. Zhang J, Mougenot C, Partanen A, Muthupillai R, Hor PH (2013) Volumetric MRI-guided high-intensity focused ultrasound for noninvasive, in vivo determination of tissue thermal conductivity: initial experience in a pig model. J Magn Reson Imaging 37: 950-957.

16. Dillon CR, Vyas U, Payne A, Christensen DA, Roemer RB (2012) An analytical solution for improved HIFU SAR estimation. Phys Med Biol 57: 4527-4544.

17. Dillon CR, Todd N, Payne A, Parker DL, Christensen DA, et al. (2013). Effects of MRTI sampling characteristics on estimation of HIFU SAR and tissue thermal diffusivity. Phys Med Biol 58: 7291-7307.

18. Abramowitz M, Stegun IA (1964) Handbook of mathematical functions: with formulas, graphs, and mathematical tables. New York: Dover. 1046 p.

19. Carslaw HS, Jaeger JC (1959) Conduction of heat in solids. London: Oxford Univ Press. 510 p.

20. Roemer PB, Edelstein WA, Hayes CE, Souza SP, Mueller OM (1990) The NMR phased array. Magn Reson Med 16: 192-225.

21. Todd N, Vyas U, de Bever J, Payne A, Parker DL (2011) The effects of spatial sampling choices on MR temperature measurements. Magn Reson Med 65: 515-521.

22. De Poorter JD, De Wagter C, De Deene Y, Thomsen C, Stahlberg F, et al. (1995) Noninvasive MRI thermometry with the proton resonance frequency (PRF) method: in vivo results in human muscle. Magn Reson Med 33: 74-81.

23. Ishihara Y, Calderon A, Watanabe H, Okamoto K, Suzuki Y, et al. A precise and fast temperature mapping using water proton chemical shift. Magn Reson Med 33: 814-823.

24. Rieke V, Vigen KK, Sommer G, Daniel BL, Pauly JM, et al. (2004) Referenceless PRF shift thermometry. Magn Reson Med 51: 1223-1231.

25. Sapareto SA, Dewey WC (1984) Thermal dose determination in cancer therapy. Int J Radiat Oncol Biol Phys 10: 787-800.

26. Choi J, Morrissey M, Bischof JC (2013) Thermal processing of biological tissue at high temperatures: impact of protein denaturation and water loss on the thermal properties of human and porcine liver in the range 25–80° C. ASME J Heat Transfer 135: 061302.

CHAPTER 5

A FEASIBILITY STUDY FOR QUANTIFYING PERFUSION-RELATED ENERGY LOSSES USING MRgFUS

5.1 Introduction

In many studies, it has been demonstrated that perfusion plays a significant role in altering the temperature fields of FUS treatments [1-4]. Blood perfusion serves to draw energy away from the focal region, lowering temperatures and increasing the unpredictability of the treatment. In order to safely and completely ablate high perfusion regions, additional time is required for sonication, extending the overall treatment time. The concerns related to perfusion-related energy losses in MRgFUS are not limited to the increased treatment time alone. When more sonication time is required to induce tumor death, more dose will accumulate in the near field, potentially putting at risk healthy tissues [5]. For these reasons, accurate quantification of perfusion-related energy losses ($\dot{Q}_{bl}'''$ in Equation 1.11) for biothermal modeling of MRgFUS treatments is important.

The previous chapters have laid the foundation that makes a quantitative determination of $\dot{Q}_{bl}'''$ possible. When the SAR (Chapters 2-3), thermal diffusivity (Chapters 3-4), and temperature fields over time (MRTI) are known, a conservation of energy analysis will provide estimates of term $\dot{Q}_{bl}'''$ that may vary with time and position. This chapter introduces the theory, simulation verification, and initial experimental

results of two approaches for determining perfusion-related energy losses from MRgFUS data.

5.2 Theory

This section presents the heat transfer and numerical methods involved in two unique approaches for quantifying perfusion-related energy losses. For each of these approaches, only the cooling data following FUS heating are utilized so that SAR (and $\dot{Q}'''_{FUS}$) is equal to zero. The methods of Chapters 2-3 might have been used to obtain SAR during heating, but were not utilized for this feasibility study in order to eliminate a potential source of error.

5.2.1 Raw data approach

Immediately after the FUS heating has been turned off, the general bioheat transfer equation given by Equation 1.11 can be reduced and rearranged to the following equation, which governs the temperature distribution throughout the cooling period:

$$\dot{Q}'''_{bl} = k\nabla^2 T_{exp} - \rho c \frac{dT_{exp}}{dt}. \tag{5.1}$$

Subscript *exp* refers to experimental temperature data. Equation 5.1 can provide direct estimates of perfusion-related energy losses if each term on the right side of the equation is known. Properties k, ρ, and c can be calculated from the thermal diffusivity and the methods described in Chapter 4. The temperature terms in Equation 5.1 are determined from the experimental data. For the i,j,k-th voxel of MRTI temperature data (see Figure 5.1), the Laplacian of temperature can be discretized with a finite-difference (FD) approximation as

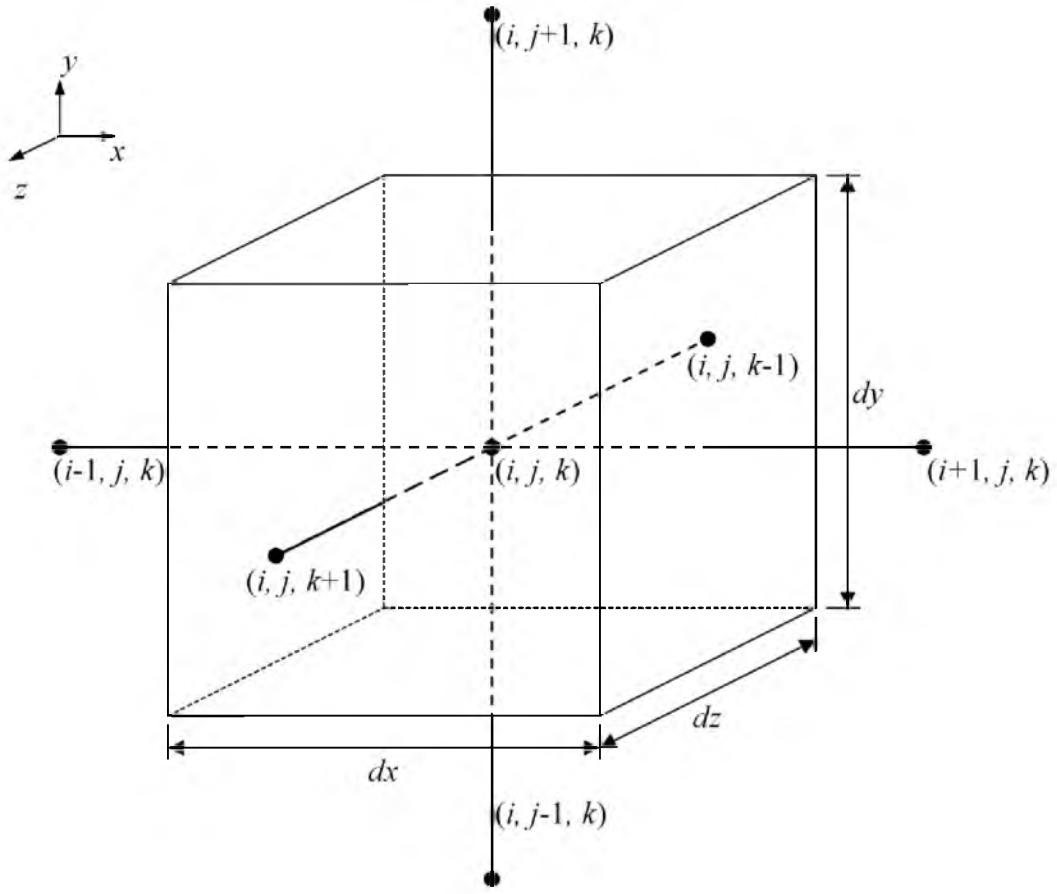

Figure 5.1: Finite-difference discretization for each MRTI voxel.

$$\nabla^2 T_{exp} = \frac{\left(T^p_{i-1,j,k} - 2T^p_{i,j,k} + T^p_{i+1,j,k}\right)}{dx^2} + \frac{\left(T^p_{i,j-1,k} - 2T^p_{i,j,k} + T^p_{i,j+1,k}\right)}{dy^2} + \frac{\left(T^p_{i,j,k-1} - 2T^p_{i,j,k} + T^p_{i,j,k+1}\right)}{dz^2}, \tag{5.2}$$

where *dx*, *dy*, and *dz* are the voxel dimensions in the *x*-, *y*-, and *z*-directions, respectively, and superscript *p* indicates the current time at which temperature is measured and the Laplacian is evaluated.

The derivative of temperature with respect to time found in Equation 5.1 is calculated from the experimental temperature data by means of a central difference approximation as

$$\frac{dT_{exp}}{dt} = \frac{\left(T_{i,j,k}^{p+1} - T_{i,j,k}^{p-1}\right)}{2t_{acq}}, \tag{5.3}$$

where t_{acq} is the acquisition time for each three-dimensional MR temperature image, and superscripts p-1 and p+1 indicate the temperatures measured immediately prior to and immediately following the current temperature measurement for the i,j,k-th voxel. The central difference approximation is used (instead of a forward difference approximation) so that the Laplacian and time derivative of temperature are evaluated consistently at time measurement p.

By substitution of Equations 5.2 and 5.3 into Equation 5.1 and with knowledge of tissue thermal properties, dynamic values for $\dot{Q}_{bl}'''$ can be calculated in each MRTI voxel directly from the experimental MR temperature data. Hereafter, this direct experimental data approach will be referred to as the raw data approach.

5.2.2 Model-based approach

A second approach for $\dot{Q}_{bl}'''$ quantification is possible by the incorporation of modeling in the estimation process. The model is used to determine what the temperature distribution would have been in the absence of perfusion. Experimental temperature data already includes the effects of perfusion-related energy losses. Thus, any difference between the experimental and modeled data is a result of perfusion-related energy losses.

This approach requires two consecutive three-dimensional MR temperature images acquired during the cooling period. Using the first MRTI temperature distribution as an initial condition, subsequent temperature decay is simulated via finite-difference methods according to

$$0 = k\nabla^2 T_{sim} - \rho c \frac{dT_{sim}}{dt}. \tag{5.4}$$

Note that Equation 5.4 for simulated data, hence subscript *sim*, takes the same form as Equation 5.1, with the important difference being that perfusion-related energy losses $\dot{Q}_{bl}'''$ have been excluded from the simulated model. By simulating temperatures for the MR acquisition time t_{acq}, the final model temperatures match up in time with the next available MR experimental temperature distribution.

Subtracting Equation 5.4 from Equation 5.1 yields a solution for perfusion-related energy losses that includes both simulated and experimental data:

$$\dot{Q}_{bl}''' = k\nabla^2 T_{exp} - k\nabla^2 T_{sim} + \rho c \left(\frac{dT_{sim}}{dt} - \frac{dT_{exp}}{dt}\right). \tag{5.5}$$

Assuming that perfusion does not affect the spatial distribution of temperatures [6], the first two terms on the right side of Equation 5.5 cancel each other. Then, using the difference in temperatures from the consecutive MRTI measurements (ΔT_{exp}), the corresponding difference in initial and final model temperatures (ΔT_{sim}), and the acquisition time t_{acq} to approximate time derivatives, Equation 5.5 becomes

$$\dot{Q}_{bl}''' = \rho c \left(\frac{\Delta T_{sim} - \Delta T_{exp}}{t_{acq}}\right). \tag{5.6}$$

The forward difference approximations of Equation 5.6 are used for this approach (instead of a central difference method) to minimize the time over which the approximations are made.

Equation 5.6 gives the three-dimensional distribution of $\dot{Q}_{bl}'''$ between two consecutive MR temperature images. By sequentially stepping through the cooling MRTI data, updating the initial condition and endpoint temperatures for each consecutive pair of

images, the dynamic three-dimensional distribution of perfusion-related energy losses can be evaluated. For the remaining sections of this chapter, this combined model and experimental data approach will be called the model-based approach.

5.2.3 Evaluating biothermal models

After determining the perfusion-related energy losses, $\dot{Q}_{bl}'''$ can be used in the evaluation of specific biothermal models. For this study, the Pennes bioheat transfer equation (PBHTE) [7], first introduced in Section 1.4.4 of the Introduction, with approximations of full tissue-blood equilibrium and constant arterial blood temperature, will be used. The equation of relevance (Equation 1.15) is repeated here for convenience:

$$\dot{Q}_{bl}''' = wc_{bl}(T - T_{ar}). \tag{5.7}$$

While the empirically derived Pennes perfusion parameter w is only equal to the true capillary blood perfusion in limited situations [8], comparison with actual capillary blood perfusion values can help identify appropriate magnitudes of w. For reference, fat and resting muscle perfusion are approximately 0.55 and 0.65 kg/m^3/s, respectively, brain perfusion is 9.3 kg/m^3/s, liver is 15 kg/m^3/s, and average values for kidney are 69 kg/m^3/s [9]. If large vessels traverse the MRgFUS heated region, even larger values for calculated local perfusion values could be possible.

5.3 Simulation verification

5.3.1 Simulation methods

A two-tissue model was utilized in simulations to verify the two approaches for quantifying perfusion-related energy losses with MRgFUS temperature data (see Figure

5.2). The two tissues have different acoustic, thermal, and perfusion properties, but all properties are assumed constant, uniform, and isotropic within each tissue type. Model tissue properties can be found in Table 5.1.

Two cases of perfusion were simulated. In Case 1, perfusion was set to zero for both tissues to verify that both approaches would accurately identify this limiting case. In Case 2, because it has been shown to be appropriate in some situations [10-15] and for reasons of simplicity, perfusion was modeled via the PBHTE (Equation 1.15) with values of 1.0 kg/m^3/s in Tissue 1 and 5.0 kg/m^3/s in Tissue 2. The blood specific heat capacity c_{bl} was assumed equal to the tissue specific heat capacity and T_{ar} was assumed uniform, constant, and equal to the uniform tissue temperature initial condition.

Heating was generated via a scanned FUS pattern with electronic steering to four focal locations in the transverse plane. Acoustic power was 30 acoustic watts and each focal location was steered ±2.0 mm in the x- and y- directions from the geometric focus on the tissue boundary (spacing = 4.0 mm, see Figure 5.2). The four individual SAR patterns were calculated via the hybrid angular spectrum method [16], superimposed, and scaled under the assumption that ultrasound applied continuously at one-fourth power is equivalent to rapid steering at a duty cycle of 0.25. The simulated heating lasted for 40 s and cooling temperatures were calculated for an additional 40 s. The isotropic FD grid spacing was 0.4 mm and the time step was 0.1 s. Finally, the FD temperatures were subsampled to a temporal resolution more representative of MRTI at 4.0 s.

The two approaches for quantifying perfusion-related energy losses (Sections 5.2.1 and 5.2.2) were applied to generate values of $\dot{Q}_{bl}'''$ from the FD temperature data. Then,

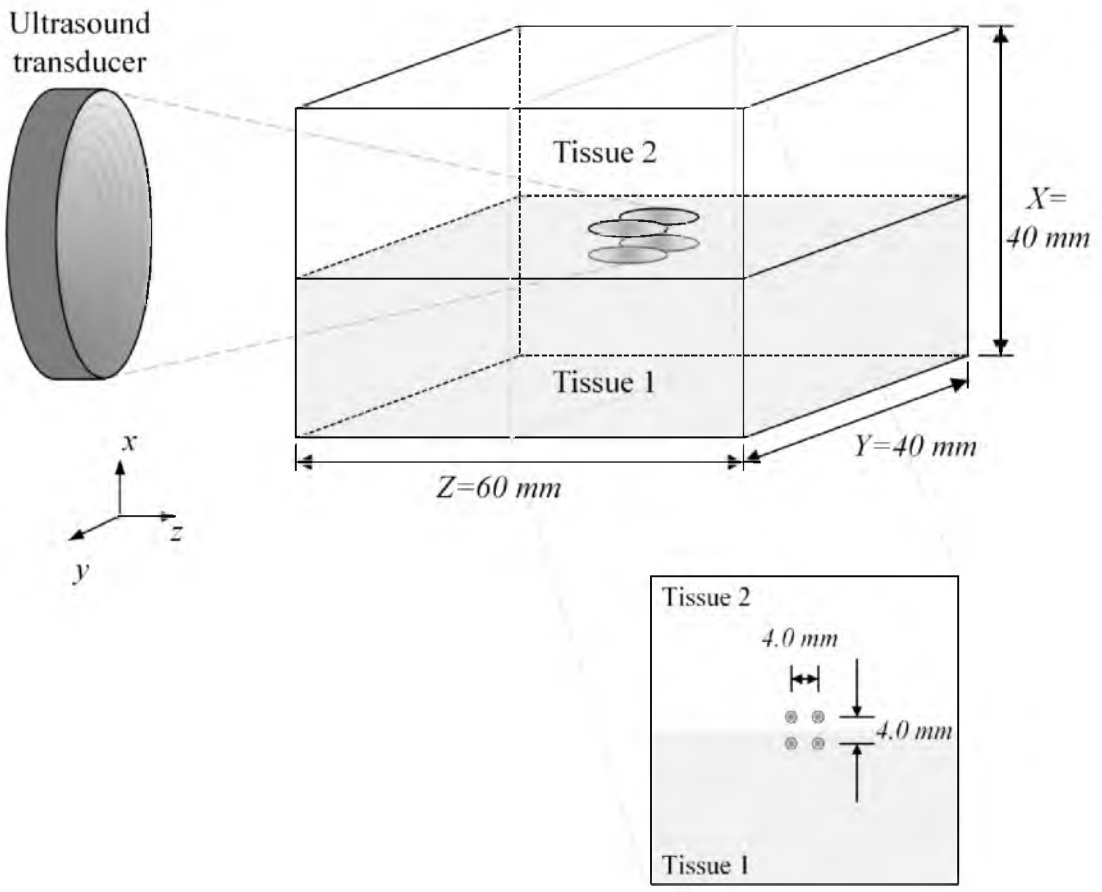

Figure 5.2: Schematic illustrating the two-tissue model used for simulations to verify approaches for quantifying perfusion-related energy losses. Inset at bottom identifies the four electronically steered focal positions in the transverse plane.

Table 5.1: Tissue properties for two-tissue model used in simulations to verify approaches for quantifying perfusion related energy losses.

	Units	Tissue 1	Tissue 2
Acoustic Properties			
Attenuation coefficient	Np/m	5.0	7.0
Density	kg/m^3	990	1050
Speed of Sound	m/s	1480	1500
Thermal Properties			
Thermal conductivity	W/m/°C	0.4	0.6
Specific heat capacity	J/kg/°C	3500	4180
Thermal diffusivity	mm^2/s	0.115	0.137
Perfusion			
Case 1	$kg/m^3/s$	0.0	0.0
Case 2	$kg/m^3/s$	1.0	5.0

those $\dot{Q}_{bl}'''$ estimates were used to calculate the Pennes perfusion parameter w for each location and time (Section 5.2.3).

5.3.2 Simulation results

For the limiting case of zero perfusion (Case 1) and at early cooling times (< 8 s), $\dot{Q}_{bl}'''$ and w estimates from the raw data approach do not match the true values and exhibit a pattern similar to the distribution of SAR (Figure 5.3a). This occurs because the central difference approximation used in time derivatives of the raw data approach (Equation 5.3) does not adequately represent the quickly changing temperatures early in the cooling period. After that time, when temperatures drop more gradually, absolute errors in w are less than 1.0 kg/m^3/s for all locations (Figure 5.3b and 5.3c) with estimates converging to zero (error < 0.1 kg/m^3/s) by 24 s. The model-based approach gives zero values for $\dot{Q}_{bl}'''$ and w for all times and locations, because for these simulations, the "experimental" and "modeled" data are identical (Figure 5.3). Maximum temperatures at the times corresponding to Figure 5.3a, 5.3b, and 5.3c are 18.2, 11.4, and 9.1 °C, respectively.

Figure 5.4 shows the results when perfusion in the two simulated tissues is nonzero (Case 2). Errors in the raw data approach are large early in cooling (Figure 5.4a), and both approaches converge toward the correct values later in cooling (Figure 5.4b and 5.4c). Maximum temperatures at the times corresponding to Figure 5.4a, 5.4b, and 5.4c are 17.9, 10.5, and 8.0 °C, respectively.

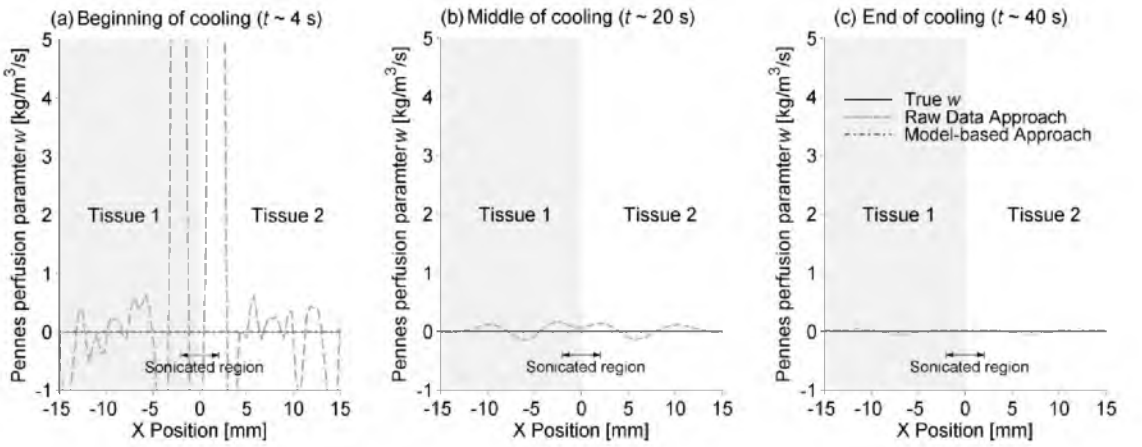

Figure 5.3: In simulated FUS heating of a two-tissue model with zero perfusion, both approaches for quantifying $\dot{Q}_{bl}'''$ and w converge toward the true Pennes perfusion parameter w after 40 s of cooling (Figure 5.4c). Early in the cooling period (Figure 5.3a), the raw data approach estimates w poorly, with a pattern similar to the SAR distribution. In the middle of cooling (Figure 5.4b), errors are less than 0.1 kg/m^3/s. The sonicated region is defined as the spacing of the electronically steered focal positions.

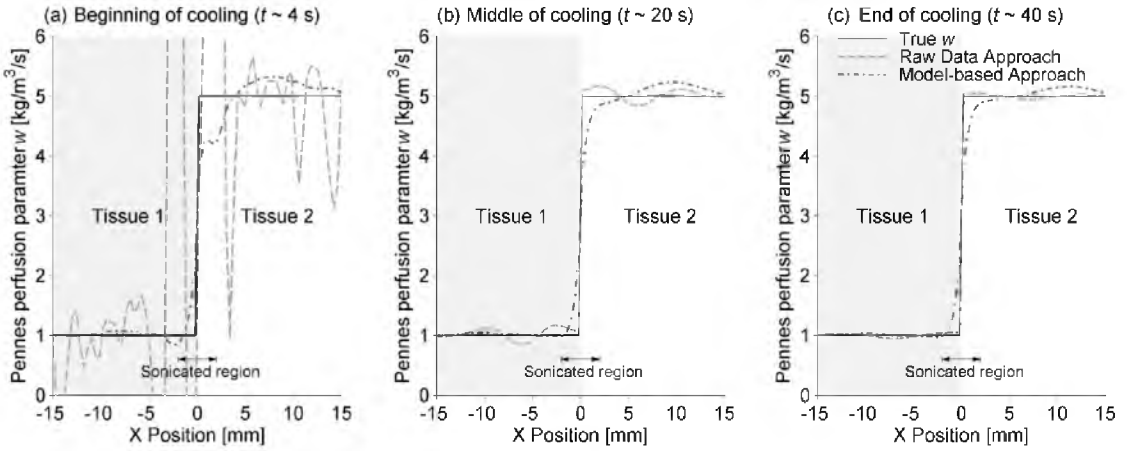

Figure 5.4: In simulated FUS heating of a two-tissue model with different perfusion values, both approaches for quantifying $\dot{Q}_{bl}'''$ and w converge toward the true Pennes perfusion parameter w after (b) 20 s and (c) 40 s of cooling. Early in cooling (a), the raw data approach does not accurately quantify the Pennes perfusion parameter w. The sonicated region is defined as the spacing of the electronically steered focal positions.

5.4 Initial experimental validation

5.4.1 Experimental methods

The initial validation experiment was performed in an *ex vivo* perfused porcine kidney with the setup shown in Figure 5.5. The kidney was obtained from a recently euthanized pig on a separate protocol. Just before euthanization, the animal was heavily heparinized, and following euthanization, kidney excision, and canulation of the renal artery, the kidney was flushed with a heparin and saline solution to prevent blood clotting in the vasculature [17]. Heating was achieved by electronically steering a phased-array ultrasound transducer (256 elements, f=1 MHz) [18] rapidly in an 8-mm radius circle for 150-160 s at 60-90 acoustic watts. The kidney was perfused with a heparin-H_2O solution in no-flow and two flow (20 and 40 mL/min) situations [19]. In order to obtain a higher and more consistent temperature distribution at the start of cooling, flow was initiated at the start of the cooling period. Three series of ultrasound heatings with each of the three flow situations were performed for a total of nine runs.

MR temperature data were acquired in 10 oblique axial slices with a 3T Siemens Trio MRI (three-dimensional segmented-EPI, TR/TE = 35/11 ms, FOV = 256x176x30 mm^3, FA = 20°, 752 Hz/pixel, EPI factor = 9, 2x2x3 mm^3, 4.2-s acquisition), reconstructed via the proton resonance frequency method [20-21] using a baseline reference technique, and zero filled interpolated to 0.5-mm isotropic spacing. Thermal properties were obtained via the methods described in Chapter 4.

Following temperature reconstruction, the two approaches for quantifying perfusion-related energy losses (Sections 5.2.1 and 5.2.2) were applied to generate values of $\dot{Q}_{bl}'''$ from the cooling temperature data. Values of $\dot{Q}_{bl}'''$ vary for each voxel and MR

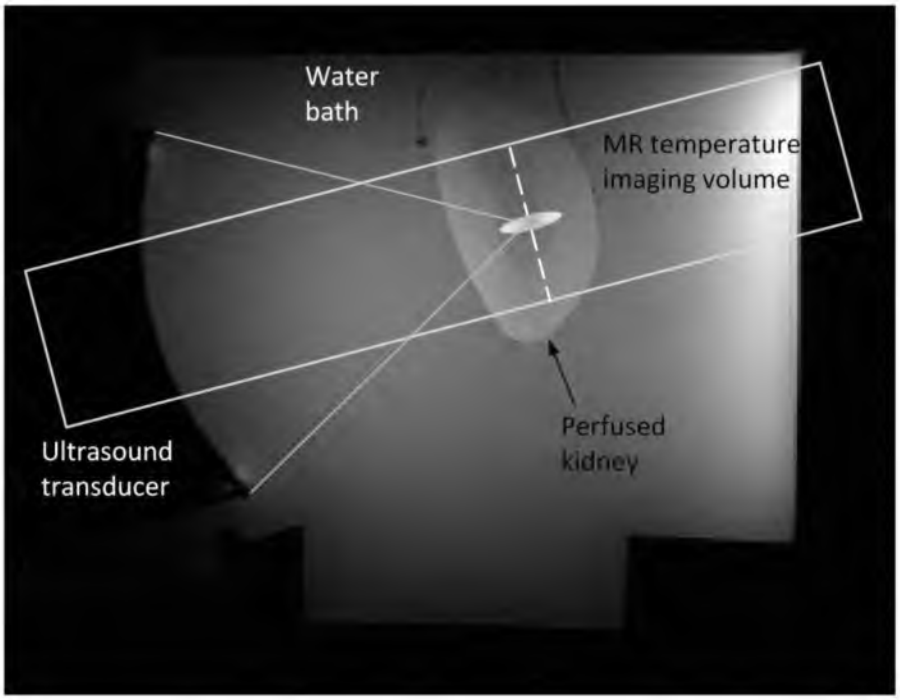

Figure 5.5: Experimental setup for MRgFUS heating of *ex vivo* perfused porcine kidney. The oblique axial MR temperature imaging volume and lines tracing the ultrasound beam profile have been overlaid on the sagittal MR magnitude image. The dashed line through the focal region indicates the spatial orientation of data presented in Figures 5.6-5.10.

acquisition in time; using those data to evaluate the Pennes perfusion parameter *w* (Section 5.2.3) may or may not include averaging in space or time to reduce noise effects. In one extreme, individual $\dot{Q}_{bl}'''$ values can be used to generate point-by-point, dynamic estimates of *w*. Alternatively, the collection of dynamic three-dimensional $\dot{Q}_{bl}'''$ values can be optimized for a single *w* value that is uniform in space and constant in time. Between these two extremes, the user may define discrete spatial regions and/or temporal periods for which local estimates of *w* can be optimized. When averaging is implemented in this chapter, *w* is optimized in Equation 5.7 from $\dot{Q}_{bl}'''$ and temperature data to minimize the least-squares error with MATLAB function *fminsearch*.

5.4.2 Experimental results

Experimental transverse temperature profiles ~4 s into the cooling period are shown in Figure 5.6a for one series (three sequential heating runs) at different flow rates. These temperature profiles in the phase encode direction correspond to the dashed line in Figure 5.5. Because the flow was not active during the heating period, these profiles are very similar. Later in the cooling period (~50 s), the temperature profiles diverge, with larger flow rates drawing energy away from the heated region and increasing the rate of temperature decay (Figure 5.6b).

Figure 5.7 shows the point-by-point results of the two approaches for $\dot{Q}_{bl}'''$ quantification corresponding to the temperature profiles and times of Figure 5.6. $\dot{Q}_{bl}'''$ values are larger at ~4 s into the cooling period (Figure 5.7a and 5.7c) than after ~50 s of cooling (Figure 5.7b and 5.7d). Variation in $\dot{Q}_{bl}'''$ is larger for the raw data approach (Figure 5.7a and 5.7b) than for the model-based approach (Figure 5.7c and 5.7d). While these results are generally noisy, trends show an increase in $\dot{Q}_{bl}'''$ with increasing flow rate.

For Figure 5.8, twelve $\dot{Q}_{bl}'''$ values in time (from the first 50 s of cooling) and the transient temperature data for each location were used in Equation 5.7 to optimize for a single constant *w* value on a point-by-point basis (MATLAB function *fminsearch*). For the no-flow cases, *w* values oscillate about zero with heated region minimum and maximum values of -13.5 and 14.9 kg/m^3/s for the raw data approach (Figure 5.8a) and -6.5 and 6.6 kg/m^3/s for the model-based approach (Figure 5.8b). As with $\dot{Q}_{bl}'''$, the magnitude of these constant, local *w* values generally increases with increasing flow rate for both approaches.

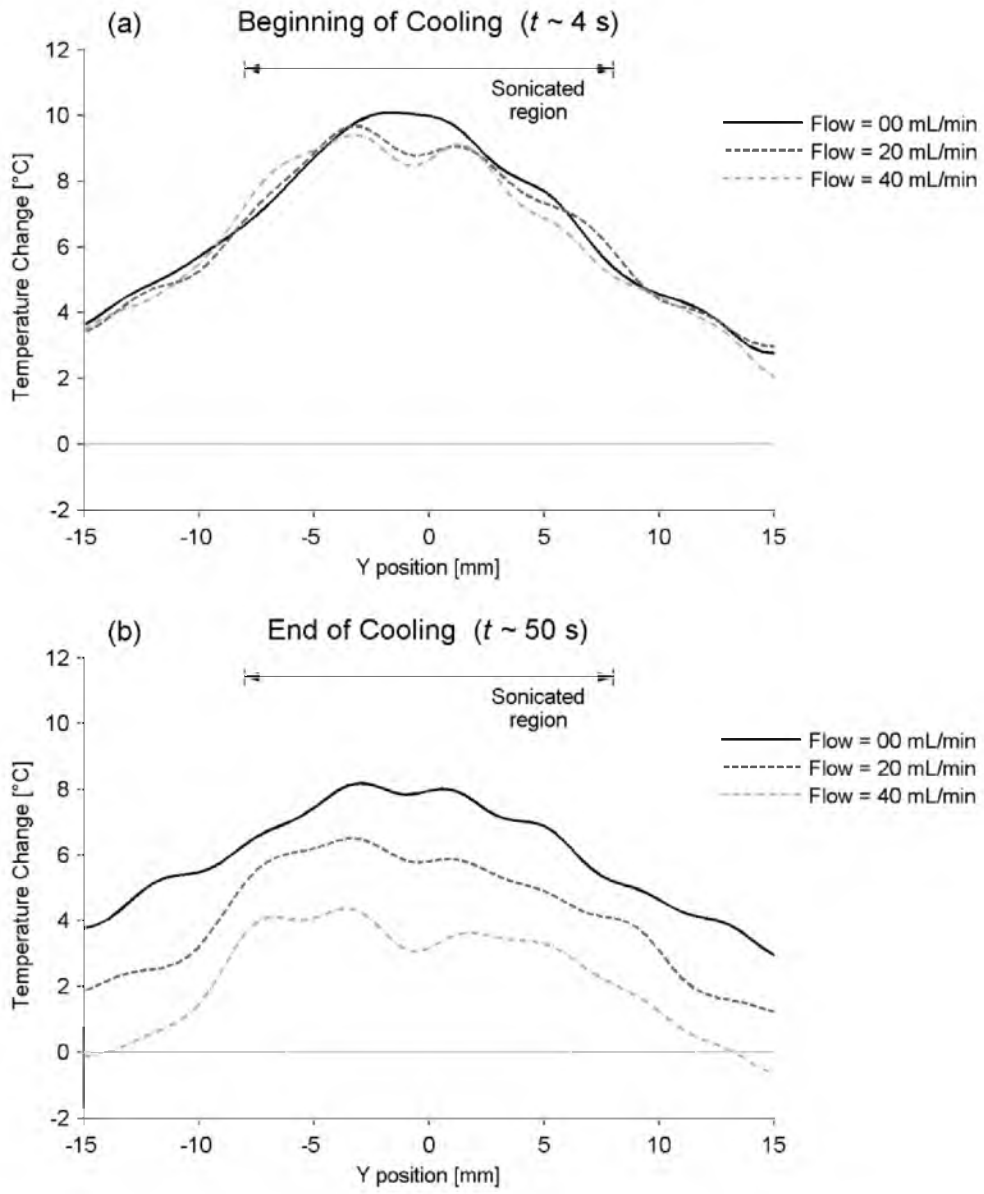

Figure 5.6: Experimental MR temperatures in the phase encode direction (perpendicular to the ultrasound beam axis) at the beginning of cooling (a) and at the end of cooling (b) for three flow rates in an *ex vivo* perfused kidney. The sonicated region indicates the radial spacing of the electronically steered focal positions.

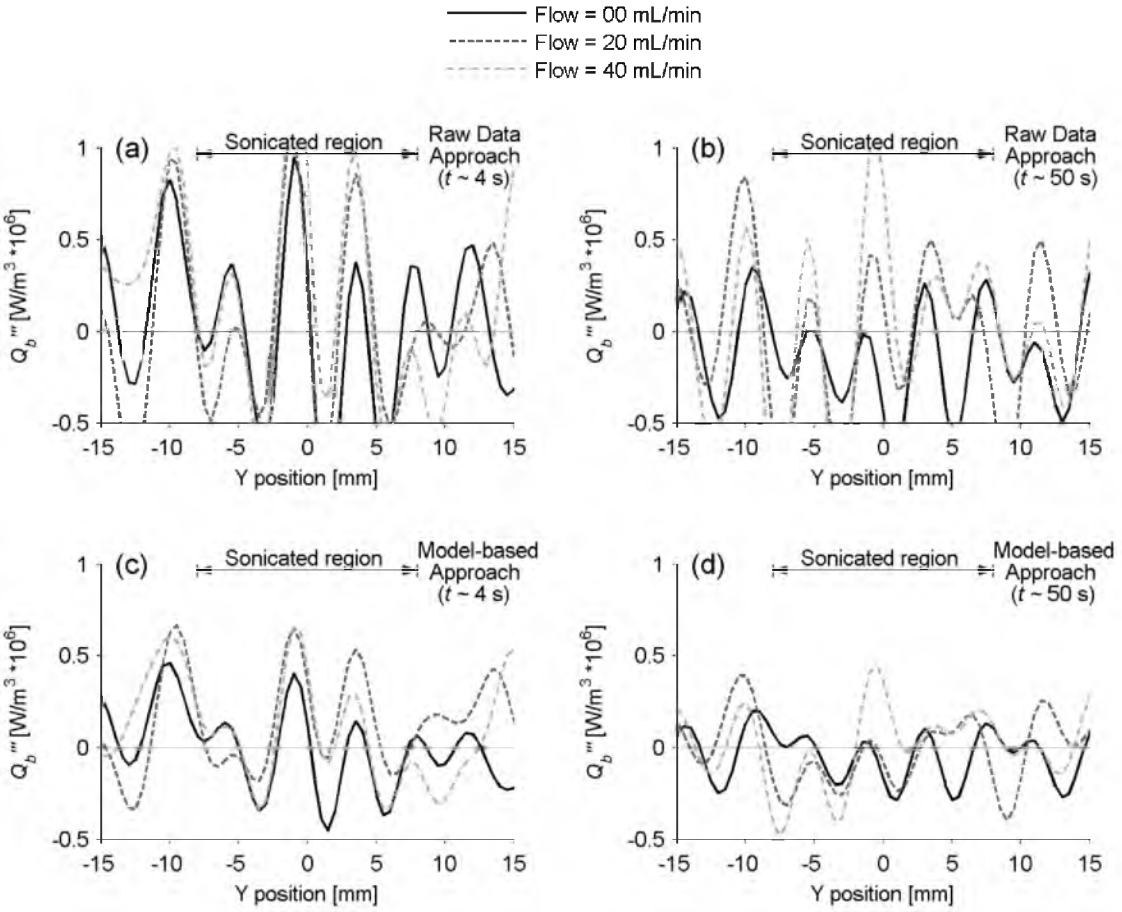

Figure 5.7: Local, dynamic estimates of perfusion-related energy losses ($\dot{Q}_{bl}'''$) early in the cooling period (a & c) and later in the cooling period (b & d) for three different flow rates. Times for $\dot{Q}_{bl}'''$ values correspond to the temperatures of Figure 5.6. Estimates from the raw data approach for estimating $\dot{Q}_{bl}'''$ are shown in (a) and (b) while estimates from the model-based approach are given in (c) and (d).

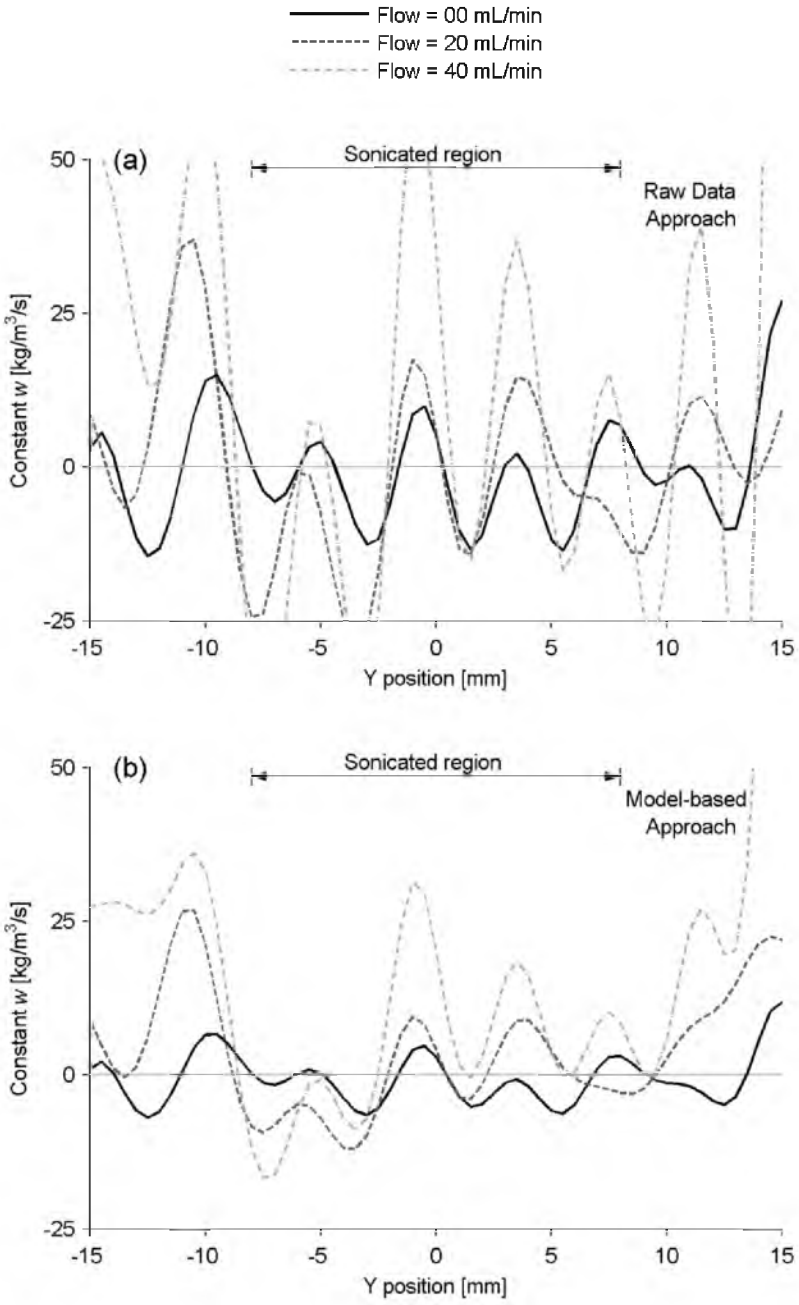

Figure 5.8: Local Pennes perfusion parameter w values have been optimized for a single constant value over the first 50 s of cooling. Results for the (a) raw data approach and the (b) model-based approach are shown for three different flow rates.

Figure 5.9 shows estimates for all nine heating runs (three series of heatings with three flow rates) when a constant, uniform w value is calculated for a 1.0-cm^3 region of interest in the center of the heated volume over the first 50 s of cooling (Least-squares optimization of Equation 5.7 with MATLAB function *fminsearch*). Values from the raw data approach are shown in Figure 5.9a and the model-based approach results are presented in Figure 5.9b. For both approaches, estimates of w for the zero perfusion case are within ±0.8 $kg/m^3/s$. Increases in flow rate correspond to a nearly linear increase in the Pennes perfusion parameter w for each series of runs. The results presented in Figures 5.5-5.8 correspond to the second series of data in Figure 5.9.

Figure 5.10 repeats the experimental temperature profiles of Figure 5.6b at ~50 s into cooling along with simulated data. These simulated data were modeled using the experimental temperature data at ~4 s into cooling (Figure 5.6a) as an initial condition, thermal properties determined by the methods of Chapter 4, and with Pennes perfusion values taken from the constant, uniform w estimates of Figure 9b. These w values, optimized from the central 1 cm^3 of data, were applied throughout the entire tissue volume. The average magnitude of temperature differences after 50 s in the optimized region for the 0, 20, and 40 mL/min cases were 0.2, 0.7, and 1.0 °C, respectively.

5.5 Discussion

5.5.1 Key points of results

Figures 5.3 and 5.4 demonstrate the ability of both approaches to converge to the correct perfusion distribution. These simulations help to verify both the theory and MATLAB code implementation.

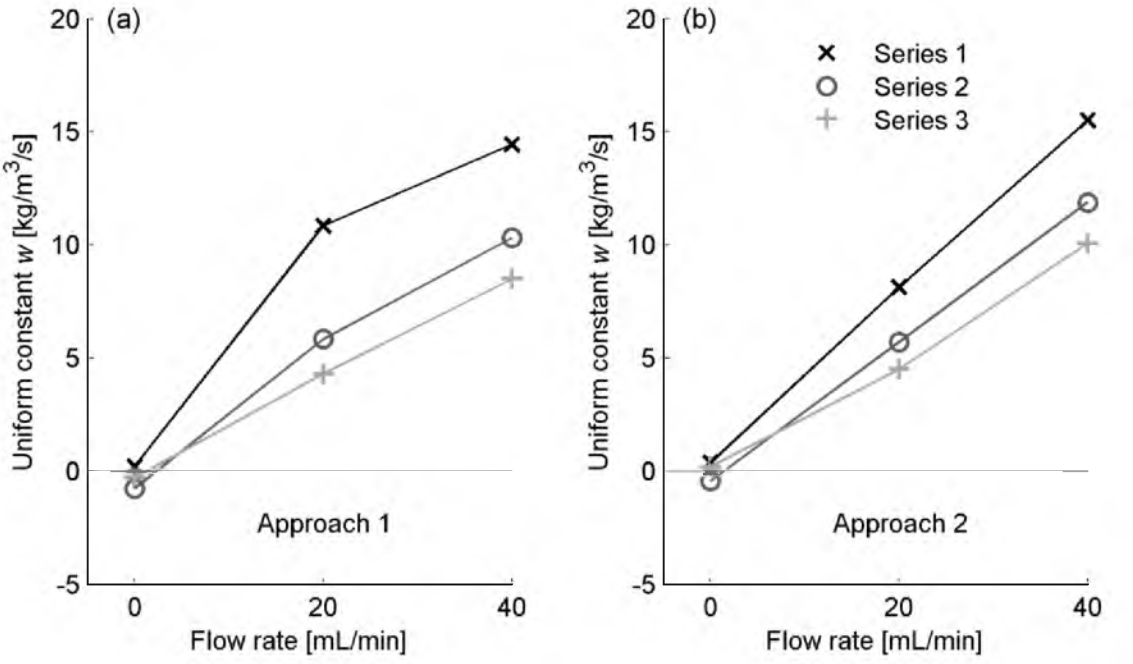

Figure 5.9: Uniform, constant estimates of the Pennes perfusion parameter w were made for all nine runs (three sequential series with three different flow rates). The optimization included all $\dot{Q}_{bl}'''$ values from 50 s of cooling data in a 1 cm^3 region at the center of the heated volume. Results of the raw data approach and the model-based approach are given in (a) and (b), respectively.

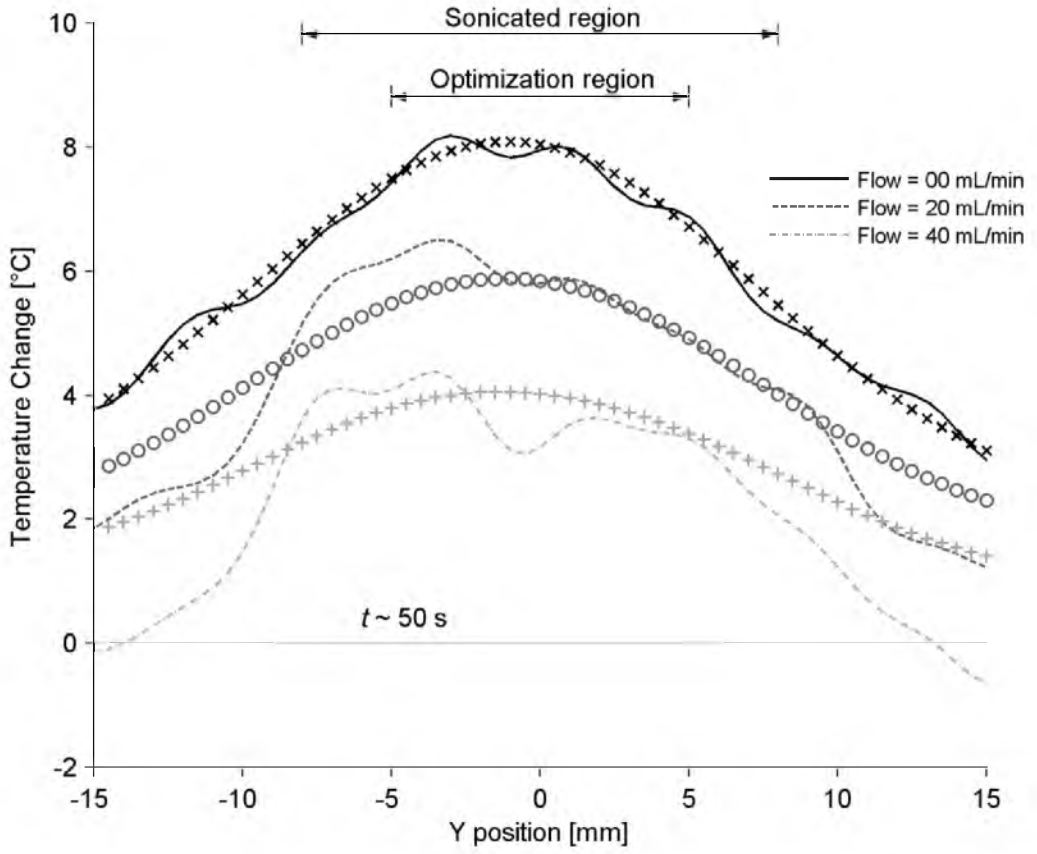

Figure 5.10: Modeled temperatures using uniform, constant *w* estimates (see Figure 5.9b) for no-flow (x marker), 20 mL/min (o marker), and 40 mL/min (+ marker) cases are compared with experimental data first presented in Figure 5.6b. The temperature profiles from Figure 5.5a were used as an initial condition for the model.

In Figure 5.6, the nearly uniform decay of temperatures for the different flow cases indicates that there are likely no large vessels in this region. The oscillations observed in later figures are also present in these data, but on a much smaller scale.

$\dot{Q}_{bl}'''$ estimates in Figure 5.7 are obtained on a point-by-point basis and are dynamic in time; hence, they are very noisy. This indicates that averaging or optimization in time and/or space will be important for obtaining meaningful w values. Taking spatial derivatives in the estimation process amplifies the oscillatory artifact in the temperature data. The oscillations observed in these data are not due to any real distribution of flow in the kidney or artifacts induced by the flow since they are also observed in the no-flow case.

Obtaining w estimates that are constant in time can help reduce noise and oscillations as seen in Figure 5.8. In this figure, the model-based approach appears more stable than the raw data approach.

With spatial optimization in addition to temporal optimization, a near linear relationship between flow rate and the constant, uniform Pennes perfusion parameter w is observed in Figure 5.9. While not perfect, consistency between runs and series is encouraging.

With no independent perfusion measurements, testing the predictive power of w estimates is an appropriate, but admittedly less than ideal, method for assessing the magnitude of w values. The temperatures profiles in Figure 5.10 are predicted very well in the region used for perfusion optimization. In adjacent regions, over-prediction of temperatures suggests that perfusion may have been higher at those positions. Indeed,

when the optimization region was increased to include all of the data in Figures 5.5-5.9, estimates of w increased approximately 10%.

5.5.2 General points of discussion

The two approaches for estimating $\dot{Q}_{bl}'''$ have two major differences. First, both equations used for estimating $\dot{Q}_{bl}'''$ (Equations 5.1 and 5.6) include the term $\rho c \frac{dT_{exp}}{dt}$, but the raw data approach evaluates the time derivative with a central difference approximation and the model-based approach utilizes a forward difference approximation. Therefore, the time over which the derivative is evaluated is twice as long in the raw data approach as it is in the model-based approach. With dynamic temperature profiles that change quickly, especially early in the cooling period, a shorter time for this approximation would be beneficial.

The second major difference in the approaches is found in the second term required for $\dot{Q}_{bl}'''$ quantification. In the raw data approach, the term $k\nabla^2 T_{exp}$ is calculated for each voxel based upon its own temperature and the temperatures of the six voxels immediately adjacent to it for a single measurement in time, as defined by Equation 5.2. Using so few data to estimate a spatial derivative makes it extremely susceptible to noise. In contrast, the second term of the model-based approach is given by $\rho c \frac{\Delta T_{sim}}{t_{acq}}$. From Equation 5.4, it can be seen that this simulated time derivative is equal to the spatial derivative $k\nabla^2 T_{sim}$. Because the model-based approach uses finite-difference temperatures for which the time step is necessarily much smaller than t_{acq}, this spatial derivative will be influenced by not only the voxel and its immediate neighbors, but by their neighbors and more distant

voxels as well. This spreading effect can reduce the errors induced by local noise or temperature artifacts.

Based upon the results of this study, pursuing the development of the model-based approach appears to be advantageous. In simulations, this approach accurately estimated w for both cases in a point-by-point dynamic analysis. In the experimental data, noise and oscillations in estimates of $\dot{Q}_{bl}'''$ and w were substantially reduced for the reasons discussed in the previous paragraph. It is noteworthy that the spreading effect of using this model-based approach was seen in simulations. The sharp transition between tissue types of different perfusion values in Figure 5.4 is captured cleanly by the raw data approach, but is more gradual with the model-based approach because in the model-based approach, data from both tissue types affect estimates in the vicinity of the tissue boundary.

Looking at the zero-flow results for the model-based approach, it is clear that there is significant room for improvement in these experiments. For constant point-by-point estimates (Figure 5.8b), w values that should be zero have a range of approximately ±6 kg/m^3/s, nearly reaching brain perfusion values. Even when a uniform, constant perfusion is assumed in the sonicated region, no-flow estimates were in the range of perfusion values for fat and resting muscle.

Of positive note, the overall magnitudes of w estimates in the sonicated region are realistic for all flow rates. Experimental uniform, constant perfusion estimates for a flow of 40 mL/min ranged from 10-15 kg/m^3/s (Figure 5.9b). These values are, as anticipated, a fraction of published values (69 kg/m^3/s) for *in vivo* kidney [9], because the pressures attainable in the *ex vivo* setting are much lower than those experienced *in vivo*.

Additionally, with a flow rate of 40 mL/min and the approximate volume of the excised kidney (64 cm^3), a simple estimate of uniform perfusion under the experimental conditions can be calculated at approximately 10 $kg/m^3/s$. Such results demonstrate the potential of this approach to, with continued improvements, evaluate biothermal models like the PBHTE.

5.5.3 Specific recommendations for future experiments

The following recommendations for improving the experimental setup and reconstruction methods used in these experiments will result in better-quality MR temperature data and, by extension, more accurate estimates of perfusion-related energy losses.

First, dope the water tank used for ultrasound coupling with manganese chloride. The high-power FUS used in these experiments can induce water motion and eddy currents inside the tank that introduce artifacts into MR images, temperature measurements, and temperature-based estimation methods. The oscillatory artifact observed in these data may be caused, at least in part, by this water motion. Sharp signal changes, such as those at water-air interfaces, can also induce ringing. By doping the water, its strong signal is minimized and artifacts associated with it can be substantially reduced.

Second, place additional unheated tissue in the field of view to assist in referenceless temperature reconstruction techniques. Because the heated region is large and diffuse, there is limited tissue in the kidney that does not experience temperature change. Referenceless reconstruction algorithms [22] can help reduce motion or phase drift artifacts, but require unheated tissues from which the background phase can be

determined. Introducing a piece of meat or agar adjacent to the kidney could serve this purpose in addition to stabilizing the kidney from motion caused by water eddies.

Third, place fiberoptic probes to monitor temperatures in the kidney and in the heparinized water inflow. These temperature measurements will ensure the temperature is stable and consistent before each run and will help identify any shift in baseline temperature.

Fourth, calibrate the flow exiting the kidney for each flow rate. While the pump prescribes a flow value, ensuring this value is accurate and consistent will improve confidence in results. Kidney outflow should also be diverted outside of the water tank to prevent mixing of the heparinized water with doped water in the tank.

Fifth, generate an independent measurement of local perfusion in the kidney at each flow rate. To fully validate biothermal models such as the PBHTE, an independent measure of perfusion is essential. MR approaches such as arterial spin labeling and gadolinium-based DCE [23-24] are non- or minimally invasive and would be appropriate for use in *in vivo* and eventually human validation studies.

5.6 Conclusion

The noninvasive, three-dimensional dynamic measurements of these approaches for quantifying perfusion-related energy losses and evaluating biothermal models are a step forward from past validation efforts. There is value in the fact that estimates of perfusion-related energy losses can be used to evaluate any existing or future biothermal model. The approaches also demonstrate flexibility in quantifying perfusion-related energy losses. Estimates can be fully dynamic or constant in time. They can be

evaluated on a point-by-point basis, discretized into regions, or assumed uniform in space. While significant improvements are needed for estimates of perfusion-related energy losses to have the desired resolution and accuracy, these approaches show promise for making possible the evaluation of biothermal models used in MRgFUS thermal therapies.

5.7 References

1. Billard B, Hynynen K, Roemer RB (1990) Effect of physical parameters on high temperature ultrasound hyperthermia. Ultrasound Med Biol 16: 409-420.

2. Chen L, Rivers I, ter Haar G, Riddler S, Hill CR, et al. (1993) Histological changes in rat liver tumours treated with high-intensity focused ultrasound. Phys Med Biol 19: 67-74.

3. McDannold N, Tempany CM, Fennessy FM, So MJ, Rybicki FJ, et al. (2006) Uterine leiomyomas: MR imaging–based thermometry and thermal dosimetry during focused ultrasound thermal ablation. Radiology 240: 263-272.

4. Zhang L, Zhu H, Jin C, Zhou K, Li K, et al. (2009) High-intensity focused ultrasound (HIFU): effective and safe therapy for hepatocellular carcinoma adjacent to major hepatic veins. Eur Radiol 19: 437-445.

5. Payne A, Vyas U, Todd N, de Bever J, Christensen DA, et al. (2011) The effect of electronically steering a phased array ultrasound transducer on near-field tissue heating. Med Phys 38: 4971-4981.

6. Cheng HL, Plewes DB (2002) Tissue thermal conductivity by magnetic resonance thermometry and focused ultrasound heating. J Magn Reson Imaging 16: 598-609.

7. Pennes HH (1948) Analysis of tissue and arterial blood temperatures in the resting human forearm. J Appl Physiol 1: 93-122.

8. Roemer RB and Dutton AW (1998) A generic tissue convective energy balance equation: Part I-theory and derivation. J Biomech Eng 120: 395-404.

9. Hasgall PA, Neufeld E, Gosselin MC, Klingenböck A, Kuster N (2013) IT'IS database for thermal and electromagnetic parameters of biological tissues. Version 2.4. www.itis.ethz.ch/database

10. Roemer RB, Forsyth K, Oleson JR, Clegg ST, Sim DA (1988) The effect of hydralazine dose on blood perfusion changes during hyperthermia. Int J Hyperthermia 4: 401-415.

11. Wissler EH (1988) An analytical solution countercurrent heat transfer between parallel vessels with a linearaxial temperature gradient. J Biomech Eng 110: 254-256.

12. Strohbehn JW, Curtis EH, Paulsen KD, Yuan XC, Lynch DR (1989) Optimization of the absorbed power distribution for an annular phased array hyperthermia system. Int J Radiat Oncol Biol Phys 16: 589-599.

13. Clegg ST, Roemer RB (1993) Reconstruction of experimental hyperthermia temperature distributions: application of state and parameter estimation. J Biomech Eng 115: 380-388.

14. Arkin H, Xu LW, Roemer RB (1994) Recent developments in modeling heat transfer in blood perfused tissues. IEEE Trans Biomed Eng 41: 97-107.

15. Kolios MC, Worthington AE, Sherar MD, Hunt JW (1998) Experimental evaluation of two simple thermal models using transient temperature analysis. Phys Med Biol 43: 3325-3340.

16. Vyas U, Christensen DA (2012) Ultrasound beam simulations in inhomogeneous tissue geometries using the hybrid angular spectrum method. IEEE Trans Ultrason Ferroelectr Freq Control 59: 1093-1100.

17. Holmes KR, Ryan W, Weinstein P, Chen MM (1984) A fixation technique for organs to be used as perfused tissue phantoms in bioheat transfer studies. ASME Adv Bioeng 9–10.

18. Payne A, Merrill R, Minalga E, Vyas U, de Bever J, et al. (2012) Design and characterization of a laterally mounted phased-array transducer breast-specific MRgHIFU device with integrated 11-channel receiver array. Med Phys 39: 1552-1560.

19. Payne A, Goodrich KC, Kholmovski EG, Roemer RB, Parker DL. (2008) Isolated kidney phantom for development of biothermal vascular models with application to high intensity focused ultrasound therapy. Med Phys 35: 4426-4434.

20. De Poorter JD, De Wagter C, De Deene Y, Thomsen C, Stahlberg F, et al. (1995) Noninvasive MRI thermometry with the proton resonance frequency (PRF) method: in vivo results in human muscle. Magn Reson Med 33: 74-81.

21. Ishihara Y, Calderon A, Watanabe H, Okamoto K, Suzuki Y, et al. A precise and fast temperature mapping using water proton chemical shift. Magn Reson Med 33: 814-823.

22. Rieke V, Vigen KK, Sommer G, Daniel BL, Pauly JM, et al. (2004) Referenceless PRF shift thermometry. Magn Reson Med 2004: 1223-1231.

23. Knutsson L, van Westen D, Petersen ET, Bloch KM, Holtas S, et al. (2010) Absolute quantification of cerebral blood flow: correlation between dynamic susceptibility contrast MRI and model-free arterial spin labeling. Magn Reson Imag 28: 1–7.

24. Winter JD, St Lawrence KS, Cheng HLM (2011) Quantification of renal perfusion: comparison of arterial spin labeling and dynamic contrast-enhanced MRI. J Magn Reson Imag 34: 608-615.

CHAPTER 6

CONCLUSION

6.1 Impact

The intended goal of this dissertation was to develop a systematic approach for estimating parameters from the general bioheat transfer equation that can be used in the evaluation of specific biothermal models. For decades, estimation of parameters from experimental temperature data has been done using invasive temperature probes at discrete locations. Experimental uncertainty in probe position, the limited spatial information discrete probes provide, and the fact that invasive probes can alter local physiology and interfere with heating distributions are a few of the challenges previous research studies have faced. These limitations have prevented biothermal models such as the Pennes bioheat transfer equation from being thoroughly and systematically validated for over half a century. The recent development of noninvasive fully three-dimensional dynamic temperature measurement with MRI and the ability of FUS to noninvasively heat deep tissues, coupled with the methods and approaches presented in this dissertation, provide a foundation for a complete and extensive evaluation of existing and future models of heat transfer in living tissues.

The work presented in this dissertation makes other contributions to the scientific community as well. Chapter 2 provides an empirical approach to accurately estimating

FUS SAR that will be useful in the validation of ultrasound modeling software that include the effects of scattering, multiple reflections, and refraction. Chapter 3 provides guidelines for researchers to prevent errors in MR temperature measurements that would introduce systematic bias in parameter estimation values. Chapter 4 introduces a noninvasive method for estimating tissue thermal diffusivity that can be used to expand the literature on tissue-specific biothermal properties. If coupled with MR methods for three-dimensional flow quantification, the approaches of Chapter 5 could be used to address the challenge of linking blood perfusion measurements to the thermal energy losses caused by perfusion. Local anomalies in experimental temperature fields could be compared with blood vessel angiography to continue the discussion on the size of thermally significant blood vessels.

The clinical implications of this work in the field of MRgFUS are significant. The American Association of Physicists in Medicine (AAPM) is currently discussing the role of medical physicists in FUS treatments. Preliminary work such as that found in this dissertation can help establish standards for biothermal models. Employed in pretreatment planning, consistent modeling standards will help to ensure the safety, efficiency, and efficacy of treatments. Biothermal models can be utilized in the monitoring of treatments, increasing the spatial resolution or volumetric coverage of temperature measurements without sacrificing temporal resolution via methods such as Kalman filtering or model predictive filtering. Real-time feedback controllers can utilize information from biothermal models to optimize treatments, reducing treatment times, cost, and risk to patients. These contributions apply to all MRgFUS treatments regardless of treatment site and promise to increase scientific and clinical confidence in MRgFUS.

A current trend in cancer therapy is the shift toward combined therapy. In principle, the initial treatment stresses cancer cells so they are weakened before being hit with a second, alternate therapy, thus maximizing the therapeutic effect. FUS is ideal for combination treatment of cancer. Because FUS works best in low perfused regions (greater heating ability) and radiation and drug delivery are optimal with high perfusion, FUS is a natural complement to these therapies. As discussed in Chapter 1, FUS can also improve radiation or chemotherapy directly by increasing vascular permeability and perfusion levels. FUS can be used to release targeted therapeutic agents directly to the tumor via temperature-sensitive liposomes or microbubbles and can also stimulate an immune response to further attack cancer cells. With ongoing improvements in its science and technology and continued progress in clinical acceptance and awareness of focused ultrasound's potential, MRgFUS may become a great tool for improving clinical outcomes and cancer patients' treatments and quality of life.

6.2 Future work

Recommendations for future work can be divided into two categories: first, improvement of techniques developed in this dissertation and second, application of those techniques to assist in new research objectives.

6.2.1 Improvement of techniques

It is anticipated that great improvements in the quantification of perfusion-related energy losses will be made by implementing the recommendations discussed at the end of Chapter 5. More generally, any improvements to the accuracy and precision of MR

temperature imaging will yield better estimates for all of the bioheat transfer parameters, because all of these techniques are established upon those experimental temperature data. While this may seem obvious, the effect of better temperature measurements will not be trivial and the clinical implementation of these techniques may well rely upon improved MR data.

It is especially apparent from the results presented in Chapter 5 that there is room for improvement. The PRF temperature algorithm is based upon a difference of phases between images. $\dot{Q}_{bl}'''$ quantification also utilizes difference techniques. Difference techniques are naturally susceptible to noise errors and implementing two of these techniques magnifies this drawback.

The development of application-specific RF coils will boost signal strength and mitigate noise in the data. Optimal placement and weighting of signals from multiple receiver coils will maximize temperature accuracy. Improved temperature reconstruction techniques can help eliminate artifacts from motion and field drift. For the approaches of Chapter 5, developing an appropriate referenceless temperature reconstruction method will help significantly. Finding the optimal balance between spatial resolution, temporal resolution, and signal strength for these techniques is another area of research that may prove useful.

A different way to reduce noise or artifacts in the temperatures is to apply spatial filters to the MR data. While this reduces spatial resolution, it may be necessary for reliable measurements. This can be done to the raw data before the temperature image is reconstructed with a Hanning or other filter. Temporal filtering can also be applied that lowers noise in the reference image and reduces the errors associated with the difference

technique. Alternatively, the reconstructed temperature distributions can be fit with different solutions in space or in time to smooth the data. Investigating which filtering approaches yield the best results while sacrificing the least amount of detail is worth pursuing.

6.2.2 Application of techniques

The first application of these techniques is in the critical evaluation and validation of biothermal models, such as the Pennes bioheat transfer equation. However, before those evaluations can be performed, an independent measure of the blood perfusion is required. There exist several MRI techniques for quantifying perfusion, locating blood vessels, and measuring three-dimensional blood flow fields, including arterial spin labeling (ASL), blood-oxygen-level dependent (BOLD) imaging, diffusion tensor imaging (DTI), and MR angiography. Finding an imaging technique that can acquire accurate perfusion measurements with spatial and temporal resolutions comparable to those of MRTI would be very beneficial.

Combining these measurements with our approach for determining perfusion-related energy losses would open the possibility of establishing a link between perfusion measurements and perfusion-related energy losses in MRgFUS. Establishing such a link would provide clinicians with a safe, reliable way to determine accurate patient-specific thermal model parameters before any therapeutic heating occurs in the tissue.

As discussed in Chapter 5, one of the primary advantages of our approach is that estimates of $\dot{Q}_{bl}'''$ can be used to evaluate any biothermal model. The spatiotemporal approximations, advantages, and limitations of the Pennes bioheat transfer equation, the

k-effective model, or other biothermal models can be compared directly.

Finally, it would be valuable to investigate how these techniques could assist or improve temperature monitoring techniques like model predictive filtering. Addressing how much spatial and temporal detail is necessary in biothermal models for accurate prediction and what gains are achieved by the additional complexity of the model will be very valuable to the MRgFUS community. The same questions could be addressed for implementing these models in a real-time feedback controller for MRgFUS therapies.

In conclusion, successful investigation of these challenges and implementation of the techniques developed in this dissertation will provide a means for more accurate treatment planning of thermal therapies, improved consistency and safety of treatments, and ultimately greater clinical acceptance for thermal therapies as an alternative to traditional cancer treatments.

APPENDIX

MATLAB CODE

```
% -------- Function Name --------
%       Find_beamaxis_v3.m
% -------- Purpose --------
%   Finds the exact US beam axis location in all slices based on 2-D
%   temperature data from several timesteps by fitting a Gaussian to
%   the temperature data in x- and y- directions.  Averages x and y
%   beam location from different timesteps analyzed.  A linear fit to
%   the beam locations selected slices then ensures that the beam axis
%   is a straight line through the imaging volume.  The beam axis must
%   be identified prior to running code Calc_SARfield_v7.m.
% -------- Input Data --------
%       TEMPS       [nX,nY,nZ,nt]. 4D temperature data.  Axis of
%                   ultrasound beam should be approximately parallel to
%                   the z direction.
%       dx          voxel size in x-dir [mm]
%       dy          voxel size in y-dir [mm]
%       xlimit      2 element vector with min and max x voxels used to
%                   find beam axis
%       ylimit      2 element vector with min and max y voxels used to
%                   find beam axis
%       zlimit      2 element vector with min and max slices FOR LINEAR
%                   FIT, for 2D data use [1 1]
%       tlimit      2 element vector with min and max timesteps used to
%                   find beam axis
%       PLOT        'y' or 'n'.  Plots Gaussian fits over temperature
%                   data if  PLOT=='y'
%       DataType    scalar.  2 for 2D data, 3 for 3D data.
% -------- Output Data --------
%       x_loc       Linear Fit location of beam axis in x-dir (1st dim)
%       y_loc       Linear Fit location of beam axis in y-dir (2nd dim)
%       r           Linear Fit r locations
%       x_loc_sl    x-dir fitted loc of beam axis prior to linear fit
%       y_loc_sl    y-dir fitted loc of beam axis prior to linear fit
%       r_sl        r location prior to linear fit
% -------- Required Subfunctions --------
%       GaussianFunction.m
% -------- Author Info --------
%       Christopher Dillon
%       Department of Bioengineering
%       University of Utah
%       Version 1: 21 March 2012
% -------- Updates --------
%       v2      13 July 2012    Linear fit to x_loc_sl and y_loc_sl for
%                               beam axis location
%       v3      8 Feb 2013      2D or 3D data
function [r,x_loc,y_loc,x_loc_sl,y_loc_sl,r_sl] =
Find_beamaxis_v3(TEMPS,dx,dy,xlimit,ylimit,zlimit,tlimit,PLOT,DataType)
% -------- Identify variables --------
    close all
    if DataType==2  % 2D Data
        [nX,nY,nT]=size(TEMPS);nZ=1;else [nX,nY,nZ,nT]=size(TEMPS);
    end
    r_sl=zeros(nX,nY,nZ);x_loc_sl=zeros(nZ,1);y_loc_sl=zeros(nZ,1);  %
Preallocate data
% -------- Find r values --------
    h = waitbar(0,'Please wait... r values are being
calculated');count=0;  % Initialize waitbar
```

```
for zz=1:nZ      % Loop through z slices
    count=count+1;              % Increment counter
    waitbar(count/nZ,h);        % Update waitbar
    if DataType==2  % 2D Data
TEMPS2=squeeze(TEMPS(xlimit(1):xlimit(2),ylimit(1):ylimit(2),tlimit(1):
tlimit(2)));
    else
TEMPS2=squeeze(TEMPS(xlimit(1):xlimit(2),ylimit(1):ylimit(2),zz,tlimit(
1):tlimit(2)));% Identify temperatures to use for finding r in slice zz
    end
    [XX,YY,nt]=size(TEMPS2); % Size of truncated temperature data

    % In slice zz, find indices of max temperature in each timestep
    xmax=zeros(nt,1);ymax=zeros(nt,1); % Preallocate data
    for pp=1:nt                        % Loop through time steps
        T=squeeze(TEMPS2(:,:,pp));     % Temps for timestep pp
        [num idx] = max(T(:));% Value of max Temp in slice & index #
        [x y] = ind2sub([XX YY],idx);  % Convert index # to x and y
        xmax(pp)=x;            % x voxel of max Temp in this slice
        ymax(pp)=y;            % y voxel of max Temp in this slice
    end

    % In slice zz, find center location in the x-direction (1st dim)
xGauss=zeros(XX,nt);xMag=zeros(nt,1);xOffset=zeros(nt,1);xVariance=zero
s(nt,1);x_cen=zeros(nt,1);  % Preallocate data
    if (PLOT=='y' && zz<=zlimit(2) && zz>=zlimit(1));figure;end
    for pp=1:nt
        x_neg=-dx*(xmax(pp)-1);  % Most negative position
        x_pos=dx*(XX-1)+x_neg;   % Most positive position
        x_vec=x_neg:dx:x_pos;    % Position vector (initial guess)
        x0=[5 0 2];              % Initial guess for fitting parameters
        T=squeeze(TEMPS2(:,ymax(pp),pp))';% xdir TEMPS2 for timestep pp
        [params] = lsqcurvefit(@GaussianFunction,x0,x_vec,T);   %
least-squares curve fit to Gaussian
            xMag(pp)=params(1);
            xOffset(pp)=params(2);
            xVariance(pp)=params(3);
        xGauss(:,pp)=xMag(pp).*exp(-(x_vec-
xOffset(pp)).^2/xVariance(pp)); % Gaussian fit data for plot
        x_cen(pp)=xmax(pp)+xOffset(pp)/dx;% Center of beam, timestep pp
        if (PLOT=='y' && zz<=zlimit(2) && zz>=zlimit(1))
            J=xlimit(1):xlimit(2);
            plot(J,T,'k-x','LineWidth',1);hold on; % Plot temperature
data for timestep pp
            plot(J,xGauss(:,pp),'k--','LineWidth',1); % Plot Gaussian
curve fit for timestep pp
            xlim(xlimit);xlabel('X position');ylabel('Temperature');
        end
    end
    x_loc_sl(zz)=mean(x_cen)+(xlimit(1)-1); % Adjust position back to
untruncated initial data

    % If beam axis is determined to be outside the established limits
    % xlimit and ylimit, then beam axis value is set at nearest limit.
        if x_loc_sl(zz)<xlimit(1);x_loc_sl(zz)=xlimit(1);end
        if x_loc_sl(zz)>xlimit(2);x_loc_sl(zz)=xlimit(2);end
```

```
    % Find center location in the y-direction (2nd dim)
    if (PLOT=='y' && zz<=zlimit(2) && zz>=zlimit(1));figure;end

yGauss=zeros(YY,nt);yMag=zeros(nt,1);yOffset=zeros(nt,1);yVariance=zero
s(nt,1);y_cen=zeros(nt,1);  % Preallocate data
    for pp=1:nt
        y_neg=-dy*(ymax(pp)-1);  % Most negative position
        y_pos=dy*(YY-1)+y_neg;   % Most positive position
        y_vec=y_neg:dy:y_pos;    % Position vector (initial guess)
        y0=[5 0 2];              % Initial guess for fitting parameters
        T=squeeze(TEMPS2(xmax(pp),:,pp));% y dir TEMPS2 for timestep pp
        [params] = lsqcurvefit(@GaussianFunction,y0,y_vec,T);   %
least-squares curve fit to Gaussian
            yMag(pp)=params(1);
            yOffset(pp)=params(2);
            yVariance(pp)=params(3);
        yGauss(:,pp)=yMag(pp).*exp(-(y_vec-
yOffset(pp)).^2/yVariance(pp));  % Gaussian fit data for plot
        y_cen(pp)=ymax(pp)+yOffset(pp)/dy;% Center of beam, timestep pp
        if (PLOT=='y' && zz<=zlimit(2) && zz>=zlimit(1))
            I=ylimit(1):ylimit(2);
            plot(I,T,'k-x','LineWidth',1);hold on; % Plot temperature
data for timestep pp
            plot(I,yGauss(:,pp),'k--','LineWidth',1); % Plot Gaussian
curve fit for timestep pp
            xlim(ylimit);xlabel('Y position');ylabel('Temperature');
        end
    end
    y_loc_sl(zz)=mean(y_cen)+(ylimit(1)-1); % Adjust position back to
untruncated initial data

    % If beam axis is determined to be outside the established limits
    % xlimit and ylimit, then the beam axis value is set at the nearest
limit.
        if y_loc_sl(zz)<ylimit(1);y_loc_sl(zz)=ylimit(1);end
        if y_loc_sl(zz)>ylimit(2);y_loc_sl(zz)=ylimit(2);end

    for xx=1:nX
        for yy=1:nY
            r_sl(xx,yy,zz)=((dx*(xx-x_loc_sl(zz)))^2+(dy*(yy-
y_loc_sl(zz)))^2)^0.5;
        end
    end
end
close(h);

% -------- Linear Fit for final x_loc, y_loc, and r values --------
if zlimit(1)~=zlimit(2)
    a=zlimit(1):zlimit(2); zloc=1:nZ;
    % Linear fit for x beam axis
        x_LinFit=polyfit(a,x_loc_sl(a)',1);
        x_loc=x_LinFit(1)*zloc+x_LinFit(2);
    % Linear fit for y beam axis
        y_LinFit=polyfit(a,y_loc_sl(a)',1);
        y_loc=y_LinFit(1)*zloc+y_LinFit(2);
```

```
    % Calculate Linear Fit r values
    clear xx yy zz
    r=zeros(nX,nY,nZ);              % Preallocate data
    for xx=1:nX
        for yy=1:nY
            for zz=1:nZ
                r(xx,yy,zz)=((dx*(xx-x_loc(zz)))^2+(dy*(yy-
y_loc(zz)))^2)^0.5;
            end
        end
    end
else  % Without multiple z locations, there is no linear fit
    x_loc=x_loc_sl;y_loc=y_loc_sl;r=r_sl;
    x_loc_sl=[];y_loc_sl=[]; r_sl=[];
end
% ------------------------------------------------------------------------
```

```
% -------- Function Name ----------------------------------------------
%       GaussianFunction.m
% -------- Purpose --------
%   Subfunction of Find_beamaxis_v3.m for fitting temperature data to a
%   Gaussian distribution
function F = GaussianFunction(x,xdata)
F = x(1)*exp(-(xdata - x(2)).^2/x(3));
% ------------------------------------------------------------------------
```

```
% -------- Function Name --------------------------------------------------------
%       Calc_SARfield_v7.m
% -------- Purpose --------
%       Calculates the 2D SAR field in slice of interest from 4D temperature
%       data by fitting those temperatures to the analytical solution for a
%       1D radial Gaussian heating & or cooling profile in a least-squares
%       manner. For each slice of temperature data, estimates are made for the
%       maximum SAR value, beam FWHM, and thermal diffusivity (Kappa).
%       Diffusivity estimates are most valid in slices at the center of the
%       focal zone where the assumption of a 1D radial Gaussian is most
%       valid.
% -------- Input Data --------
%       TEMPS       [nX,nY,nZ,nt]. 4D temperature data.  Axis of ultrasound
%                   beam should be approximately parallel to the z direction.
%       time        1xnt. Time vector corresponding to TEMPS.
%       HT          Scalar. Heating time in s.
%       r           [nX,nY,nZ]. Identifies radial distance from beam axis in mm
%       x_loc       1xnZ. Vector identifying beam axis location in each
%                   slice: 1st dimension.
%       y_loc       1xnZ. Vector identifying beam axis location in each
%                   slice: 2nd dimension.
%       cp          Scalar. Specific heat capacity of tissue in J/(kg*deg C)
%       timePts     Vector. Identifies which components in time to use for
%                   the fitting process. (Not a 2 element vector, include
%                   all time points for fitting)
%       zloc        Scalar.  Identifies slice in which estimates are made.
%       NumLocs     Scalar. Identifies how many voxels per slice to use for
%                   the fitting process.  Should be the square of an odd
%                   number (1,9,25,49,81,121,169,etc). Does not apply if
%                   CircSym='y'
%       CircSym     'y' or 'n'. Use circularly symmetric ROI in place of square
%                   ROI?
%       rad         Scalar. if CircSym='y', what radius [mm] to use for ROI
%                   from beam axis in slice of interest?
%       DataType    Scalar. 2 for 2D temperature data, 3 for 3D data.
% -------- Output Data --------
%       SAR         [nX,nY]. SAR estimates for 2D field in slice 'zloc' [W/kg].
%       FWHM        Scalar. Value of beam FWHM. [mm].
%       beta        Scalar. Value of beam variance. [mm^2].
%       C           Scalar. Value of fitting parameter C. [deg C/s].
%       Kappa       Scalar. Value of thermal diffusivity. [m^2/s].
%       TEMPS_Fit   [nX,nY,length(timePts)]. Least-squares fit to
%                   temperature data.
%       time_Fit    1xlength(timePts). Time vector corresponsing to TEMPS_Fit.
%       TEMPS_Ana   [nX,nY,nt]. Temperatures calculated from fitting
%                   parameters for entire slice and all time points.
% -------- Required Subfunctions --------
%       analyticalfit6.m
% -------- Author Info --------
%       Christopher Dillon
%       Department of Bioengineering
%       University of Utah
%       Version 1: 4 May 2012
% -------- Updates --------
%       v2      31 October 2012             Rewrote to be a function
%                                           Commented and condensed code
%                                           'x' and 'y' are 1st and 2nd
%                                              dimensions, respectively
%                                           'r' used as an input
%       v4      8 February 2013             Merged with HeatCoolFit_v2
%                                           Output TEMPS_Fit and TEMPS_Ana
%                                           2D or 3D data
%       v5      26 June 2013                Forced user specified beam width
```

```
%       v6      28 October 2013             Option for circularly symmetric ROI
%                                              instead of square ROI
%                                           Only calculates for a single slice
%                                              at a time
%       v7      28 May 2014                 Output fitting parameters Beta and
C
function
[SAR,beta,C,FWHM,Kappa,TEMPS_Fit,time_Fit,TEMPS_Ana,NumLocs,SAR_CalcTime]=Calc_
SARfield_v7(TEMPS,time,HT,r,x_loc,y_loc,cp,timePts,zloc,NumLocs,CircSym,rad,Dat
aType)
% -------- Identify variables --------
    totaltime=tic; % Start timer
    [nX nY nZ nt]=size(TEMPS);
    if DataType==2
        TEMPS=reshape(TEMPS,nX,nY,1,nZ);
    end
    [nX nY nZ nt]=size(TEMPS);
    ttot=length(timePts);      % Total number of time points to use for fitting
    time_Fit=time(timePts);    % Times to use for fitting
        ON=find(time_Fit<=HT); % Time steps when ultrasound is on
        OFF=find(time_Fit>HT); % Time steps when ultrasound is off

% -------- Identify temperatures and r values to use for fitting process in
each slice --------
    if CircSym=='y'
        r_new=squeeze(r(:,:,zloc));
        TEMPS_new=squeeze(TEMPS(:,:,zloc,timePts));
        LOCS=find(r_new<rad);
        NumLocs=length(LOCS)
        [xx yy]=ind2sub(size(r_new),LOCS);
        TEMPS_Ana=zeros(NumLocs,ttot);
        rval=r_new(LOCS)*1e-3; % 1xNumLocs vector of r-values converted to m
        mask=zeros(nX,nY);
        for nn=1:NumLocs
            TEMPS_Ana(nn,:)=squeeze(TEMPS_new(xx(nn),yy(nn),:));
            mask(xx(nn),yy(nn))=1;
        end
        xmin=min(xx);xmax=max(xx);ymin=min(yy);ymax=max(yy);
        figure;imagesc(mask)
    else  % Square ROI defined by NumLocs input
        TEMPS_Ana=zeros(NumLocs,ttot);  % Preallocate truncated experimental
temperatures to use for SAR estimates
        rval=zeros(1,NumLocs);          % Preallocate r values per slice
        bb=(round(sqrt(NumLocs))-1)/2;  % Number of voxels away from central
voxel in each of first two dimensions to use for fitting
            xmin=round(x_loc(zloc))-bb; % Min vox value for fit in the x dir
            xmax=round(x_loc(zloc))+bb; % Max vox value for fit in the x dir
            ymin=round(y_loc(zloc))-bb; % Min vox value for fit in the y dir
            ymax=round(y_loc(zloc))+bb; % Max vox value for fit in the y dir
        n=0;                            % Initialize counter
            for ii=xmin:xmax
                for jj=ymin:ymax
                    n=n+1;              % Counter, up to NumLocs for each slice
                    TEMPS_Ana(n,:)=squeeze(TEMPS(ii,jj,zloc,timePts)); % Select
TEMPS for fitting in each slice
                    rval(n)=r(ii,jj,zloc)*1e-3; % Select r-values for fitting
and convert to meters
                end
            end
        clear ii jj
    end
    r_sq=rval.^2;   % radius-squared values
% -------- Fit the temperature data to find estimates --------
```

```
    SARtime=tic;                        % Start timer on SAR calculation time
    h = waitbar(1,'Please wait... SAR is being calculated');cc=0; % Initiate
waitbar
    cc=cc+1;waitbar(cc/1,h);                                    % Update waitbar
        [estimates,model] = analyticalfit6(time_Fit,TEMPS_Ana,r_sq,HT);    %
Fit temperature data to analytical solution
                C=estimates(1);                 % 2*alpha*Io/(rho*cp)
                Kappa=estimates(2)*1e-6;        % Kappa: thermal diffusivity
                Beta=estimates(3)*1e-6;         % Beta: beam variance
    SAR_CalcTime=toc(SARtime)                   % Time elapsed calculating SAR
    close(h)                                    % close waitbar
    STDV=(Beta/2)^0.5;            % Relation of variance and standard deviation
    FWHM=STDV*2*sqrt(2*log(2))*1000;           % Relation of STDV and FWHM [mm]
    beta=Beta*1e6;
% -------- Find SAR for 2D field --------
   SAR=zeros(nX,nY);                % Preallocate data
    for ii=1:nX
        for jj=1:nY
                SAR(ii,jj)=cp*C*exp(-(r(ii,jj,zloc)*1e-3)^2/Beta);
        end
    end
    clear ii jj
% ----------------Calculate Fitted Temperatures from Analytical Solution and
parameter values---------------
    TEMPS_Fit=single(zeros(nX,nY,ttot)); % Preallocate Fitted Temperatures
    q = waitbar(0,'Please wait... Temperatures are being evaluated');ddd=0; %
Initiate waitbar
    if CircSym=='y'
        for nn=1:NumLocs
            ddd=ddd+1;waitbar(ddd/(NumLocs),q);        % Update waitbar
            if rval(nn)==0     % Center of beam (r=0) temperature solution

TEMPS_Fit(xx(nn),yy(nn),ON)=C*Beta/(4*Kappa)*log(1+4*Kappa/Beta*time_Fit(ON));

TEMPS_Fit(xx(nn),yy(nn),OFF)=C*Beta/(4*Kappa)*log((1+4*Kappa/Beta*time_Fit(OFF)
)./(1+4*Kappa/Beta*(time_Fit(OFF)-HT)));
            else               % Off-axis (r~=0) temperature solution

TEMPS_Fit(xx(nn),yy(nn),ON)=C*Beta/(4*Kappa).*(real(expint(squeeze(r_sq(nn))/Be
ta./(1+4*Kappa/Beta.*time_Fit(ON))))-real(expint(squeeze(r_sq(nn))/Beta)));

TEMPS_Fit(xx(nn),yy(nn),OFF)=C*Beta/(4*Kappa).*(real(expint(squeeze(r_sq(nn))/B
eta./(1+4*Kappa/Beta.*time_Fit(OFF))))...

real(expint(squeeze(r_sq(nn))/Beta./(1+4*Kappa/Beta.*(time_Fit(OFF)-HT)))));
            end
        end
    else  % Square ROI defined by NumLocs input
        for ii=xmin:xmax
            for jj=ymin:ymax
                    ddd=ddd+1;waitbar(ddd/(NumLocs),q);  % Update waitbar
                if r(ii,jj)==0 % Center of beam (r=0) temperature solution

TEMPS_Fit(ii,jj,ON)=C*Beta/(4*Kappa)*log(1+4*Kappa/Beta*time_Fit(ON));

TEMPS_Fit(ii,jj,OFF)=C*Beta/(4*Kappa)*log((1+4*Kappa/Beta*time_Fit(OFF))./(1+4*
Kappa/Beta*(time_Fit(OFF)-HT)));
                else           % Off-axis (r~=0) temperature solution
                    r_sq=r(ii,jj).^2*1e-6;

TEMPS_Fit(ii,jj,ON)=C*Beta/(4*Kappa).*(real(expint(r_sq/Beta./(1+4*Kappa/Beta.*
time_Fit(ON))))-real(expint(r_sq/Beta)));
```

```
TEMPS_Fit(ii,jj,OFF)=C*Beta/(4*Kappa).*(real(expint(r_sq/Beta./(1+4*Kappa/Beta.
*time_Fit(OFF)))).-
real(expint(r_sq/Beta./(1+4*Kappa/Beta.*(time_Fit(OFF)-HT))));
                end
            end
        end
    end
    close(q);  % Close waitbar
% ----------------Calculate All Temperatures from Analytical Solution and
parameter values---------------
    TEMPS_Ana=single(zeros(nX,nY,nt)); % Preallocate Fitted Temperatures
    NEG=find(time<0, 1, 'last' );% Number of time steps before ultrasound is on
    ON2=find(time<=HT);          % Time steps before ultrasound is turned off
    ON2=find(ON2>NEG);           % Cut off time steps before ultrasound is on
    OFF2=find(time>HT);          % Time steps after ultrasound is off
    qq = waitbar(0,'Please wait... Temperatures are being evaluated');dd=0; %
Initiate waitbar
        for ii=1:nX
            for jj=1:nY
                dd=dd+1;waitbar(dd/(nX*nY),qq); % Update waitbar
                if r(ii,jj)==0 % Center of beam (r=0) temperature solution

TEMPS_Ana(ii,jj,ON2)=C*Beta/(4*Kappa)*log(1+4*Kappa/Beta*time(ON2));

TEMPS_Ana(ii,jj,OFF2)=C*Beta/(4*Kappa)*log((1+4*Kappa/Beta*time(OFF2))./(1+4*Ka
ppa/Beta*(time(OFF2)-HT)));
                else           % Off-axis (r~=0) temperature solution
                    r_sq=r(ii,jj).^2*1e-6;

TEMPS_Ana(ii,jj,ON2)=C*Beta/(4*Kappa).*(real(expint(r_sq/Beta./(1+4*Kappa/Beta.
*time(ON2))))-real(expint(r_sq/Beta)));

TEMPS_Ana(ii,jj,OFF2)=C*Beta/(4*Kappa).*(real(expint(r_sq/Beta./(1+4*Kappa/Beta
.*time(OFF2)))).-
real(expint(r_sq/Beta./(1+4*Kappa/Beta.*(time(OFF2)-HT))));
                end
            end
        end
    close(qq);   % Close waitbar
TotalRunTime=toc(totaltime)  % Total time elapsed during function
% --------------------------------------------------------------------------
```

```
% -------- Function Name ----------------------------------------------
%       analyticalfit6.m
% -------- Purpose --------
%       Subfunction of Calc_SARfield_v7.m which uses fminsearch
%       optimization routine to fit analytical solution for a 1D radial
%       Gaussian to experimental temperature data.
% -------- Input Data --------
%       TIME        Vector of time points to use for fitting (in sec)
%       TEMPS       Matrix of Temperatures from all locations for fit &
%                   all time steps for fit. Size=(#locs,#timesteps)
%       r_sq        Vector of squared distances from beam axis for all
%                   locations for fit.
%       t_us        Total time that ultrasound is on
% -------- Output Data --------
%       estimates   Fitting parameters C, K, and B
function [estimates, model] = analyticalfit6(TIME,TEMPS,r_sq,t_us)
start_point = rand(1,3); % Call fminsearch with random starting point.
model = @anafun;
estimates = fminsearch(model, start_point);
% anafun accepts curve parameters as inputs, and outputs sse,the sum of
% squares error and the FittedCurve. FMINSEARCH only needs sse,
% but we want to plot the FittedCurve at the end.
    function [sse, FittedCurve] = anafun(params)
        % Determine which temperatures are heating and cooling
            ON=find(TIME<=t_us);  % Time steps when ultrasound is on
            OFF=find(TIME>t_us);  % Time steps when ultrasound is off
        C = params(1);  % 2*alpha*Io/(rho*cp)
        K = params(2);  % kappa
        B = params(3);  % beta
        FittedCurve=zeros(size(TEMPS));
        for mm=1:length(r_sq)  %
            if r_sq(mm)==0
                FittedCurve(mm,ON)=C*B/(4*K).*log(1+4*K/B*TIME(ON));

FittedCurve(mm,OFF)=C*B/(4*K).*log((1+4*K/B*TIME(OFF))./(1+4*K/B*(TIME(
OFF)-t_us)));
            else
                FittedCurve(mm,ON) =
C*B/(4*K).*(real(expint(r_sq(mm)/(B*1e-6)./(1+4*K/B.*TIME(ON))))-
real(expint(r_sq(mm)/(B*1e-6))));
                FittedCurve(mm,OFF)=
C*B/(4*K).*(real(expint(r_sq(mm)/(B*1e-6)./(1+4*K/B.*TIME(OFF))))...
                                        -real(expint(r_sq(mm)/(B*1e-
6)./(1+4*K/B.*(TIME(OFF)-t_us)))));
                % NOTE: If not in the ratio B/K, B and K would need to
be
                % multiplied by 1e-6
            end
        end
        ErrorVector = FittedCurve - TEMPS;
        ErrorVector_sq=ErrorVector.^2;
        sse = sum(ErrorVector_sq(:));
    end
end
% ------------------------------------------------------------------------
```

```
% -------- Function Name ----------------------------------------------
% Qb_Calc_EXPRMNT_and_MODEL_v02.m
% -------- Purpose --------
%       Calculates perfusion-related energy losses for MRgFUS
%       treatments by taking the difference in cooling between
%       simulated cooling (without any perfusion) and experimental
%       cooling (with perfusion).
% -------- Input Data --------
%       TEMPS       [nX,nY,nZ,nt]. 4D MR experimental temperature data
%                   during cooling. Should be zero-filled interpolated
%                   to desired simulation resolution.
%       Modl        [nX,nY,nZ]. Segmented tissue model(ie. 1=water,
%                   2=fat, 3...nTypes)
%       k           1xnTypes. Vector of thermal conductivity values.
%                   [W/(m*deg C)].
%       rho         1xnTypes. Vector, density values. [kg/m^3].
%       cp          1xnTypes. Vector specific heats. [J/(kg*deg C)].
%       tacq        Scalar. Acquisition time for each MRT image.
%       Vox         1x3 vector of MR voxel dimensions [dx dy dz]. [mm].
%       dt          Scalar. Time step for simulation calculations. [s].
%       Sim_Expand  'y' or 'n'. Expand simulation FOV for temperature
%                   calculations.  Helps minimize errors from zero
%                   temperature boundaries.
%         nExpand       1x3 vector of number of voxels to increase
%                       matrix in each direction.
%                       If Modl size is [40,40,40] and nExpand is [20
%                       30 40], final simulation Modl is [60,70,80]
%                       with original [40,40,40] centered.
%         TisExpand     Scalar. Tissue type to use from segmented model
%                       for additional tissue from Sim_Expand.
% -------- Output Data --------
%       TEMPS_Sim   [nX,nY,nZ,nt-1]. 4D simulated temperature data
%                   during cooling.
%                   Correspond to experimental TEMPS(:,:,:,2:end).
%       TEMPS_Diff  [nX,nY,nZ,nt-1]. Difference between 4D simulated
%                   and experimental temperature data during cooling.
%                   Correspond to experimental TEMPS(:,:,:,2:end).
%       Qb          [nX,nY,nZ,nt-1]. Perfusion-related energy losses.
%                   [W/m^3].
%       w           [nX,nY,nZ,nt-1]. Pennes perfusion parameter.
%                   [kg/(m^3*s)].
% -------- Required Subfunctions --------
%       NA
% -------- Author Info --------
%       Christopher Dillon
%       Department of Bioengineering
%       University of Utah
%       Version 01: 21 October 2013
% -------- Updates --------
%       v02      4 June2014         % Commented and cleaned up code
function
[TEMPS_Sim,TEMPS_Diff,Qb_v01,w_v01]=Qb_Calc_EXPRMNT_and_MODEL_v02(TEMPS
,Modl,k,rho,cp,tacq,Vox,dt,Sim_Expand,nExpand,TisExpand);

[nX,nY,nZ,nt]=size(TEMPS);
% Identify voxel dimensions, convert from [mm] to [m]
    dx=Vox(1)/1000;dy=Vox(2)/1000;dz=Vox(3)/1000;
```

```
    A=(dx/dy)^2;B=(dx/dz)^2;% Dimensionless lengths
Tb=0;    % Arterial Blood Temperature [deg C]
% Check that TEMPS and Modl are the same size
    [nx,ny,nz]=size(Modl);  % Identify model size
    if nx~=nX || ny~=nY || nz~=nZ
        errordlg('Dimensions of variables ''Modl'' and ''TEMPS'' must
be the same in X, Y, and Z.','ERROR','modal');return;
    end;clear nx ny nz
% Check that time step (dt) divides evenly into sampling time (tacq)
    if rem(tacq,dt)~=0
        errordlg('Time step variable ''dt'' must divide evenly into MR
sampling time variable ''tacq''.','ERROR','modal');return;
    end;
% Check Stability of Solver
    dt_max=1/( 2*max(k)*(1+A+B)/min(rho)/min(cp)/dx^2)
    if dt>dt_max
        errordlg('Time step ''dt'' must be smaller than dt_m_a_x on
command line for stability of solver.','ERROR','modal');return;
    end

% -----Define TEMPS2 and Modl2 which may have an expanded FOV-----
    if Sim_Expand=='y'; % Expand simulation FOV to minimize errors from
zero temperature boundaries.
        addX=nExpand(1);addY=nExpand(2);addZ=nExpand(3);
        TEMPS2=zeros(nX+addX,nY+addY,nZ+addZ,nt);
        [nX2,nY2,nZ2,nt]=size(TEMPS2);
        Modl2=TisExpand*ones(nX+addX,nY+addY,nZ+addZ);

startX=floor(addX/2)+1;startY=floor(addY/2)+1;startZ=floor(addZ/2)+1;
        endX=nX2-ceil(addX/2);endY=nY2-ceil(addY/2);endZ=nZ2-
ceil(addZ/2);
        TEMPS2(startX:endX,startY:endY,startZ:endZ,:)=TEMPS;
        Modl2(startX:endX,startY:endY,startZ:endZ)=Modl;
    else
        startX=1;startY=1;startZ=1;
        endX=nX;endY=nY;endZ=nZ;
        TEMPS2=TEMPS;
        Modl2=Modl;
    end

% -----Create Matrices of Properties for Solver-----
% Fill in property matrices with values from property vectors
    k1=k(Modl2(:,:,:));
    rho_m=rho(Modl2(:,:,:));
    cp_m=cp(Modl2(:,:,:));
    rho_cp=rho_m.*cp_m; % Simplfies eqns by combining density & sp heat
% Use original model size for perfusion calculations
    cp_M=cp(Modl(:,:,:));
    rho_cp_M=cp_M.*rho(Modl(:,:,:));

% Shift k values for use in solver
    k2= circshift(k1,[1  0  0]);
    k3= circshift(k1,[-1 0  0]);
    k4= circshift(k1,[0  1  0]);
    k5= circshift(k1,[0 -1  0]);
    k6= circshift(k1,[0  0  1]);
```

```
    k7= circshift(k1,[0  0 -1]);

% -----Preallocate Output Matrices-----
    TEMPS_Sim=zeros(nX,nY,nZ,nt-1,'single');
    TEMPS_Diff=zeros(nX,nY,nZ,nt-1,'single');
    Qb_v01=zeros(nX,nY,nZ,nt-1,'single');
    w_v01=zeros(nX,nY,nZ,nt-1,'single');

% -----Calculate Simulation Temps, Difference Temps, Perfusion losses,
and Pennes Parmeter-----
    NT=round(tacq/dt); % Number of simulation time steps between each
MR acquisition. NOTE: This code does NOT force the time step to divide
evenly into the acquisition time.
    tic   % Starts the stopwatch
    hh = waitbar(0,'Please wait... Model temperatures and perfusion
values are being calculated');  % Initiate waitbar
    for ii=1:nt-1
        T1=squeeze(TEMPS2(:,:,:,ii));
        for nn=1:NT % Run Model for each timestep of each FZ location
            waitbar((ii*NT+nn)/(NT*nt),hh); % Increment the waitbar
            % Shift Temperatures for use in solver
            T2= circshift(T1,[ 1  0  0]);
            T3= circshift(T1,[-1  0  0]);
            T4= circshift(T1,[ 0  1  0]);
            T5= circshift(T1,[ 0 -1  0]);
            T6= circshift(T1,[ 0  0  1]);
            T7= circshift(T1,[ 0  0 -1]);
       % Solve for Temperature: Includes only conduction

T1=squeeze(2*dt/(rho_cp*dx^2).*(T2./(1/k1+1/k2)+T3./(1/k1+1/k3)+A*(T4./
(1/k1+1/k4)+A*T5./(1/k1+1/k5))+B*(T6./(1/k1+1/k6)+T7./(1/k1+1/k7)))+...
               T1.*(1-2*dt/(rho_cp*dx^2).*(1/(1/k1+1/k2)
+1/(1/k1+1/k3)+A/(1/k1+1/k4)+A/(1/k1+1/k5)+B/(1/k1+1/k6)+B/(1/k1+1/k7))
));
        end
        %   Generate Output Matrices
        TEMPS_Sim(:,:,:,ii)=T1(startX:endX,startY:endY,startZ:endZ); %
Simulated Temperatures Corresponding to Experimental Temps (NOTE: First
TEMPS_Sim values in time (4th dimension) match 2nd TEMPS values in time
        TEMPS_Diff(:,:,:,ii)=TEMPS_Sim(:,:,:,ii)-TEMPS(:,:,:,ii+1); %
Difference between Simulated TEMPS with only conduction cooling and
Experimental TEMPS
        Qb_v01(:,:,:,ii)=TEMPS_Diff(:,:,:,ii).*rho_cp_M/tacq; %
Perfusion-related Energy Losses: See documentation for equation
        T_Ave=squeeze(TEMPS(:,:,:,ii)+TEMPS(:,:,:,ii+1))/2-Tb; %
Calculate Average of Subsequent Experimental Temperature measurements
for Pennes Parameter estimation
        w_v01(:,:,:,ii)=Qb_v01(:,:,:,ii)./cp_M./T_Ave; % Pennes
Perfusion Parameter: Qb=w*cp*(T-Tb), Use T_Ave for T
    end
toc   % Stops the stopwatch
close(hh);
end
% ---------------------------------------------------------------------
```

```
% -------- Function Name ----------------------------------------------
% Qb_Calc_EXPRMNT_ONLY_v02.m
% -------- Purpose --------
%       Calculates perfusion-related energy losses for MRgFUS
%       treatments by conservation of energy analysis.
% Qb=k*del^2*T-rho*cp*dT/dt                    During cooling
% del^2*T=T(i-1,p)-2*T(i,p)+T(i+1,p)/dx^2     For each spatial
direction,where i is current position, p indicates current time step
% dT/dt=(T(i,p+1)-T(i,p-1))/(2*tacq)      Central difference approx.
% -------- Input Data --------
%       TEMPS       [nX,nY,nZ,nt]. 4D MR experimental temperature data
%                   during cooling. Should be zero-filled interpolated
%                   to desired simulation resolution.
%       Modl        [nX,nY,nZ]. Segemented tissue model (ie. 1=water,
%                   2=fat, 3...nTypes)
%       k           1xnTypes. Vector of thermal conductivity values.
%                   [W/(m*deg C)].
%       rho         1xnTypes. Vector of density values. [kg/m^3].
%       cp          1xnTypes. Vector, specific heats. [J/(kg*deg C)].
%       tacq        Scalar. Acquisition time for each MRT image.
%       Vox         1x3 vector of voxel dimensions [dx dy dz]. [mm].
% -------- Output Data --------
%       Qb          [nX,nY,nZ,nt-2]. Perfusion-related energy losses.
%                   [W/m^3].
%       w           [nX,nY,nZ,nt-2]. Pennes perfusion parameter.
%                   [kg/(m^3*s)].
% -------- Required Subfunctions --------
%       NA
% -------- Author Info --------
%       Christopher Dillon
%       Department of Bioengineering
%       University of Utah
%       Version 01: 4 February 2014
% -------- Updates --------
%       v01      4 June 2014
%                  Alternate conservation of energy analysis that does
%                  not require the use of a FD solver.  Estimates of Qb
%                  obtained directly from the experimental temperature
%                  data.
%       v02     4 June 2014     Cleaned up and commented
function
[Qb_v02,w_v02]=Qb_Calc_EXPRMNT_ONLY_v02(TEMPS,Modl,k,rho,cp,tacq,Vox);

[nX,nY,nZ,nt]=size(TEMPS);
% Identify voxel dimensions, convert from [mm] to [m]
    dx=Vox(1)/1000;dy=Vox(2)/1000;dz=Vox(3)/1000;
    A=(dx/dy)^2;B=(dx/dz)^2; % Dimensionless lengths
Tb=0; % Arterial Blood Temperature [deg C]

% Check that TEMPS and Modl are the same size
    [nx,ny,nz]=size(Modl); % Identify model size
    if nx~=nX || ny~=nY || nz~=nZ
        errordlg('Dimensions of variables ''Modl'' and ''TEMPS'' must
be the same in X, Y, and Z.','ERROR','modal');return;
    end;clear nx ny nz
```

```
% -----Create Matrices of Properties for Solver-----
% Fill in property matrices with values from property vectors
    k1=k(Modl(:,:,:));
    rho_m=rho(Modl(:,:,:));
    cp_m=cp(Modl(:,:,:));
    rho_cp=rho_m.*cp_m; % Simplfies eqns by combining density & cp

% Shift k values for use in solver
    k2= circshift(k1,[1  0  0]);
    k3= circshift(k1,[-1 0  0]);
    k4= circshift(k1,[0  1  0]);
    k5= circshift(k1,[0 -1  0]);
    k6= circshift(k1,[0  0  1]);
    k7= circshift(k1,[0  0 -1]);

% -----Preallocate Output Matrices-----
    Qb_v02=zeros(nX,nY,nZ,nt-2,'single');
    w_v02=zeros(nX,nY,nZ,nt-2,'single');

% -----Calculate Simulation Temps, Difference Temps, Perfusion losses,
and Pennes Parmeter-----
    tic   % Starts the stopwatch
    hh = waitbar(0,'Please wait... Model temperatures and perfusion
values are being calculated');  % Initiate waitbar
    for ii=1:nt-2
        waitbar(ii/(nt-1),hh); % Increment the waitbar
        T1=squeeze(TEMPS(:,:,:,ii+1));
        T1Pm1=squeeze(TEMPS(:,:,:,ii));
        T1Pp1=squeeze(TEMPS(:,:,:,ii+2));
        % Shift Temperatures for use in solver
            T2= circshift(T1,[ 1  0  0]);
            T3= circshift(T1,[-1  0  0]);
            T4= circshift(T1,[ 0  1  0]);
            T5= circshift(T1,[ 0 -1  0]);
            T6= circshift(T1,[ 0  0  1]);
            T7= circshift(T1,[ 0  0 -1]);
        % Solve for Qb
            Qb_v02(:,:,:,ii)=(2/dx^2)*((T2-T1)./(1/k1+1/k2)+(T3-
T1)./(1/k1+1/k3)+A*(T4-T1)./(1/k1+1/k4)+A*(T5-T1)./(1/k1+1/k5)+B*(T6-
T1)./(1/k1+1/k6)+B*(T7-T1)./(1/k1+1/k7))-rho_cp.*(T1Pp1-
T1Pm1)/(2*tacq);
        T_Ave=T1-Tb;                % Calculate Average of Subsequent
Experimental Temperature measurements for Pennes Parameter estimation
        w_v02(:,:,:,ii)=Qb_v02(:,:,:,ii)./cp_m./T_Ave;
% Pennes Perfusion Parameter: Qb=w*cp*(T-Tb), Use T_Ave for T

    end
toc   % Stops the stopwatch
close(hh);
end
% ------------------------------------------------------------------------
```